



Relativistic symmetries in nuclei and hadrons

Joseph N. Ginocchio

MS B238, Los Alamos National Laboratory, Los Alamos, NM, 87545, USA

Accepted 11 April 2005

Available online 9 June 2005

editor: G.E. Brown

Abstract

Relativistic symmetries of the Dirac Hamiltonian had been discovered many years ago but only recently have these symmetries been recognized empirically in nuclear and hadronic spectroscopy. The empirical data supporting spin symmetry in hadron spectroscopy and pseudospin symmetry in nuclear spectroscopy are reviewed. Realistic relativistic mean field calculations of nuclei and QCD sum rules are reviewed and shown to support approximate pseudospin symmetry. These revelations suggest a more fundamental rationale for pseudospin symmetry motivating an investigation for pseudospin conservation in the nucleon–nucleon interaction. Open questions regarding hadron spin symmetry and nuclear pseudospin symmetry are discussed.

© 2005 Elsevier B.V. All rights reserved.

PACS: 21.60.Cs; 21.60.–n; 13.75.Cs; 21.30.–x; 02.20.–a; 14.40.–n; 14.20.–c

Keywords: Symmetry; Dirac equation; Pseudospin; Nuclear and hadron spectroscopy

Contents

1. Introduction	167
2. Symmetries of the Dirac Hamiltonian	168
2.1. General Bell–Reugg symmetries	169
2.2. Spin symmetry	171
2.2.1. Axially symmetric potentials	173
2.2.2. Spherically symmetric potentials	174
2.3. Pseudospin symmetry	176

E-mail address: gino@lanl.gov.

2.3.1.	Axially symmetric potentials	176
2.3.2.	Spherically symmetric potentials	178
3.	Radial nodes and bound states	180
3.1.	Radial nodes in general	180
3.1.1.	Spin symmetry	180
3.1.2.	Pseudospin symmetry	181
3.2.	Radial nodes in the spherical symmetry limit	181
3.2.1.	Radial nodes in the spherical symmetry limit: general	182
3.2.2.	Positive energy Dirac eigenstates	183
3.2.3.	Negative energy Dirac eigenstates	185
3.2.4.	Spin symmetry limit	185
3.2.5.	Pseudospin symmetry limit	185
3.3.	Conditions for bound states	186
3.3.1.	Conditions for bound positive energy states	186
3.3.2.	Conditions for bound negative energy states	187
4.	Pseudospin symmetry in nuclei	187
5.	Relativistic nuclear theories	192
5.1.	Relativistic field theory	193
5.2.	Relativistic point coupling model	193
5.3.	Features of the relativistic mean field	194
6.	QCD sum rules	195
7.	Testing nuclear eigenstates for pseudospin symmetry	197
7.1.	Test of realistic eigenfunctions with spherical symmetry	197
7.1.1.	Lower amplitudes	197
7.1.2.	Upper amplitudes	198
7.1.3.	Non-relativistic mean field eigenfunctions	201
7.2.	Pseudospin singlets and intruders	202
7.3.	Spin and pseudospin symmetry breaking	205
7.4.	Test of realistic eigenfunctions for deformed nuclei with axial symmetry	206
7.5.	Summary	211
8.	Magnetic dipole and Gamow–Teller transitions	213
8.1.	Magnetic moments and M1 transitions	213
8.2.	Non-relativistic limit	214
8.3.	Pseudospin symmetry	214
8.4.	Gamow–Teller transitions	216
8.5.	Non-relativistic limit of the Gamow–Teller transitions	217
8.6.	Pseudospin symmetry	217
8.7.	An example: ^{39}K , ^{39}Ca	218
8.8.	Global test of the M1 pseudospin relations	219
8.9.	Discussion	220
8.10.	Summary	222
9.	Quadrupole transitions in the pseudospin limit	223
10.	Pseudo-SU(4) symmetry	224
11.	Isospin dependence of pseudospin symmetry	225
12.	Nucleon scattering from nuclei	226
12.1.	Nucleon–nucleus scattering amplitude in the spin representation	228
12.2.	Nucleon–nucleus scattering amplitude in the pseudospin representation	229
12.3.	Experimental tests	230
13.	Anti-nucleon spectrum	232
14.	Spin symmetry in hadrons	232
14.1.	Introduction	232

14.2. Experimental and lattice QCD spectrum	232
14.3. Experimental test of relativistic spin symmetry	233
14.4. QCD origins	236
14.5. Summary	236
15. Exactly solvable Dirac Hamiltonians	236
15.1. Relativistic harmonic oscillator with spin symmetry	236
15.1.1. Eigenfunctions	237
15.1.2. Energy eigenvalues	237
15.1.3. Relativistic contribution	240
15.2. Relativistic harmonic oscillator with pseudospin symmetry	241
15.3. Dirac Hamiltonian with a tensor potential	242
15.4. Relativistic Coulomb potential and its analytical solutions	242
16. Pseudospin in nucleon–nucleon scattering	244
16.1. Spin–pseudospin transformation matrix for scattering states	244
16.2. Scattering matrix in the spin representation	245
16.3. Scattering matrix in the pseudospin representation	246
16.4. Test of spin and pseudospin conservation	247
16.5. Summary and conclusions	249
17. Summary and future	250
18. Future—beyond the mean field	250
19. Appendices	251
19.1. Orthogonal transformation in four dimensions	251
19.2. Invariant symmetry	255
19.3. Spherical amplitudes	256
Acknowledgements	257
References	257

1. Introduction

The discovery of relativistic symmetries of the Dirac Hamiltonian originated from early attempts to calculate meson masses using the Dirac Hamiltonian with external potentials to describe the dynamics between a quark and antiquark [1]. The authors noted that, if the external potentials are limited to a Lorentz scalar and the time component of a Lorentz vector, and, if these two potentials were equal up to a constant, the resulting masses are independent of the orientation of the spin. Such degeneracies are commonly assumed to be due to non-relativistic dynamics since relativistic dynamics introduces spin-orbit splittings. But this work showed that this is not necessarily the case. If the Lorentz scalar and the time component of the Lorentz potential are equal, but individually large compared to the mass of the quarks, the Dirac Hamiltonian will produce highly relativistic motion *and* spin degeneracy.

Four years later the relativistic spin generators for this symmetry were derived [2]. In the process, more general Dirac Hamiltonians were shown to have a “spin-like” symmetry if the Lorentz vector potentials with all four components non-zero are related to the scalar potential in a particular way which is elucidated in detail in the next section, Section 2. The original application of the Dirac Hamiltonian for the calculation of meson masses did not correctly predict the masses of the mesons because the mesons that were studied are composed of light quarks for which the one body Dirac Hamiltonian is not a valid approximation. More recently, the spin symmetry of the Dirac Hamiltonian has been successfully applied to mesons in

which either the quark (antiquark) is light and the antiquark (quark) is heavy [3]. We shall review the present status of relativistic symmetries in hadrons in Section 14.

Spin symmetry is easily detectable empirically because the mass (or energy) spectrum will be independent of the alignment of the spin with the spatial degrees of freedom. For example, the $p_{1/2}$ state, for which the spin is unaligned with respect to the unit orbital angular momentum, will be degenerate with the $p_{3/2}$ state, for which spin is aligned with the unit orbital angular momentum. Also the spin aligned state $s_{1/2}$ will have no unaligned partner because coupling spin to zero orbital angular momentum can only produce angular momentum $\frac{1}{2}$.

On the other hand the other symmetries of the Dirac Hamiltonian that Bell and Reugg discovered are not as transparent. For example, a Dirac Hamiltonian with a Lorentz scalar potential and a Lorentz vector potential (with only a time component) equal in magnitude but *opposite* in sign will produce a “spin”-like symmetry, which has become to be called pseudospin symmetry. As we shall see in Sections 2 and 3, in this case the $p_{1/2}$ state and a $p_{3/2}$ will not be degenerate. In fact the $p_{1/2}$ state will not have a degenerate partner and the $f_{5/2}$ state will be degenerate with a $p_{3/2}$ state, the $d_{3/2}$ state will be degenerate with a $s_{1/2}$, and so on. In other words, the degenerate states differ in orbital angular momentum by units of two. For this reason the origin of a quasi-degeneracy among states with these quantum numbers observed in nuclei many years ago [4,5] remained hidden and only recently has been discovered [6]. In Section 4 we shall review the history of pseudospin symmetry in nuclei, both experimental and theoretical aspects, prior to the discovery of pseudospin symmetry as a relativistic symmetry. Because pseudospin symmetry is now known to be a relativistic symmetry we examine relativistic nuclear theories in Section 5 from this new perspective. This leads to possible quantum chromodynamics (QCD) foundations for pseudospin symmetry which is discussed in Section 6. We shall then go on to explore the theoretical and empirical consequences of this new insight, that pseudospin symmetry is a relativistic symmetry, in Sections 7–9. The marriage of pseudospin with isospin into pseudo-SU(4) is reviewed in Section 10 whereas in Section 11 we discuss the isospin dependence of pseudospin symmetry. In Section 12 we investigate pseudospin symmetry in nucleon–nucleus scattering. In Section 13 we show that pseudospin symmetry for nucleons in a nuclear mean field implies spin symmetry for anti-nucleons bound in a nuclear mean field. We go on to discuss in Section 15 the exactly solvable Dirac Hamiltonians which have harmonic or Coulombic scalar and vector potentials and the additional symmetries that these special potentials engender.

The Dirac Hamiltonian describes the dynamics of relativistic single particle motion. For one light quark interacting with heavy quarks or for nucleons moving in the mean field of many nucleons in a nucleus, the Dirac Hamiltonian may be a good approximation. However for interacting particles of comparable mass the Dirac Hamiltonian is not appropriate and other approaches are necessary. In Section 16 we investigate pseudospin conservation in nucleon–nucleon scattering which will test pseudospin symmetry at a more fundamental level beyond the mean field.

Finally in Sections 17 and 18 we summarize and discuss open issues remaining to be investigated.

2. Symmetries of the Dirac Hamiltonian

The Lorentz covariant Dirac equation for a single particle with mass M is [7]:

$$[\gamma^\mu [c p_\mu + g_V A_\mu(x_\mu)] + M c^2 + V_S(x_\mu)] \Psi(x_\mu) = 0, \quad (1)$$

where x_μ is the four spatial vector (ct, \vec{r}) , \vec{r} is the three-dimensional vector (x, y, z) , $p_\mu = -i\hbar \frac{\partial}{\partial x_\mu}$, $A_\mu(x_\mu)$ is the Lorentz vector potential $(A_0(x_\mu), \vec{A}(x_\mu))$, c is the speed of light, and $V_S(x_\mu)$ is the Lorentz scalar potential. The Dirac matrices are four by four matrices

$$\gamma^0 = \begin{pmatrix} \mathbf{1} & 0 \\ 0 & -\mathbf{1} \end{pmatrix} = \beta, \quad \vec{\gamma} = \begin{pmatrix} 0 & \vec{\sigma} \\ -\vec{\sigma} & 0 \end{pmatrix} = \beta \vec{\alpha}, \quad (2)$$

where $\mathbf{1}$ is the two dimensional unit matrix and $\vec{\sigma}$ are the two dimensional Pauli matrices. Assuming that the potentials are time independent, the Dirac wavefunction can be factorized, $\Psi(x_\mu) = e^{-iEt/\hbar} \Phi(\vec{r})$, and, after multiplying through by β , the Dirac equation reduces to an eigenfunction equation,

$$H \Phi(\vec{r}) = E \Phi(\vec{r}), \quad (3)$$

where

$$H = \vec{\alpha} \cdot [c\vec{p} + g_V \vec{A}(\vec{r})] + V_V(\vec{r}) + \beta[Mc^2 + V_S(\vec{r})] \quad (4)$$

is the Dirac Hamiltonian and $V_V(\vec{r}) = g_V A_0(\vec{r})$ to conform to popular notation.

The conclusions that follow remain valid if we add an arbitrary constant to the vector and scalar potentials

$$V_V(\vec{r}) \rightarrow V_V(\vec{r}) + c_V, \quad V_S(\vec{r}) \rightarrow V_S(\vec{r}) + c_S \quad (5)$$

because we can just adjust the energy and mass by the same constant so that the Dirac equation remains unchanged:

$$E \rightarrow E + c_V, \quad Mc^2 \rightarrow Mc^2 - c_S. \quad (6)$$

2.1. General Bell–Reugg symmetries

We assume $V_V(\vec{r}) \neq 0$ and define a Euclidean four vector $\mathbf{e}_0 = (e_{0,0}, \vec{e}_0)$ such that

$$e_{0,0} = V_S(\vec{r})/V_V(\vec{r}), \quad \vec{e}_0 = \vec{A}(\vec{r})/V_V(\vec{r}). \quad (7)$$

Then, if this four vector is a unit vector, $\mathbf{e}_0 \cdot \mathbf{e}_0 = \vec{e}_0 \cdot \vec{e}_0 + e_{0,0}^2 = 1$, which is equivalent to

$$V_S(\vec{r})^2 = V_V(\vec{r})^2 - g_V^2 \vec{A}(\vec{r}) \cdot \vec{A}(\vec{r}) = g_V^2 A^\mu(\vec{r}) A_\mu(\vec{r}), \quad (8)$$

the Dirac Hamiltonian has an SU(2) invariant symmetry.

In order to prove this statement we define three additional unit Euclidean unit four vectors $\mathbf{e}_i = (e_{i,0}, \vec{e}_i)$, $i = 1, 2, 3$ which are orthogonal to the unit four vector $\mathbf{e}_0 = (e_{0,0}, \vec{e}_0)$. We then define prime Dirac matrices which are projections on to this new basis:

$$\beta' = \beta e_{0,0} + \vec{\alpha} \cdot \vec{e}_0 \quad (9a)$$

$$\alpha'_i = \beta e_{i,0} + \vec{\alpha} \cdot \vec{e}_i, \quad (9b)$$

where $(\alpha'_1, \alpha'_2, \alpha'_3) = \vec{\alpha}'$. This Euclidean orthogonal transformation of the Euclidean four vector (β, α_i) and six dimensional representation, (Σ_i, γ_i) , is discussed in more detail in the appendices (Section 19).

Since these new Dirac matrices are related to the original Dirac matrices by an orthogonal transformation, they have the same anticommutation and commutation relations as the original Dirac matrices; that is,

$$\{\beta', \beta'\} = 2, \quad \{\alpha'_i, \alpha'_j\} = -\{\gamma'_i, \gamma'_j\} = \{\Sigma'_i, \Sigma'_j\} = 2\delta_{i,j}, \quad (10a)$$

$$\{\beta', \alpha'_j\} = \{\beta', \gamma'_i\} = 0, \quad \{\beta', \Sigma'_j\} = 2\beta' \Sigma'_j, \quad (10b)$$

$$\{\Sigma'_i, \alpha'_j\} = 2\delta_{i,j}\gamma'_5, \quad \{\Sigma'_i, \gamma'_j\} = 2\delta_{i,j}\beta'\gamma'_5, \quad \{\alpha'_i, \gamma'_j\} = -2i\epsilon_{ijk}\beta'\Sigma'_k \quad (10c)$$

$$[\alpha'_i, \alpha'_j] = [\gamma'_i, \gamma'_j] = [\Sigma'_i, \Sigma'_j] = 2i\epsilon_{ijk}\Sigma'_k, \quad (11a)$$

$$[\beta', \beta'] = [\beta', \Sigma'_i] = 0, \quad [\beta', \alpha'_j] = 2\gamma'_j, \quad [\beta', \gamma'_i] = 2\alpha'_i, \quad (11b)$$

$$[\alpha'_i, \gamma'_j] = -2\delta_{i,j}\beta, \quad [\Sigma'_i, \alpha'_j] = 2i\epsilon_{ijk}\alpha'_k, \quad [\Sigma'_i, \gamma'_j] = 2i\epsilon_{ijk}\gamma'_k, \quad (11c)$$

where $\vec{\gamma}' = \beta'\vec{\alpha}'$ and $\vec{\Sigma}' = (\vec{\alpha}' \times \vec{\alpha}')/2i$. Similarly, transforming the four vector (Mc, \vec{p}) we have,

$$M'c = Mce_{0,0} + \vec{p} \cdot \vec{e}_0, \quad (12a)$$

$$p'_i = Mce_{i,0} + \vec{p} \cdot \vec{e}_i. \quad (12b)$$

Then the Dirac Hamiltonian with the Bell–Reugg condition in Eq. (8) becomes

$$\begin{aligned} H_{\text{BR}} &= \vec{\alpha} \cdot [c\vec{p} + g_V \vec{A}(\vec{r})] + V_V(\vec{r}) + \beta[Mc^2 + V_S(\vec{r})] \\ &= \vec{\alpha}' \cdot c\vec{p}' + V_V(\vec{r})(1 + \beta') + \beta'M'c^2. \end{aligned} \quad (13)$$

In the appendices (Section 19), using Eqs. (10)–(11), it is shown that the generators

$$\vec{S}' = \frac{\vec{\Sigma}'}{4}(1 + \beta') + \vec{\Sigma}' \cdot \vec{p}' \frac{\vec{\Sigma}'}{4\vec{p}' \cdot \vec{p}'} \vec{\Sigma}' \cdot \vec{p}'(1 - \beta') \quad (14)$$

form an SU(2) algebra and commute with the Dirac Hamiltonian H_{BR} ,

$$[S'_i, S'_j] = i\epsilon_{ijk}S'_k, \quad (15a)$$

$$[S'_i, H_{\text{BR}}] = 0. \quad (15b)$$

Thus the operators S'_i generate an SU(2) invariant symmetry of H_{BR} . Therefore each eigenstate of the Dirac Hamiltonian has a partner with the same energy,

$$H_{\text{BR}}\Phi_{k,\mu'}^{\text{BR}}(\vec{r}) = E_k\Phi_{k,\mu'}^{\text{BR}}(\vec{r}), \quad (16)$$

where k are the other quantum numbers and $\mu' = \pm\frac{1}{2}$ is the eigenvalue of S'_z ,

$$S'_z\Phi_{k,\mu'}^{\text{BR}}(\vec{r}) = \mu'\Phi_{k,\mu'}^{\text{BR}}(\vec{r}). \quad (17)$$

The eigenstates in the doublet will be connected by the generators S'_\pm ,

$$S'_\pm\Phi_{k,\mu'}^{\text{BR}}(\vec{r}) = \sqrt{\left(\frac{1}{2} \mp \mu'\right)\left(\frac{3}{2} \pm \mu'\right)}\Phi_{k,\mu' \pm 1}^{\text{BR}}(\vec{r}). \quad (18)$$

The Dirac eigenfunctions with a Lorentz vector potential with non-zero three components, $\vec{A}(\vec{r}) \neq 0$, will not conserve parity. To date there has not been an application for S'_k with $\vec{A}(\vec{r}) \neq 0$ for single-particle dynamics. Thus, we shall limit ourselves to the symmetries with $\vec{A}(\vec{r}) = 0$. However, beyond single-particle dynamics, the Bell–Reugg symmetries with $\vec{A}(\vec{r}) \neq 0$ may prove to be very useful as speculated in Section 18.

2.2. Spin symmetry

Spin symmetry occurs for $V_V(\vec{r}) = V_S(\vec{r}) + C_s$ in the Dirac Hamiltonian in Eq. (4) where C_s is a constant. This is the equivalent to $\beta' = \beta$, $\vec{\alpha}' = \vec{\alpha}$, $p' = p$ and $M'c^2 = Mc^2 + C_s$ in Eq. (13). The Dirac Hamiltonian with spin symmetry is

$$H_s = \vec{\alpha} \cdot c\vec{p} + V_V(\vec{r})(1 + \beta) + \beta(Mc^2 + C_s) , \quad (19)$$

and the spin generators are

$$\vec{S} = \begin{pmatrix} \vec{s} & 0 \\ 0 & \vec{s} \end{pmatrix} , \quad (20)$$

where $\vec{s} = \vec{\sigma}/2$ and $\vec{s} = U_p \vec{s} U_p$ where $U_p = \vec{\sigma} \cdot \vec{p}$ is the helicity unitary transformation [8]. We can write the eigenstates $\Phi_{k,\mu}^s(\vec{r})$ of the Dirac Hamiltonian,

$$H_s \Phi_{k,\mu}^s(\vec{r}) = E_k \Phi_{k,\mu}^s(\vec{r}) , \quad (21)$$

as a four dimensional vector,

$$\Phi_{k,\mu}^s(\vec{r}) = \begin{pmatrix} g_{k,\mu}^+(\vec{r}) \\ g_{k,\mu}^-(\vec{r}) \\ i f_{k,\mu}^+(\vec{r}) \\ i f_{k,\mu}^-(\vec{r}) \end{pmatrix} , \quad (22)$$

where $g_{k,\mu}^\pm(\vec{r})$ are the “upper Dirac components”, $f_{k,\mu}^\pm(\vec{r})$ are the “lower Dirac components” and + indicates spin up and – spin down.

Since these eigenstates must also belong to the spinor representation of the spin group, these amplitudes in the doublets with $\mu = \pm \frac{1}{2}$ must be related as indicated in Eqs. (17)–(18),

$$S_z \Phi_{k,\mu}^s(\vec{r}) = \mu \Phi_{k,\mu}^s(\vec{r}) , \quad (23)$$

and the eigenstates in the doublet will be connected by the generators S_\pm ,

$$S_\pm \Phi_{k,\mu}^s(\vec{r}) = \sqrt{\left(\frac{1}{2} \mp \mu\right) \left(\frac{3}{2} \pm \mu\right)} \Phi_{k,\mu \pm 1}^s(\vec{r}) . \quad (24)$$

Clearly from the fact that the upper component of the spin generators in Eq. (20) is simply \vec{s} , Eq. (23) implies that [9]

$$g_{k,-1/2}^+(\vec{r}) = g_{k,1/2}^-(\vec{r}) = 0 , \quad (25)$$

while Eq. (24) implies that

$$g_{k,1/2}^+(\vec{r}) = g_{k,-1/2}^-(\vec{r}) = g_k(\vec{r}) . \quad (26)$$

For the lower components the relationships are more complicated because the operator \vec{s} intertwines spin and space due to the dependence on the momentum. In order to simplify the derivations of the conditions on the lower component we introduce the functions $\tilde{f}_{k,\mu}^\pm$,

$$\begin{pmatrix} \tilde{f}_{k,\mu}^+(\vec{r}) \\ \tilde{f}_{k,\mu}^-(\vec{r}) \end{pmatrix} = U_p \begin{pmatrix} f_{k,\mu}^+(\vec{r}) \\ f_{k,\mu}^-(\vec{r}) \end{pmatrix} , \quad (27)$$

which has the inverse,

$$\begin{pmatrix} f_{k,\mu}^+(\vec{r}) \\ f_{k,\mu}^-(\vec{r}) \end{pmatrix} = U_p \begin{pmatrix} \tilde{f}_{k,\mu}^+(\vec{r}) \\ \tilde{f}_{k,\mu}^-(\vec{r}) \end{pmatrix} . \quad (28)$$

Then from Eqs. (23), (24), (27) and

$$U_p = \begin{pmatrix} p_z & p_- \\ p_+ & -p_z \end{pmatrix} , \quad (29)$$

where $p_\pm = p_x \pm ip_y$, we deduce that $p_i \tilde{f}_{k,1/2}^-(\vec{r}) = p_i \tilde{f}_{k,-1/2}^+(\vec{r}) = 0$ which leads to

$$\tilde{f}_{k,1/2}^-(\vec{r}) = \tilde{f}_{k,1/2}^-, \quad \tilde{f}_{k,-1/2}^+(\vec{r}) = \tilde{f}_{k,-1/2}^+ ; \quad (30)$$

that is, these amplitudes are constants. For the other amplitudes we derive

$$f_{k,+1/2}^+(\vec{r}) = \frac{p_z}{p} \tilde{f}_{k,\pm 1/2}^\pm(\vec{r}) = -f_{k,-1/2}^-(\vec{r}) , \quad (31)$$

and

$$f_{k,-1/2}^+(\vec{r}) = \frac{p_-}{p} \tilde{f}_{k,\pm 1/2}^\pm(\vec{r}), \quad f_{k,1/2}^-(\vec{r}) = \frac{p_+}{p} \tilde{f}_{k,\pm 1/2}^\pm(\vec{r}) . \quad (32)$$

From Eqs. (31) and (32) we get

$$f_{k,1/2}^+(\vec{r}) = -f_{k,-1/2}^-(\vec{r}) = f_k(\vec{r}) , \quad (33)$$

$$\left(\frac{\partial}{\partial x} + i \frac{\partial}{\partial y} \right) f_{k,-1/2}^+(\vec{r}) = \left(\frac{\partial}{\partial x} - i \frac{\partial}{\partial y} \right) f_{k,1/2}^-(\vec{r}) , \quad (34a)$$

$$\frac{\partial}{\partial z} f_{k,\mp 1/2}^\pm(\vec{r}) = \pm \left(\frac{\partial}{\partial x} \mp i \frac{\partial}{\partial y} \right) f_{k,\pm 1/2}^\pm(\vec{r}) . \quad (34b)$$

Therefore spin symmetry dictates that the Dirac wavefunctions in the doublet then become

$$\Phi_{k,1/2}^s(\vec{r}) = \begin{pmatrix} g_k(\vec{r}) \\ 0 \\ i f_k(\vec{r}) \\ i f_{k,1/2}^-(\vec{r}) \end{pmatrix}, \quad \Phi_{k,-1/2}^s(\vec{r}) = \begin{pmatrix} 0 \\ g_k(\vec{r}) \\ i f_{k,-1/2}^+(\vec{r}) \\ -i f_k(\vec{r}) \end{pmatrix} . \quad (35)$$

Thus, instead of the eight independent amplitudes for the two states in the doublet, there are four amplitudes, one upper and three lower, and the three lower are related by first order differential equations in Eqs. (34).

2.2.1. Axially symmetric potentials

If the potentials are axially symmetric then the Dirac Hamiltonian has an additional $U_s(1)$ symmetry. Axial symmetry means $V_S(\vec{r}) = V_S(\rho, z)$, $V_V(\vec{r}) = V_V(\rho, z)$, where $\rho = \sqrt{x^2 + y^2}$ and $x = \rho \cos(\phi)$, $y = \rho \sin(\phi)$; that is, the potentials are independent of the azimuthal angle ϕ . The Dirac Hamiltonian will then be invariant to rotations about the z -axis, $[L_z, H_S] = 0$ where

$$L_z = \begin{pmatrix} \ell_z & 0 \\ 0 & \tilde{\ell}_z \end{pmatrix}, \quad (36)$$

and $\tilde{\ell}_z = U_p \ell_z U_p$ and $\ell_z = \mathbf{r} \times \mathbf{p}$ and thus the invariant group will be $SU_s(2) \times U_s(1)$. Then the Dirac eigenstates are eigenstates of the $U_s(1)$ generator, L_z , and the total angular momentum generator $J_z = S_z + L_z$, which is also conserved,

$$J_z = \begin{pmatrix} j_z & 0 \\ 0 & j_z \end{pmatrix}, \quad (37)$$

where $j_z = \ell_z + s_z = \tilde{\ell}_z + \tilde{s}_z$.

The conventional method of labeling the eigenstates of axially deformed single-particle states in nuclei is to use the asymptotic quantum numbers $[N, n_3, A]$ Ω that emerge in the limit of a non-relativistic axially symmetric deformed harmonic oscillator [10] and in the limit of a relativistic axially symmetric deformed harmonic oscillator with spin symmetry [11] that we shall discuss in the Section 15, where N is the total harmonic oscillator quantum number, n_3 is the number of nodes in the z -direction, A is the angular momentum projection along the z -direction, and Ω is total angular momentum along the z -direction including the spin.

However, for realistic axially symmetric potentials only the quantum numbers A and Ω are conserved in the pseudospin limit. The eigenstates will then be eigenfunctions of the conserved quantum numbers

$$L_z \Phi_{\eta, A, \mu}^s(\vec{r}) = A \Phi_{\eta, A, \mu}^s(\vec{r}), \quad J_z \Phi_{\eta, A, \mu}^s(\vec{r}) = \Omega \Phi_{\eta, A, \mu}^s(\vec{r}), \quad \Omega = A + \mu. \quad (38)$$

The two states in the doublet will have the same orbital angular momentum projected along the symmetry axis A but will have different total angular momentum projected along the symmetry axis, $\Omega = A + \frac{1}{2}$ and $\Omega' = A - \frac{1}{2}$. Since N and n_3 are not conserved, we designate the additional quantum numbers needed to specify the single particle states by the generic quantum number η .

Following Eq. (35) the Dirac eigenstates in the doublet will therefore have the form

$$\Phi_{\eta, A, 1/2}^s(\vec{r}) = \begin{pmatrix} g_{\eta, A}(\rho, z) e^{iA\phi} \\ 0 \\ i f_{\eta, A}(\rho, z) e^{iA\phi} \\ i f_{\eta, A, 1/2}^-(\rho, z) e^{i(A+1)\phi} \end{pmatrix}, \quad \Omega = A + \frac{1}{2}, \quad (39a)$$

$$\Phi_{\eta, A, -1/2}^s(\vec{r}) = \begin{pmatrix} 0 \\ g_{\eta, A}(\rho, z) e^{iA\phi} \\ i f_{\eta, A, -1/2}^+(\rho, z) e^{i(A-1)\phi} \\ -i f_{\eta, A}(\rho, z) e^{iA\phi} \end{pmatrix}, \quad \Omega' = A - \frac{1}{2}. \quad (39b)$$

From Eq. (34) spin symmetry predicts the following differential relations between the lower amplitudes:

$$\left(\frac{\partial}{\partial \rho} + \frac{A+1}{\rho}\right) f_{\eta,A,1/2}^-(\rho, z) = \left(\frac{\partial}{\partial \rho} - \frac{A-1}{\rho}\right) f_{\eta,A,-1/2}^+(\rho, z) , \quad (40a)$$

$$\frac{\partial}{\partial z} f_{\eta,A,\mp 1/2}^\pm(\rho, z) = \pm \left(\frac{\partial}{\partial \rho} \pm \frac{A}{\rho}\right) f_{\eta,A,\pm 1/2}^\pm(\rho, z) . \quad (40b)$$

2.2.2. Spherically symmetric potentials

If the potentials are spherically symmetric then the Dirac Hamiltonian has an additional $SU_L(2)$ symmetry [12]. Spherically symmetric means $V_S(\vec{r}) = V_S(r)$, $V_V(\vec{r}) = V_V(r)$ where $r = \sqrt{x^2 + y^2 + z^2}$; that is, the potentials are independent of the polar angle θ , where $z = r \cos(\theta)$, $\rho = r \sin(\theta)$, as well as ϕ . The Dirac Hamiltonian will be invariant with respect to rotations about all three axes, $[L_i, H_s] = 0$ where

$$\vec{L} = \begin{pmatrix} \vec{\ell} & 0 \\ 0 & \vec{\ell} \end{pmatrix} , \quad (41)$$

and $\vec{\ell} = U_p \vec{\ell} U_p$ and the invariant group will be $SU_s(2) \times SU_L(2)$. The Dirac eigenstates will then be an eigenfunction of $\vec{L} \cdot \vec{L}$ as well as L_z and J_z ,

$$\vec{L} \cdot \vec{L} \Phi_{n_r, \ell, m, \mu}^s(\vec{r}) = \ell(\ell + 1) \Phi_{n_r, \ell, m, \mu}^s(\vec{r}) , \quad (42a)$$

$$L_z \Phi_{n_r, \ell, m, \mu}^s(\vec{r}) = m \Phi_{n_r, \ell, m, \mu}^s(\vec{r}) , \quad (42b)$$

$$J_z \Phi_{n_r, \ell, m, \mu}^s(\vec{r}) = M \Phi_{n_r, \ell, m, \mu}^s(\vec{r}), \quad M = m + \mu , \quad (42c)$$

where the radial quantum number n_r is the number of nodes of the upper amplitude at points $r \neq 0, \infty$ and is discussed in more detail in Section 3, ℓ is the orbital angular momentum in units of \hbar , $M = m + \mu$, m its projection, and the generators (41) will connect states with the same ℓ and different m ,

$$L_\pm \Phi_{n_r, \ell, m, \mu}^s(\vec{r}) = \sqrt{(\ell \mp m)(\ell \pm m + 1)} \Phi_{n_r, \ell, m \pm 1, \mu}^s(\vec{r}) . \quad (43)$$

As shown in the appendices (Section 19) these conditions will give for the amplitudes in Eq. (35),

$$\Phi_{n_r, \ell, m, 1/2}^s(\vec{r}) = \begin{pmatrix} g_{n_r, \ell}(r) Y_m^{(\ell)}(\theta, \phi) \\ 0 \\ i \sum_{j=\ell-1/2}^{\ell+1/2} A_m^j f_{n_r, \ell, j}(r) Y_m^{(\ell_j)}(\theta, \phi) \\ i \sum_{j=\ell-1/2}^{\ell+1/2} B_{m,1}^j f_{n_r, \ell, j}(r) Y_{m+1}^{(\ell_j)}(\theta, \phi) \end{pmatrix} , \quad M = m + \frac{1}{2} , \quad (44a)$$

$$\Phi_{n_r, \ell, m, -1/2}^s(\vec{r}) = \begin{pmatrix} 0 \\ g_{n_r, \ell}(r) Y_m^{(\ell)}(\theta, \phi) \\ i \sum_{j=\ell-1/2}^{\ell+1/2} B_{m,-1}^j f_{n_r, \ell, j}(r) Y_{m-1}^{(\ell_j)}(\theta, \phi) \\ -i \sum_{j=\ell-1/2}^{\ell+1/2} A_m^j f_{n_r, \ell, j}(r) Y_m^{(\ell_j)}(\theta, \phi) \end{pmatrix} , \quad M = m - \frac{1}{2} , \quad (44b)$$

where $Y_m^{(\ell)}(\theta, \phi)$ is the spherical harmonic of order ℓ , ℓ_j is given by

$$\ell_{\ell+1/2} = \ell + 1, \quad (45a)$$

$$\ell_{\ell-1/2} = \ell - 1, \quad (45b)$$

and

$$A_m^j = -\frac{1}{2} \sqrt{\frac{(j + \frac{1}{2} + m)(j + \frac{1}{2} - m)}{j(j+1)}}, \quad (46a)$$

$$B_{m,\pm 1}^j = \frac{1}{2} \sqrt{\frac{(j+1 \pm (\ell_j - \ell)(m \pm \frac{1}{2}))(j \pm (\ell_j - \ell)(m \pm \frac{1}{2}))}{j(j+1)}}. \quad (46b)$$

The reason that $\ell \pm 1$ appears in the lower amplitude is because of the unitary transformation U_p on the lower component of the orbital angular momentum given in Eq. (41) which changes both the parity and the orbital angular momentum by at most one unit.

Thus the spherical symmetry reduces the number of amplitudes in the doublet even further from four to three and two of these amplitudes are related by a first order differential equation

$$\left(\frac{\partial}{\partial r} + \frac{\ell+2}{r}\right) f_{n_r, \ell, \ell+1/2}(r) = \left(\frac{\partial}{\partial r} - \frac{\ell-1}{r}\right) f_{n_r, \ell, \ell-1/2}(r). \quad (47)$$

Since the total angular momentum, $\vec{J} = \vec{L} + \vec{S}$, is also conserved, the usual convention is to use the coupled basis,

$$\Psi_{n_r, \ell, j, M}^s(\vec{r}) = \sum_{m, \mu} C_{m\mu M}^{\ell(1/2)j} \Phi_{n_r, \ell, m, \mu}^s(\vec{r}), \quad (48)$$

which is also an eigenfunction of $\vec{J} \cdot \vec{J}$ but not of L_z :

$$\vec{J} \cdot \vec{J} \Psi_{n_r, \ell, j, M}^s(\vec{r}) = j(j+1) \Psi_{n_r, \ell, j, M}^s(\vec{r}), \quad (49a)$$

$$\vec{L} \cdot \vec{L} \Psi_{n_r, \ell, j, M}^s(\vec{r}) = \ell(\ell+1) \Psi_{n_r, \ell, j, M}^s(\vec{r}), \quad (49b)$$

$$J_z \Psi_{n_r, \ell, j, M}^s(\vec{r}) = M \Psi_{n_r, \ell, j, M}^s(\vec{r}). \quad (49c)$$

Rather than using the four row basis for this eigenfunction, it is more convenient to introduce the spin function χ_μ explicitly. The states that are a degenerate doublet are then the states with $j = \ell \pm \frac{1}{2}$ and, as shown in the appendices (Section 19), they have the two row form

$$\Psi_{n_r, \ell, j, M}^s(\vec{r}) = \begin{pmatrix} g_{n_r, \ell}(r) [Y^{(\ell)}(\theta, \phi) \chi_M^{(j)}] \\ i f_{n_r, \ell, j}(r) [Y^{(\ell_j)}(\theta, \phi) \chi_M^{(j)}] \end{pmatrix}, \quad (50)$$

where $[Y^{(\ell)}(\theta, \phi) \chi_M^{(j)}]$ is the coupled amplitude $\sum_{m\mu} C_{m\mu M}^{\ell(1/2)j} Y_m^{(\ell)}(\theta, \phi) \chi_\mu$.

While n_r is the number of radial nodes of the upper amplitude of eigenstates in the spin doublet, the number of radial nodes of the lower amplitudes will be determined by the Dirac Hamiltonian which will be discussed in detail in the next section. Nevertheless n_r is the quantum number of the Dirac eigenstate and therefore we use it to label the lower amplitudes as well.

2.3. Pseudospin symmetry

The pseudospin symmetry occurs for $V_V(\vec{r}) = -V_S(\vec{r}) + C_{ps}$. In this case $\beta' = -\beta$, $\vec{\alpha}' = \vec{\alpha}$, $p' = p$ and $M'c^2 = -(Mc^2 + C_{ps})$, and the Dirac Hamiltonian with pseudospin symmetry is

$$H_{ps} = \vec{\alpha} \cdot c\vec{p} + V_V(\vec{r})(1 - \beta) + \beta(Mc^2 + C_{ps}) , \quad (51)$$

and the pseudospin generators are [13]

$$\vec{\tilde{S}} = \begin{pmatrix} \vec{s} & 0 \\ 0 & \vec{s} \end{pmatrix} . \quad (52)$$

Therefore $\vec{\tilde{S}} = \gamma_5 \vec{S} \gamma_5$ where $\gamma_5 = \begin{pmatrix} 0 & 1 \\ 1 & 0 \end{pmatrix}$. Following similar logic as in the previous section we find that [9]

$$f_{\vec{k}, -1/2}^+(\vec{r}) = f_{\vec{k}, 1/2}^-(\vec{r}) = 0 , \quad (53a)$$

$$f_{\vec{k}, 1/2}^+(\vec{r}) = f_{\vec{k}, -1/2}^-(\vec{r}) = f_{\vec{k}}(\vec{r}) , \quad (53b)$$

$$g_{\vec{k}, 1/2}^+(\vec{r}) = -g_{\vec{k}, -1/2}^-(\vec{r}) = g_{\vec{k}}(\vec{r}) , \quad (53c)$$

$$\left(\frac{\partial}{\partial x} + i \frac{\partial}{\partial y} \right) g_{\vec{k}, -1/2}^+(\vec{r}) = \left(\frac{\partial}{\partial x} - i \frac{\partial}{\partial y} \right) g_{\vec{k}, 1/2}^-(\vec{r}) , \quad (53d)$$

$$\frac{\partial}{\partial z} g_{\vec{k}, \mp 1/2}^\pm(\vec{r}) = \pm \left(\frac{\partial}{\partial x} \mp i \frac{\partial}{\partial y} \right) g_{\vec{k}, \pm 1/2}^\pm(\vec{r}) . \quad (53e)$$

Thus, for pseudospin symmetry the *lower* components have the same spatial wavefunction, while the other upper components can have very different spatial wavefunctions. The upper components are the large components and dominate most experimental probes of the nucleus. This is the reason that the origin of pseudospin symmetry took almost 30 years to be discovered.

Thus the eigenstates in the doublet have the form

$$\Phi_{\vec{k}, 1/2}^{ps}(\vec{r}) = \begin{pmatrix} g_{\vec{k}}(\vec{r}) \\ g_{\vec{k}, 1/2}^-(\vec{r}) \\ i f_{\vec{k}}(\vec{r}) \\ 0 \end{pmatrix} , \quad \Phi_{\vec{k}, -1/2}^{ps}(\vec{r}) = \begin{pmatrix} g_{\vec{k}, -1/2}^+(\vec{r}) \\ -g_{\vec{k}}(\vec{r}) \\ 0 \\ i f_{\vec{k}}(\vec{r}) \end{pmatrix} . \quad (54)$$

Thus, instead of the eight independent amplitudes for the two states in the doublet, there are four amplitudes, one lower and three upper, and the three upper are related by first order differential equations in Eqs. (53).

2.3.1. Axially symmetric potentials

If the potentials are axially symmetric then the Dirac Hamiltonian has an additional $U_{ps}(1)$ symmetry. The Dirac Hamiltonian will then be invariant of rotations about the z -axis, $[\tilde{L}_z, H_{ps}] = 0$ where

$$\tilde{L}_z = \begin{pmatrix} \tilde{\ell}_z & 0 \\ 0 & \ell_z \end{pmatrix} , \quad (55)$$

and the invariant symmetry is $SU_{\text{ps}}(2) \times U_{\text{ps}}(1)$. Then Dirac eigenstates are eigenstates of the $U_{\text{ps}}(1)$ generator, \tilde{L}_z , and the total angular momentum generator $J_z = \tilde{S}_z + \tilde{L}_z$, which is also conserved,

$$\tilde{L}_z \Phi_{\tilde{\eta}, \tilde{\Lambda}, \tilde{\mu}}^{\text{ps}}(\vec{r}) = \tilde{\Lambda} \Phi_{\tilde{\eta}, \tilde{\Lambda}, \tilde{\mu}}^{\text{ps}}(\vec{r}), \quad J_z \Phi_{\tilde{\eta}, \tilde{\Lambda}, \tilde{\mu}}^{\text{ps}}(\vec{r}) = \Omega \Phi_{\tilde{\eta}, \tilde{\Lambda}, \tilde{\mu}}^{\text{ps}}(\vec{r}), \quad (56)$$

where $\tilde{\Lambda}$ is the pseudo-orbital angular momentum projection along the symmetry z -axis, $\Omega = \tilde{\Lambda} + \tilde{\mu}$ is the total angular momentum projection along the symmetry z -axis, and $\tilde{\eta}$ represents any additional quantum numbers needed to specify the eigenstates.

Therefore from Eq. (54) the Dirac eigenstates in the doublet will therefore have the form

$$\Phi_{\tilde{\eta}, \tilde{\Lambda}, 1/2, \Omega}^{\text{ps}}(\vec{r}) = \begin{pmatrix} g_{\tilde{\eta}, \tilde{\Lambda}}(\rho, z) e^{i\tilde{\Lambda}\phi} \\ g_{\tilde{\eta}, \tilde{\Lambda}, 1/2}^-(\rho, z) e^{i(\tilde{\Lambda}+1)\phi} \\ i f_{\tilde{\eta}, \tilde{\Lambda}}(\rho, z) e^{i\tilde{\Lambda}\phi} \\ 0 \end{pmatrix}, \quad \Omega' = \tilde{\Lambda} + \frac{1}{2}, \quad (57a)$$

$$\Phi_{\tilde{\eta}, \tilde{\Lambda}, -1/2, \Omega}^{\text{ps}}(\vec{r}) = \begin{pmatrix} g_{\tilde{\eta}, \tilde{\Lambda}, -1/2}^+(\rho, z) e^{i(\tilde{\Lambda}-1)\phi} \\ -g_{\tilde{\eta}, \tilde{\Lambda}}(\rho, z) e^{i\tilde{\Lambda}\phi} \\ 0 \\ i f_{\tilde{\eta}, \tilde{\Lambda}}(\rho, z) e^{i\tilde{\Lambda}\phi} \end{pmatrix}, \quad \Omega = \tilde{\Lambda} - \frac{1}{2}, \quad (57b)$$

with the upper components satisfying the following differential relations:

$$\left(\frac{\partial}{\partial \rho} + \frac{\tilde{\Lambda} + 1}{\rho} \right) g_{\tilde{\eta}, \tilde{\Lambda}, 1/2}^-(\rho, z) = \left(\frac{\partial}{\partial \rho} - \frac{\tilde{\Lambda} - 1}{\rho} \right) g_{\tilde{\eta}, \tilde{\Lambda}, -1/2}^+(\rho, z), \quad (58a)$$

$$\frac{\partial}{\partial z} g_{\tilde{\eta}, \tilde{\Lambda}, \mp 1/2}^{\pm}(\rho, z) = \pm \left(\frac{\partial}{\partial \rho} \pm \frac{\tilde{\Lambda}}{\rho} \right) g_{\tilde{\eta}, \tilde{\Lambda}, \pm 1/2}^{\pm}(\rho, z), \quad (58b)$$

which follow from Eqs. (53).

Although it makes sense to label the eigenstates with the pseudospin and pseudo-orbital angular momentum projection because they are the conserved quantum numbers, experimentally the deformed single-particle states are labeled by the orbital angular momentum projection along the symmetry axis. In the pseudospin limit the orbital angular momentum projection is conserved only in the extreme case that the vector and scalar potentials are a constant. The projection operator $(1 + \beta)/2$ projects the upper components from the Dirac eigenfunction. The orbital angular momentum projection generator in Eq. (41) operating on the upper components gives

$$L_z \frac{(1 + \beta)}{2} \Phi_{\tilde{\eta}, \tilde{\Lambda}, 1/2, \Omega}^{\text{ps}}(\vec{r}) = \begin{pmatrix} \tilde{\Lambda} g_{\tilde{\eta}, \tilde{\Lambda}}(\rho, z) e^{i\tilde{\Lambda}\phi} \\ (\tilde{\Lambda} + 1) g_{\tilde{\eta}, \tilde{\Lambda}, 1/2}^-(\rho, z) e^{i(\tilde{\Lambda}+1)\phi} \\ 0 \\ 0 \end{pmatrix}, \quad \Omega' = \tilde{\Lambda} + \frac{1}{2}, \quad (59a)$$

$$L_z \frac{(1+\beta)}{2} \Phi_{\tilde{\eta}, \tilde{\Lambda}, -1/2, \Omega'}^{\text{ps}}(\vec{r}) = \begin{pmatrix} (\tilde{\Lambda}-1)g_{\tilde{\eta}, \tilde{\Lambda}, -1/2}^+(\rho, z)e^{i(\tilde{\Lambda}-1)\phi} \\ -\tilde{\Lambda}g_{\tilde{\eta}, \tilde{\Lambda}}(\rho, z)e^{i\tilde{\Lambda}\phi} \\ 0 \\ 0 \end{pmatrix}, \quad \Omega = \tilde{\Lambda} - \frac{1}{2}. \quad (59b)$$

Therefore, in order for the upper components to have a definite orbital angular momentum projection,

$$g_{\tilde{\eta}, \tilde{\Lambda}}(\rho, z) = 0 \quad (60)$$

and

$$\Lambda = \tilde{\Lambda} - 1, \quad \Omega = \tilde{\Lambda} - \frac{1}{2}, \quad (61a)$$

$$\Lambda' = \tilde{\Lambda} + 1, \quad \Omega' = \tilde{\Lambda} + \frac{1}{2}. \quad (61b)$$

This agrees with the orbital angular momentum projection quantum numbers associated with pseudospin doublets as outlined in Section 4. Also Eq. (60) suggests that $g_{\tilde{\eta}, \tilde{\Lambda}}(\rho, z)$ will be small for realistic eigenfunctions as we shall see in Section 7.

2.3.2. Spherically symmetric potentials

If the potentials are spherically symmetric then the Dirac Hamiltonian has an additional $SU_{\tilde{L}}(2)$ symmetry. The Dirac Hamiltonian will be invariant with respect to rotations about all three axes, $[\tilde{L}_i, H_{\text{ps}}] = 0$ where

$$\vec{\tilde{L}} = \begin{pmatrix} \tilde{\ell} & 0 \\ 0 & \tilde{\ell} \end{pmatrix}, \quad (62)$$

and hence the invariant group will be $SU_{\text{ps}}(2) \times SU_{\tilde{L}}(2)$. The Dirac eigenstates will then be an eigenfunction of $\vec{\tilde{L}} \cdot \vec{\tilde{L}}$ as well as \tilde{L}_z and J_z ,

$$\vec{\tilde{L}} \cdot \vec{\tilde{L}} \Phi_{\tilde{n}_r, \tilde{\ell}, m, \tilde{\mu}}^{\text{ps}}(\vec{r}) = \tilde{\ell}(\tilde{\ell} + 1) \Phi_{\tilde{n}_r, \tilde{\ell}, m, \tilde{\mu}}^{\text{ps}}(\vec{r}), \quad (63a)$$

$$\tilde{L}_z \Phi_{\tilde{n}_r, \tilde{\ell}, m, \tilde{\mu}}^{\text{ps}}(\vec{r}) = \tilde{m} \Phi_{\tilde{n}_r, \tilde{\ell}, m, \tilde{\mu}}^{\text{ps}}(\vec{r}), \quad (63b)$$

$$J_z \Phi_{\tilde{n}_r, \tilde{\ell}, m, \tilde{\mu}}^{\text{ps}}(\vec{r}) = M \Phi_{\tilde{n}_r, \tilde{\ell}, m, \tilde{\mu}}^{\text{ps}}(\vec{r}), \quad (63c)$$

where \tilde{n}_r is the pseudo-radial quantum number, $M = \tilde{m} + \tilde{\mu}$ and the generators in Eq. (62) will connect states with the same $\tilde{\ell}$ and different \tilde{m} ,

$$\tilde{L}_{\pm} \Phi_{\tilde{n}_r, \tilde{\ell}, m, \tilde{\mu}}^{\text{ps}}(\vec{r}) = \sqrt{\frac{(\tilde{\ell} \mp \tilde{m})(\tilde{\ell} \pm \tilde{m} + 1)}{2}} \Phi_{\tilde{n}_r, \tilde{\ell}, m \pm 1, \tilde{\mu}}^{\text{ps}}(\vec{r}). \quad (64)$$

As shown in the appendices (Section 19) these conditions will give for the amplitudes,

$$\Phi_{\tilde{n}_r, \tilde{\ell}, \tilde{m}, 1/2}^{\text{ps}}(\vec{r}) = \begin{pmatrix} \sum_{j=\tilde{\ell}-1/2}^{\tilde{\ell}+1/2} A_{\tilde{m}\tilde{m}}^{\tilde{\ell}\tilde{\ell}_j} g_{\tilde{n}_r, \tilde{\ell}, j}(r) Y_{\tilde{m}}^{(\tilde{\ell}_j)}(\theta, \phi) \\ \sum_{j=\tilde{\ell}-1/2}^{\tilde{\ell}+1/2} A_{\tilde{m}\tilde{m}+1}^{\tilde{\ell}\tilde{\ell}_j} g_{\tilde{n}_r, \tilde{\ell}, j}(r) Y_{\tilde{m}+1}^{(\tilde{\ell}_j)}(\theta, \phi) \\ \text{if}_{\tilde{n}_r, \tilde{\ell}}(r) Y_{\tilde{m}}^{(\tilde{\ell})}(\theta, \phi) \\ 0 \end{pmatrix}, \quad M' = \tilde{m} + \frac{1}{2}, \quad (65a)$$

$$\Phi_{\tilde{n}_r, \tilde{\ell}, \tilde{m}, -1/2}^{\text{ps}}(\vec{r}) = \begin{pmatrix} \sum_{j=\tilde{\ell}-1/2}^{\tilde{\ell}+1/2} A_{\tilde{m}\tilde{m}-1}^{\tilde{\ell}\tilde{\ell}_j} g_{\tilde{n}_r, \tilde{\ell}, j}(r) Y_{\tilde{m}-1}^{(\tilde{\ell}_j)}(\theta, \phi) \\ -\sum_{j=\tilde{\ell}-1/2}^{\tilde{\ell}+1/2} A_{\tilde{m}\tilde{m}}^{\tilde{\ell}\tilde{\ell}_j} g_{\tilde{n}_r, \tilde{\ell}, j}(r) Y_{\tilde{m}}^{(\tilde{\ell}_j)}(\theta, \phi) \\ 0 \\ \text{if}_{\tilde{n}_r, \tilde{\ell}}(r) Y_{\tilde{m}}^{(\tilde{\ell})}(\theta, \phi) \end{pmatrix}, \quad M = \tilde{m} - \frac{1}{2}. \quad (65b)$$

Just as for spin symmetry the spherical symmetry reduces the number of amplitudes in the doublet from four to three and two of these amplitudes are related by a first order differential equation

$$\left(\frac{\partial}{\partial r} + \frac{\tilde{\ell} + 2}{r} \right) g_{\tilde{n}_r, \tilde{\ell}, \tilde{\ell}+1/2}(r) = \left(\frac{\partial}{\partial r} - \frac{\tilde{\ell} - 1}{r} \right) g_{\tilde{n}_r, \tilde{\ell}, \tilde{\ell}-1/2}(r). \quad (66)$$

Since the total angular momentum, $\vec{J} = \vec{L} + \vec{S}$, is also conserved, the usual convention is to use the coupled basis,

$$\Psi_{\tilde{n}_r, \tilde{\ell}, j, M}^{\text{ps}}(\vec{r}) = \sum_{\tilde{m}, \tilde{\mu}} C_{\tilde{m}\tilde{\mu}M}^{\tilde{\ell}(1/2)j} \Phi_{\tilde{n}_r, \tilde{\ell}, \tilde{m}, \tilde{\mu}, M}^{\text{ps}}(\vec{r}), \quad (67)$$

which is also an eigenfunction of $\vec{J} \cdot \vec{J}$ but not of \tilde{L}_z :

$$\vec{J} \cdot \vec{J} \Psi_{\tilde{n}_r, \tilde{\ell}, j, M}^{\text{ps}}(\vec{r}) = j(j+1) \Psi_{\tilde{n}_r, \tilde{\ell}, j, M}^{\text{ps}}(\vec{r}), \quad (68a)$$

$$\vec{L} \cdot \vec{L} \Psi_{\tilde{n}_r, \tilde{\ell}, j, M}^{\text{ps}}(\vec{r}) = \tilde{\ell}(\tilde{\ell}+1) \Psi_{\tilde{n}_r, \tilde{\ell}, j, M}^{\text{ps}}(\vec{r}), \quad (68b)$$

$$J_z \Psi_{\tilde{n}_r, \tilde{\ell}, j, M}^{\text{ps}}(\vec{r}) = M \Psi_{\tilde{n}_r, \tilde{\ell}, j, M}^{\text{ps}}(\vec{r}). \quad (68c)$$

Rather than using the four row basis for this eigenfunction, it is more convenient to introduce the spin function $\chi_{\tilde{\mu}}$ explicitly. The states that are a degenerate doublet are then the states with $j = \tilde{\ell} \pm \frac{1}{2}$ and, as shown in the appendices (Section 19), they have the two row form

$$\Psi_{\tilde{n}_r, \tilde{\ell}, j, M}^{\text{ps}}(\vec{r}) = \begin{pmatrix} g_{\tilde{n}_r, \tilde{\ell}, j}(r) [Y^{(\tilde{\ell}_j)}(\theta, \phi) \chi_M^{(j)}] \\ \text{if}_{\tilde{n}_r, \tilde{\ell}}(r) [Y^{(\tilde{\ell})}(\theta, \phi) \chi_M^{(j)}] \end{pmatrix}. \quad (69)$$

Thus spherical symmetry reduces the number of independent amplitudes even more to two upper amplitudes and one lower amplitude. The two upper amplitudes are related by the differential equation in Eq. (66).

For pseudospin the lower component spatial amplitudes in the doublet are equal and therefore it is convenient to label the eigenfunctions by the radial quantum number and orbital angular momentum

of the lower component. However, the experimental eigenfunctions are labelled by the radial quantum number and orbital angular momentum of the upper component. We see from Eq. (69) that the orbital angular momentum of the upper component is $\tilde{\ell}_j$ and from Eq. (45) that the relation between the orbital angular momentum of the upper component and the pseudo-orbital angular momentum is given by

$$\ell = \tilde{\ell} - 1 \quad \text{for } j = \tilde{\ell} - \frac{1}{2} = \ell + \frac{1}{2}, \quad (70a)$$

$$\ell' = \tilde{\ell} + 1 = \ell + 2 \quad \text{for } j = \tilde{\ell} + \frac{1}{2} = \ell' - \frac{1}{2}, \quad (70b)$$

which agrees with the original assignments over 30 years ago as discussed in the Introduction.

As for the radial nodes, we shall show in the next subsection that the radial nodes of the upper components are related to the radial nodes of the lower components, \tilde{n}_r , by

$$n_r = \tilde{n}_r \quad \text{for } j = \tilde{\ell} - \frac{1}{2}, \quad (71a)$$

$$n'_r = \tilde{n}_r - 1 \quad \text{for } j = \tilde{\ell} + \frac{1}{2}. \quad (71b)$$

3. Radial nodes and bound states

In general the Dirac eigenstates have four spatial amplitudes as seen in Eq. (22). Spin symmetry or pseudospin symmetry impose relations between upper components and between lower components but they do not impose conditions relating upper and lower components. However, the Dirac eigenfunction (3) relates these amplitudes by means of first order differential equations in the spatial coordinates:

$$\begin{pmatrix} f^+(\vec{r}) \\ f^-(\vec{r}) \end{pmatrix} = \frac{-ic}{E + Mc^2 + V_S - V_V} \begin{pmatrix} p_z g^+(\vec{r}) + p_- g^-(\vec{r}) \\ -p_z g^-(\vec{r}) + p_+ g^+(\vec{r}) \end{pmatrix}, \quad (72a)$$

$$\begin{pmatrix} g^+(\vec{r}) \\ g^-(\vec{r}) \end{pmatrix} = \frac{ic}{E - Mc^2 - V_S - V_V} \begin{pmatrix} p_z f^+(\vec{r}) + p_- f^-(\vec{r}) \\ -p_z f^-(\vec{r}) + p_+ f^+(\vec{r}) \end{pmatrix}, \quad (72b)$$

where we have suppressed the quantum numbers. Therefore we can ask: what are the implications of these relationships? For the general case we shall make some qualitative statements. For the spherical symmetry limit this question has been explored in detail [14–16] and we shall be able to draw definitive conclusions.

3.1. Radial nodes in general

3.1.1. Spin symmetry

In the spin symmetry limit $V_S = V_V + C_s$, where C_s is a constant, we have from Eq. (72a)

$$f_k(\vec{r}) = \frac{-\hbar c}{E_k + Mc^2 + C_s} \frac{\partial}{\partial z} g_k(\vec{r}), \quad (73a)$$

$$f_{k,1/2}^-(\vec{r}) = \frac{-\hbar c}{E_k + Mc^2 + C_s} \left(\frac{\partial}{\partial x} + i \frac{\partial}{\partial y} \right) g_k(\vec{r}), \quad (73b)$$

$$f_{k,-1/2}^+(\vec{r}) = \frac{-\hbar c}{E_k + Mc^2 + C_s} \left(\frac{\partial}{\partial x} - i \frac{\partial}{\partial y} \right) g_k(\vec{r}) . \quad (73c)$$

If we assume the nodes in one direction are independent of the other directions, we can draw the following conclusions from these differential relations:

- (1) $f_k(\vec{r})$ has the same number of nodes in the x, y directions as $g_k(\vec{r})$, and
- (2) $f_{k,1/2}^-(\vec{r}), f_{k,-1/2}^+(\vec{r})$ have the same number of nodes in the z direction as $g_k(\vec{r})$.

In the axially symmetric limit this reduces to:

- (1) $f_{\eta,A}(\rho, z)$ has the same number of nodes in the ρ direction as $g_{N,n_3,A}(\rho, z)$,
- (2) $f_{\eta,A,1/2}^-(\rho, z)$ and $f_{\eta,A,-1/2}^+(\rho, z)$ have the same number of nodes in the z direction as $g_{\eta,A}(\rho, z)$.

3.1.2. Pseudospin symmetry

In the pseudospin symmetry limit $V_S = -V_V + C_{ps}$, where C_{ps} is a constant, we have from (72b)

$$g_{\tilde{k}}(\vec{r}) = \frac{\hbar c}{E_{\tilde{k}} - Mc^2 - C_{ps}} \frac{\partial}{\partial z} f_{\tilde{k}}(\vec{r}) , \quad (74a)$$

$$g_{\tilde{k},1/2}^-(\vec{r}) = \frac{\hbar c}{E_{\tilde{k}} - Mc^2 - C_{ps}} \left(\frac{\partial}{\partial x} + i \frac{\partial}{\partial y} \right) f_{\tilde{k}}(\vec{r}) , \quad (74b)$$

$$g_{\tilde{k},-1/2}^+(\vec{r}) = \frac{\hbar c}{E_{\tilde{k}} - Mc^2 - C_{ps}} \left(\frac{\partial}{\partial x} - i \frac{\partial}{\partial y} \right) f_{\tilde{k}}(\vec{r}) . \quad (74c)$$

If we assume the nodes in one direction are independent of the other directions we can draw the following conclusions from these differential relations:

- (1) $g_{\tilde{k}}(\vec{r})$ has the same number of nodes in the x, y directions as $f_{\tilde{k}}(\vec{r})$, and
- (2) $g_{\tilde{k},1/2}^-(\vec{r}), g_{\tilde{k},-1/2}^+(\vec{r})$ have the same number of nodes in the z direction as $f_{\tilde{k}}(\vec{r})$.

In the axially symmetric limit this reduces to:

- (1) $g_{\tilde{\eta},\tilde{A}}(\rho, z)$ has the same number of nodes in the ρ direction as $f_{\tilde{\eta},\tilde{A}}(\rho, z)$ and $A = \tilde{A}$,
- (2) $g_{\tilde{\eta},\tilde{A},1/2}^-(\rho, z)$ and $g_{\tilde{\eta},\tilde{A},-1/2}^+(\rho, z)$ have the same number of nodes in the z direction as $f_{\tilde{\eta},\tilde{A}}(\rho, z)$.

However, these conclusions are valid only if the number of nodes in one direction are independent of the other directions. This is true for the relativistic harmonic oscillator [11] but is not true for realistic deformed potentials.

3.2. Radial nodes in the spherical symmetry limit

We shall determine the relationship between the radial nodes in general at first, not necessarily in the spin or pseudospin symmetry limit. We shall show that, if the number of radial nodes of the upper

component is known, then the Dirac equation predicts the number of radial nodes of the lower component, and vice versa. If in addition there is a spin or pseudospin symmetry, the number of radial nodes in the partner eigenstate are then predicted as well.

3.2.1. Radial nodes in the spherical symmetry limit: general

In the spherical symmetry limit the operator

$$\hat{\kappa} = -\beta(\vec{\sigma} \cdot \vec{\ell} + 1) \quad (75)$$

commutes with the Dirac Hamiltonian, $[H, \hat{\kappa}] = 0$, independent of spin and pseudospin symmetry [7]. The Dirac eigenstates will then be eigenstates of this operator

$$\hat{\kappa}\Psi_{n_r, \kappa, j, M}(\vec{r}) = \kappa\Psi_{n_r, \kappa, j, M}(\vec{r}) \quad (76)$$

with eigenvalues

$$\kappa = \pm(j + \frac{1}{2}) , \quad (77)$$

and the eigenstates are labeled by this conserved quantum number rather than the orbital angular momentum or pseudo-orbital angular momentum.

The eigenvectors have the form

$$\Psi_{n_r, \kappa, j, m}(\vec{r}) = \begin{pmatrix} g_{n_r, \kappa, j}(r) [Y^{(\ell_u)}(\theta, \phi) \chi]_m^{(j)} \\ i f_{n_r, \kappa, j}(r) [Y^{(\ell_l)}(\theta, \phi) \chi]_m^{(j)} \end{pmatrix} , \quad (78)$$

with

$$\ell_u = \kappa, \quad \ell_l = \kappa - 1 \quad \text{for } j = \ell_u - \frac{1}{2} = \ell_l + \frac{1}{2} , \quad (79a)$$

and

$$\ell_u = -\kappa - 1, \quad \ell_l = -\kappa \quad \text{for } j = \ell_u + \frac{1}{2} = \ell_l - \frac{1}{2} ; \quad (79b)$$

that is, for states unaligned with orbital angular momentum or aligned with pseudo-orbital angular momentum, $\kappa > 0$, and for states aligned with orbital angular momentum or unaligned with pseudo-orbital angular momentum, $\kappa < 0$. We note that both the upper and lower components depend on j when there is no spin nor pseudospin symmetry.

For simplicity in the following we suppress all quantum numbers and label the radial amplitudes only with κ . The Dirac equation in terms of these two radial amplitudes becomes [14]

$$\frac{dg_\kappa(r)}{dr} = -\frac{(\kappa + 1)}{r} g_\kappa(r) + A(r) f_\kappa(r) , \quad (80a)$$

$$\frac{df_\kappa(r)}{dr} = \frac{(\kappa - 1)}{r} f_\kappa(r) - B(r) g_\kappa(r) , \quad (80b)$$

where

$$A(r) = [E_\kappa + M + V_S(r) - V_V(r)] , \quad (81a)$$

$$B(r) = [E_\kappa - M - V_S(r) - V_V(r)] . \quad (81b)$$

In the following we shall use Eq. (80) to determine how the number of radial nodes of $g_\kappa(r)$ is related to the number of nodes of $f_\kappa(r)$. The number of radial nodes is the number of times the amplitude becomes zero other than at the points $r = 0$ or ∞ .

3.2.2. Positive energy Dirac eigenstates

For nuclei the potentials will be finite at the origin, $|V_S(0)| < \infty$, $|V_V(0)| < \infty$, and go to zero monotonically as $r \rightarrow \infty$. Also we know the binding energies for nuclear states, $M - E_\kappa \leq 40$ MeV, are much smaller than the mass of the nucleon, $M = 938$ MeV. As we shall see in Section 5, for realistic nuclear potentials $A(r) > 0$ for all r . On the other hand, $V_S(r) + V_V(r)$ is the potential that binds the nucleon and therefore it must be attractive and, at the origin, greater in magnitude than the binding energy but must vanish as $r \rightarrow \infty$. Hence $B(r)$ starts off positive at the origin but decreases monotonically and becomes negative as $r \rightarrow \infty$ and therefore vanishes at some point $r = r_B$.

We introduce $G_\kappa(r) = r^{\kappa+1} g_\kappa(r)$ and $F_\kappa(r) = r^{-\kappa+1} f_\kappa(r)$. Then in the open interval $(0, \infty)$, nodes of $f_\kappa(r)$ and $g_\kappa(r)$ coincide with nodes of $F_\kappa(r)$ and $G_\kappa(r)$. From Eq. (79b) we get

$$\frac{dG_\kappa(r)}{dr} = r^{2\kappa} A(r) F_\kappa(r) , \quad (82a)$$

$$\frac{dF_\kappa(r)}{dr} = -r^{-2\kappa} B(r) G_\kappa(r) . \quad (82b)$$

A number of observations follow from Eq. (82). First,

$$G_\kappa(r) \rightarrow G_\kappa^0, \quad F_\kappa(r) \rightarrow F_\kappa^0 r^{1-2\kappa}, \quad r \rightarrow 0, \quad \kappa < 0 , \quad (83a)$$

$$G_\kappa(r) \rightarrow G_\kappa^0 r^{2\kappa+1}, \quad F_\kappa(r) \rightarrow F_\kappa^0, \quad r \rightarrow 0, \quad \kappa > 0 , \quad (83b)$$

$$G_\kappa(r), F_\kappa(r) \rightarrow 0, \quad r \rightarrow \infty . \quad (83c)$$

and both $G_\kappa(r)$, $F_\kappa(r)$ go to zero exponentially in Eq. (83c). Second, it is impossible for $F_\kappa(r)$ and $G_\kappa(r)$ to vanish simultaneously at the same point because, if they did, then all other higher-order derivatives would vanish at that point and hence the functions themselves would vanish everywhere. Third, we see that a node of $F_\kappa(r)$ corresponds to an extremum of $G_\kappa(r)$, and a node of $G_\kappa(r)$ corresponds to an extremum of $F_\kappa(r)$. $F_\kappa(r)$ will have an additional extremum at one point $r = r_B$ which does not correspond to a node of $G_\kappa(r)$. It follows that the nodes of $F_\kappa(r)$ and $G_\kappa(r)$ alternate; that is, between every pair of adjacent nodes of $F_\kappa(r)$ (or $G_\kappa(r)$) there is one node of $G_\kappa(r)$ (or $F_\kappa(r)$). If we let r_1 be a node of $F_\kappa(r)$ and r_2 be a node of $G_\kappa(r)$, then the nature of the extrema at these points is determined from the second derivatives

$$\left. \frac{d^2 G_\kappa(r)}{dr^2} \right|_{r=r_1} = -A(r_1) B(r_1) G_\kappa(r_1) \quad \text{where } F_\kappa(r_1) = 0 , \quad (84a)$$

$$\left. \frac{d^2 F_\kappa(r)}{dr^2} \right|_{r=r_2} = -A(r_2) B(r_2) F_\kappa(r_2) \quad \text{where } G_\kappa(r_2) = 0 . \quad (84b)$$

As bound states, both $G_\kappa(r)$ and $F_\kappa(r)$ vanish at $r = \infty$ and their extrema are concave towards the r -axis. Therefore, the extrema at the nodes r_1 or r_2 are minima (maxima) if the functions $G_\kappa(r)$ or $F_\kappa(r)$ are negative (positive) respectively at these points. It follows from Eq. (84) that nodes of $F_\kappa(r)$ and $G_\kappa(r)$

can occur only where the product $A(r)B(r) > 0$ is positive. Since for practical applications $A(r) > 0$, this condition reduces to

$$B(r) > 0 \quad \text{at nodes of } F_\kappa(r) \text{ and } G_\kappa(r) . \quad (85)$$

The potential $V_S(r) + V_V(r)$ appearing in $B(r)$, Eq. (81b), is the average potential felt by the nucleon in the non-relativistic limit, as stated above. Therefore, the condition of Eq. (85) is similar to the statement in the non-relativistic case, that nodes of the radial wave function can occur only in the region of classically allowed motion, i.e., where the kinetic energy is positive.

We now use the above results to obtain a relation between the radial nodes of $F_\kappa(r)$ and $G_\kappa(r)$. For that purpose we consider the equation for $G_\kappa(r)F_\kappa(r)$ as derived from Eq. (80),

$$(G_\kappa(r)F_\kappa(r))' = A(r) F_\kappa(r)^2 - B(r) G_\kappa(r)^2 . \quad (86)$$

For large r , $(G_\kappa(r)F_\kappa(r))' \sim (E_\kappa + M)F_\kappa(r)^2 - (E_\kappa - M)G_\kappa(r)^2 > 0$ is positive, since the binding energy $(M - E_\kappa) > 0$ for bound states. At small r , $(G_\kappa(r)F_\kappa(r))' = -B(0)G_\kappa(r)^2 < 0$ for $\kappa < 0$, while $(G_\kappa(r)F_\kappa(r))' = A(0)F_\kappa(r)^2 > 0$ for $\kappa > 0$, by employing Eq. (83). Since $G_\kappa(r)F_\kappa(r)$ vanishes both at $r = 0$ and ∞ we see that it is an increasing negative function at large r , while at small r , $G_\kappa(r)F_\kappa(r)$ is a decreasing negative function for $\kappa < 0$ and an increasing positive function for $\kappa > 0$,

$$\text{for } r \rightarrow \infty, \quad G_\kappa(r)F_\kappa(r) < 0 , \quad (87a)$$

$$\text{for } r \rightarrow 0, \quad G_\kappa(r)F_\kappa(r) < 0 \quad (\kappa < 0) , \quad (87b)$$

$$\text{for } r \rightarrow 0 \quad G_\kappa(r)F_\kappa(r) > 0 \quad (\kappa > 0) , \quad (87c)$$

consistent with Eq. (83). Furthermore, since $A(r) > 0$ and by using Eq. (85) we find that

$$(G_\kappa(r)F_\kappa(r))'|_{r=r_1} = -B(r_1)G_\kappa(r_1)^2 < 0 \quad \text{where } F(r_1) = 0 , \quad (88a)$$

$$(G_\kappa(r)F_\kappa(r))'|_{r=r_2} = A(r_2)F_\kappa(r_2)^2 > 0 \quad \text{where } G(r_2) = 0 . \quad (88b)$$

Thus $G_\kappa(r)F_\kappa(r)$ is a decreasing function at the nodes of $F_\kappa(r)$, and an increasing function at the nodes of $G_\kappa(r)$. Exploiting all these derived properties, we observe that for $\kappa > 0$, $G_\kappa(r)F_\kappa(r)$ is positive at small r and negative at large r , and hence has an odd number of zeroes. By Eq. (88) the first and last zeroes of $G_\kappa(r)F_\kappa(r)$ correspond to nodes of $F_\kappa(r)$, and since the nodes of $F_\kappa(r)$ and $G_\kappa(r)$ alternate, then the number of nodes of F exceed by one the number of nodes of $G_\kappa(r)$. On the other hand, for $\kappa < 0$, $G_\kappa(r)F_\kappa(r)$ has the same (negative) sign near both end points, and hence has an even number of zeroes. By similar arguments we find that in this case the first and last zeroes of $G_\kappa(r)F_\kappa(r)$ are nodes of $G_\kappa(r)$ and $F_\kappa(r)$, respectively, and that $G_\kappa(r)$ and $F_\kappa(r)$ have the same number of nodes. Altogether we have

$$\kappa < 0 : n_f = n_g , \quad (89a)$$

$$\kappa > 0 : n_f = n_g + 1, \quad (89b)$$

where n_f and n_g denote the number of internal nodes of $f_\kappa(r)$ and $g_\kappa(r)$, respectively; that is, the number of times the amplitude goes to zero excluding $r = 0$ and ∞ . For $\kappa > 0$, the first and last nodes (considering $f_\kappa(r)$ and $g_\kappa(r)$ together) are $f_\kappa(r)$ nodes. For $\kappa < 0$, the nodes of $g_\kappa(r)$ precede those of $f_\kappa(r)$ as r increases. The same results can be obtained by considering the Riccati equation for the ratio $f_\kappa(r)/g_\kappa(r)$ and its asymptotic values, as shown in [14,15] for vector potentials.

3.2.3. Negative energy Dirac eigenstates

For negative energy eigenstates the roles of $A(r)$ and $-B(r)$ become reversed. $B(r)$ is always negative, while $A(r)$ starts off as negative for r small and then becomes positive as r becomes very large. This results in

$$\kappa < 0 : \bar{n}_g = \bar{n}_f + 1 , \quad (90a)$$

$$\kappa > 0 : \bar{n}_g = \bar{n}_f , \quad (90b)$$

where \bar{n}_f and \bar{n}_g are the number of internal nodes of $f_\kappa(r)$ and $g_\kappa(r)$, respectively.

3.2.4. Spin symmetry limit

For spin symmetry, the rank of the spherical harmonic, ℓ , of the upper amplitudes for the two states in the doublet is the same. The spin aligned state has negative κ and the spin aligned states so that

$$\kappa = -(\ell + 1), \quad j = \ell + \frac{1}{2} , \quad (91a)$$

$$\kappa = \ell, \quad j = \ell - \frac{1}{2} . \quad (91b)$$

Likewise, the radial amplitudes of the upper components in Eq. (50) in the doublet have the same number of radial nodes. Therefore, for the eigenstate for which the spin is aligned with the orbital angular momentum ($\kappa < 0$), we see from Eq. (89) that the spatial amplitudes of the upper and lower component have the same number of radial nodes, while for the eigenstate for which the spin is unaligned with the orbital angular momentum ($\kappa > 0$), the spatial amplitude of the lower component has one radial node more than the spatial amplitude of the upper component and, therefore, one radial node more than the spatial amplitude of the lower component of its partner in the spin doublet. For example, the spatial amplitudes of the upper components of $p_{3/2}$, $p_{1/2}$ eigenstates and the spatial amplitude of the lower component of $p_{3/2}$ eigenstates all have the radial quantum number, whereas the spatial amplitude of the lower component of the $p_{1/2}$ eigenstate has one more radial node than these amplitudes.

3.2.5. Pseudospin symmetry limit

On the other hand, for pseudospin symmetry, the rank of the spherical harmonic, $\tilde{\ell}$, of the lower amplitudes for the two states in the doublet is the same. The pseudospin aligned state has positive κ and the pseudospin unaligned state has negative κ so that

$$\kappa = -\tilde{\ell}, \quad j = \tilde{\ell} - \frac{1}{2} , \quad (92a)$$

$$\kappa = \tilde{\ell} + 1, \quad j = \tilde{\ell} + \frac{1}{2} . \quad (92b)$$

Likewise, the radial amplitudes of the lower components Eq. (69) in the doublet have the same number of radial nodes. Therefore the radial amplitudes of the upper components have different radial nodes. In fact, for the eigenstate for which the pseudospin is unaligned with the pseudo-orbital angular momentum ($\kappa < 0$), we see from Eq. (89) that the spatial amplitudes of the upper and lower component have the same number of radial nodes, while for the eigenstate for which the pseudospin is aligned with the pseudo-orbital angular momentum ($\kappa > 0$), we see from Eq. (89) that the spatial amplitude of the upper

component has one radial node less than the spatial amplitude of the lower component and, therefore, has one radial node less than the spatial amplitude of the upper component of its partner in the pseudospin doublet. For example, the spatial amplitudes of the lower components of the $d_{3/2}$, $s_{1/2}$ eigenstates and the spatial amplitude of the upper component of $s_{1/2}$ eigenstates all have the same radial quantum number, whereas the spatial amplitude of the upper component of the $d_{3/2}$ eigenstate has one less radial node than these amplitudes. That is why states with different radial nodes, for example, the $1s_{1/2}$ and $0d_{3/2}$ states, are pseudospin partners. The relations between the radial nodes is summarized in Eqs. (71).

Thus the identification of pseudospin as a relativistic symmetry of the Dirac Hamiltonian provides a natural explanation for the structure of radial nodes occurring in pseudospin doublets of normal-parity states. The key point in this explanation is that pseudospin symmetry implies that the radial amplitudes of the lower components of the two states in the doublet are equal, and those in turn govern the radial nodes of the corresponding upper components.

The states with radial quantum number zero and $\kappa < 0$ need special attention. These states have spin aligned with the orbital angular momentum but pseudospin unaligned with the pseudo-orbital angular momentum. The radial amplitude of the upper component of the spin partner of these states have the same number of radial nodes as argued above. However, the radial amplitude of the upper component of the pseudospin partner of these states must have one less radial quantum number but it clearly is not possible to have a negative number of radial nodes. Therefore the pseudospin partner of these particular states cannot be an eigenstate of the Dirac Hamiltonian. We shall discuss this issue in more detail in Section 7.2. The “intruder” states, discussed in the next section, have zero radial quantum numbers and are spin (pseudospin) aligned (anti-aligned) and fall into this category.

It is gratifying to note that characteristic features (e.g. radial and angular momentum quantum numbers) of the non-relativistic pseudospin partners, which seem at first ad hoc without an apparent reason, receive a proper justification once the relativistic origin of pseudospin symmetry in nuclei is taken into consideration.

3.3. Conditions for bound states

3.3.1. Conditions for bound positive energy states

From Eq. (83) we know that $G_\kappa(r)F_\kappa(r)$ goes to zero for r small and large. For a bound state to exist, $G_\kappa(r)F_\kappa(r)$ cannot be identically zero for all r . Hence the derivative $(G_\kappa(r)F_\kappa(r))'$ must be negative for some range of r and positive for some other range of r . For positive energy eigenstates $A(r)$ is always positive and $B(r)$ is negative for large r and therefore, by Eq. (86), is positive for large r . In order that $(G_\kappa(r)F_\kappa(r))'$ becomes negative, $B(r)$ must become positive for some r since $A(r)$ is always positive. If $V_S(r) + V_V(r) = 0$, $B(r) = E - M < 0$ for all r and therefore no bound positive energy states will exist in the pseudospin symmetry limit. Hence, for nuclei to exist, pseudospin must be broken! Also since there are no bound positive energy states in the symmetry limit, only continuum states, one cannot do perturbation theory about the pseudospin symmetry limit. Therefore approximate pseudospin symmetry is necessarily non-perturbative [17–19]. This non-perturbative nature of pseudospin symmetry makes it both very difficult to analyze but, at the same time, very interesting since it is so different from normal symmetry breaking. This is another large difference between spin and pseudospin symmetry; perturbation theory is possible for spin symmetry for positive energy eigenstates whereas it is not for pseudospin symmetry.

3.3.2. Conditions for bound negative energy states

For negative energy states, as stated above, $A(r)$ and $-B(r)$ change roles. Therefore, in the limit of pseudospin symmetry there are bound negative energy states, but in the limit of spin symmetry there are no bound negative energy states.

4. Pseudospin symmetry in nuclei

One need only look at the single-particle spectrum in the original book on the nuclear shell model by Meyer and Jensen, which is reproduced in Fig. 1, to observe the pseudospin degeneracies [20].

First we note the large energy gaps between major shells labeled by $N\hbar\omega$ where N is the number of harmonic oscillator quanta and $\hbar\omega$ is the energy splitting between major shells, $\hbar\omega \approx 41A^{-1/3}$. Second we note the large energy splittings between the spin–orbit partners; i.e., $1p_{1/2}$ and $1p_{3/2}$ levels, $1d_{3/2}$ and $1d_{5/2}$ levels, $1f_{5/2}$ and $1f_{7/2}$ levels, $1g_{7/2}$ and $1g_{9/2}$ levels, etc., using the notation $n_r\ell j$.

This spin–orbit splitting increases with orbital angular momentum leading to the fact that $1g_{9/2}$ is pushed down so that it becomes a member of the lower major shell, thereby earning the name of “intruder”, while $1g_{7/2}$ remains in the original major shell. This pattern is repeated for levels with larger orbital angular momentum and radial quantum number. On the other hand levels such as $1d_{3/2}$ and $2s_{1/2}$, $1f_{5/2}$ and $2p_{3/2}$, $1g_{7/2}$ and $2d_{5/2}$, $2d_{3/2}$ and $3s_{1/2}$, etc., are clumped together. From Eqs. (70) and (71) we see that these doublets are pseudospin doublets with pseudo-orbital angular momenta $\tilde{\ell} = 1, 2, 3, 1$ and pseudo-radial quantum numbers $\tilde{n}_r = 2, 2, 2, 3$, respectively, as discussed in the last subsection. The pseudo-orbital angular momenta agree with the original pseudo-orbital angular momenta assignments based on the original experimental observation [4,5].

Detailed scrutiny of empirical single-particle spectra confirms the small pseudospin splittings. For example, in Fig. 2 we show the energy splitting

$$\Delta E_{\tilde{n}_r, \tilde{\ell}} = E_{\tilde{n}_r, \tilde{\ell}, j=\tilde{\ell}-1/2} - E_{\tilde{n}_r, \tilde{\ell}, j=\tilde{\ell}+1/2} \quad (93)$$

of the $1d_{5/2}$ and $0g_{7/2}$ doublets ($\tilde{n}_r=1, \tilde{\ell}=3$) (solid dots) and for the $2s_{1/2}$ and $1d_{3/2}$ doublets ($\tilde{n}_r=2, \tilde{\ell}=1$) (solid squares) in units of $\hbar\omega$ for the Sb isotopes as a function of the isospin T [21]. In Fig. 3 we show the energy splittings for the $2s_{1/2}$ and $1d_{3/2}$ doublets ($\tilde{n}_r=2, \tilde{\ell}=1$) in the Tl isotopes. The energy splittings are less than 13% of the shell model energy gap.

Pseudospin symmetry has been observed in deformed nuclei as well. Again the original Nilsson (harmonic oscillator) levels in nuclei exhibit the feature that the states with asymptotic quantum numbers $[N, n_3, A]\Omega = A + \frac{1}{2}$ and $[N, n_3, A+2]\Omega = A - \frac{1}{2}$ were quasi-degenerate independent of the deformation [22,23]. These quasi-degeneracies were also observed for deformed orbitals calculated from a realistic Woods–Saxon deformed potential [24] and deformed orbitals calculated in the relativistic mean field approximation of a relativistic field theory [25]. An example of the latter is shown in Fig. 4 where the single neutron energies, $\varepsilon = E - M$, of neutron pseudospin partners are plotted versus the deformation, β , for ^{154}Dy . In this figure the orbits are labeled by their pseudospin quantum numbers, $[\tilde{N}, \tilde{n}_z, \tilde{A}]$, and the orientation of the pseudospin is denoted by the arrows.

In Fig. 5 the empirical splitting (divided by $\hbar\omega$) of the $[4, 0, 2]_{\frac{5}{2}}$ and $[4, 0, 4]_{\frac{7}{2}}(\tilde{A}=3)$ orbits in the thulium isotopes are plotted while in Fig. 6 the empirical splitting (divided by $\hbar\omega$) of the orbits and the $[5, 1, 0]_{\frac{1}{2}}$ and $[5, 1, 2]_{\frac{3}{2}}(\tilde{A}=1)$ orbits in the osmium isotopes are plotted. The energy splittings of the deformed doublets are less than 7% of the harmonic oscillator energy gap.

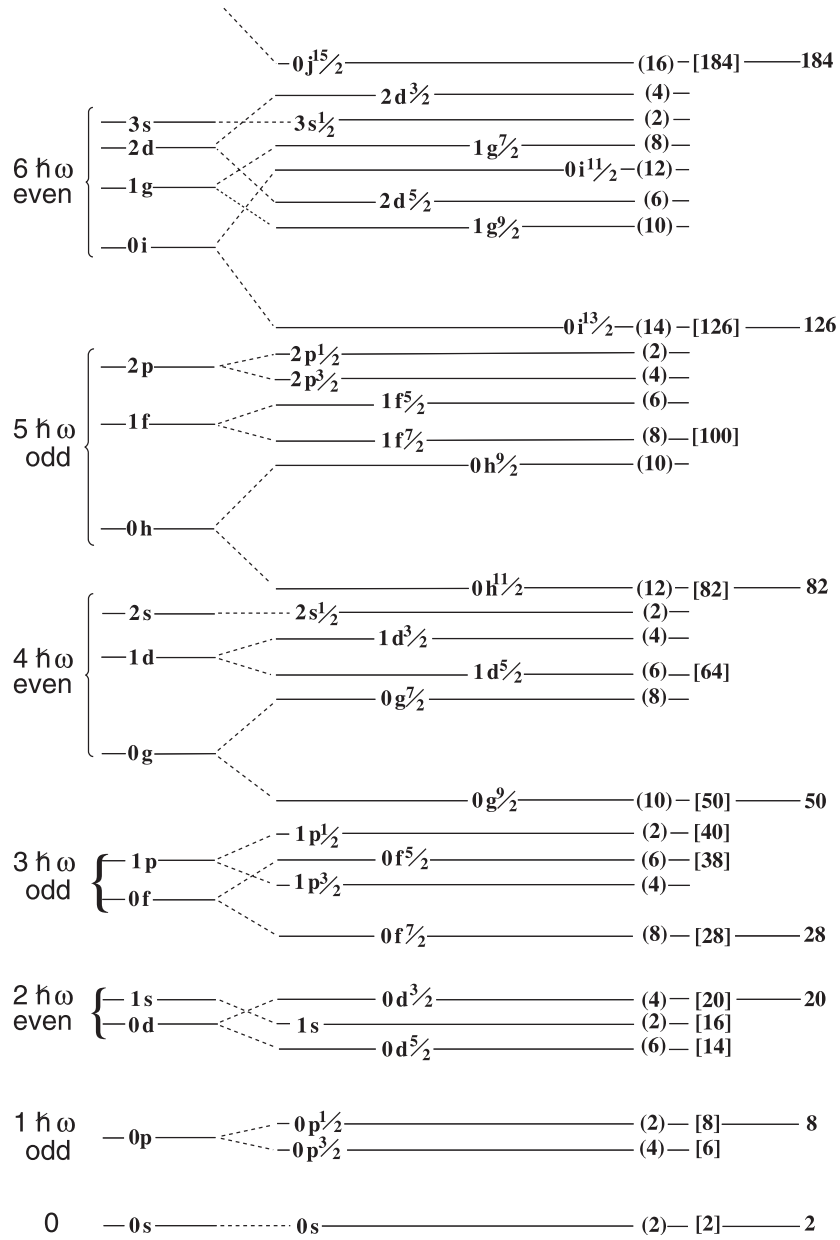


Fig. 1. A schematic single-nucleon spectrum [20]. The notation for the orbitals is $n_r \ell j$.

In Fig. 7 the spectrum of the ground state band and the neighboring band in ^{187}Os are plotted. The states of the two bands are almost degenerate in energy. The two bands are built on the $[5, 1, 0]_{\frac{1}{2}}$ and $[5, 1, 2]_{\frac{3}{2}}$ deformed orbitals respectively which are pseudospin doublets with $\tilde{\Lambda} = 1$ and $\Omega = \tilde{\Lambda} \pm \frac{1}{2}$.

The striking aspect of this discovery is that the quasi-degeneracies are almost independent of deformation (see Fig. 4 for example). This feature led to an explosion of papers linking pseudospin with

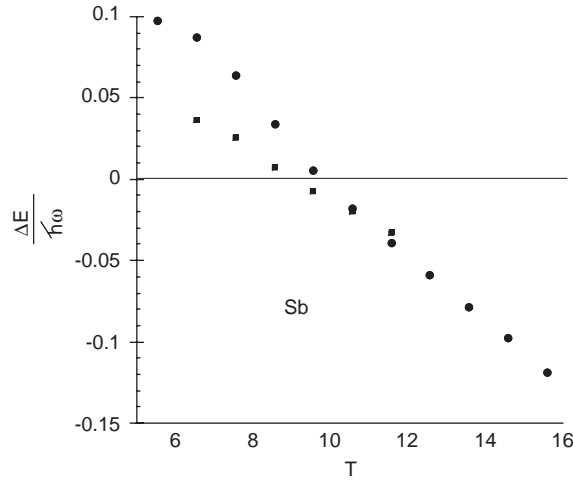


Fig. 2. The energy splitting $\Delta E_{\tilde{n}_r, \tilde{\ell}} / \hbar\omega$ for the $1d_{5/2}$ and $0g_{7/2}$ doublets ($\tilde{n}_r = 1, \tilde{\ell} = 3$) (solid dots) and for the $2s_{1/2}$ and $1d_{3/2}$ doublets ($\tilde{n}_r = 2, \tilde{\ell} = 1$) doublet (solid squares) in the Sb isotopes as a function of the isospin T . Data from [21].

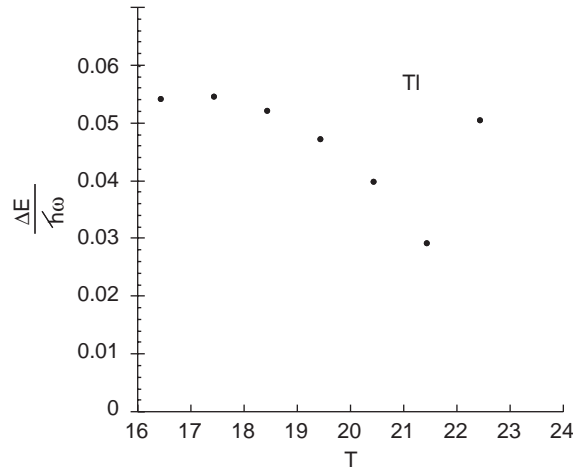


Fig. 3. The energy splitting $\Delta E_{\tilde{n}_r, \tilde{\ell}} / \hbar\omega$ for the $2s_{1/2}$ and $1d_{3/2}$ doublets ($\tilde{n}_r = 2, \tilde{\ell} = 1$) doublet (solid dots) in the Tl isotopes as a function of the isospin T . Data from [21].

superdeformed bands. The complete alignment of pseudospin along the axis of rotation was cited as partially responsible for superdeformed bands in different nuclei having virtually identical moments of inertia [27]. These bands appeared in odd, even–even, and odd–odd nuclei [28–44,26,45]. The triaxial harmonic oscillator was also shown to have pseudospin symmetry as well [46,47].

In the original observations of pseudospin doublets in spherical nuclei [4,5], it was noted that the surface delta interaction [48–50], which was considered a good phenomenological effective

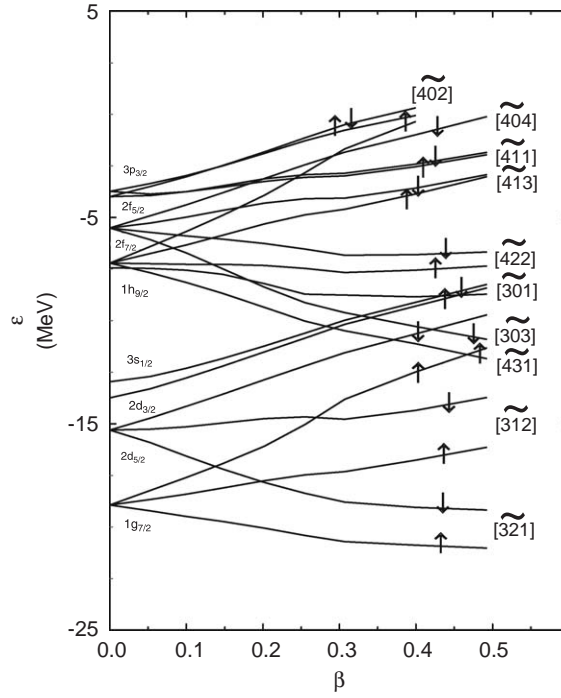


Fig. 4. The calculated single neutron energies, $\varepsilon = E - M$, of neutron pseudospin partners versus the deformation, β , for ^{154}Dy [25]. The orbits are labeled by their pseudospin quantum numbers, $[\tilde{N}, \tilde{n}_z, \tilde{A}]$, and the orientation of the pseudospin is denoted by the arrows.

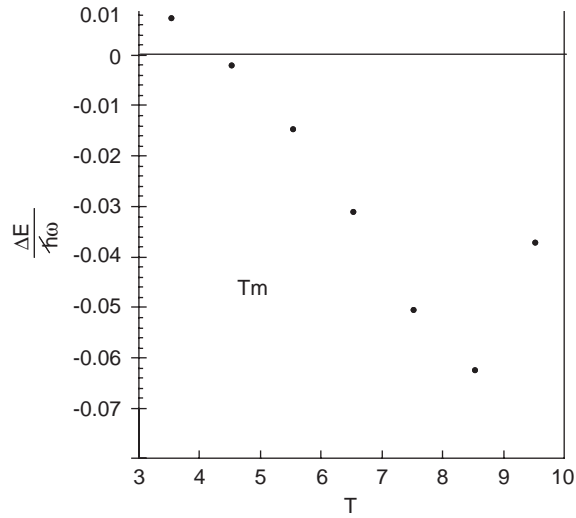


Fig. 5. The energy splitting $\Delta E_{\tilde{A}} / \hbar\omega$ for the $\tilde{n}_r = 1$, $\tilde{A} = 3$ doublet (solid dots) in the tellurium isotopes as a function of the isospin T . Data from [21].

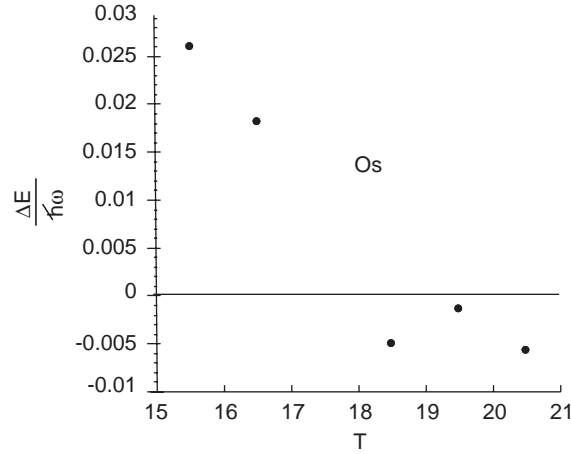


Fig. 6. The energy splitting $\Delta E_{\tilde{A}}/\hbar\omega$ for the $\tilde{n}_r = 1$, $\tilde{A} = 1$ doublet (solid dots) in the osmium isotopes as a function of the isospin T . Data from [21].

	(keV)		(keV)
<u>(9/2⁻)</u>	<u>508.22</u>	<u>(11/2⁻)</u>	<u>511.6</u>
<u>(7/2⁻)</u>	<u>333.26</u>	<u>(9/2⁻)</u>	<u>341.5</u>
<u>5/2⁻</u>	<u>187.40</u>	<u>7/2⁻</u>	<u>190.60</u>
<u>3/2⁻</u>	<u>74.33</u>	<u>5/2⁻</u>	<u>75.04</u>
<u>1/2⁻</u>	<u>0</u>	<u>3/2⁻</u>	<u>9.746</u>
<u>[510]1/2</u>		<u>[512]3/2</u>	
$\tilde{A}=1$			

Fig. 7. The spectrum of the ground state band (pseudospin unaligned) and the neighboring band (pseudospin aligned) in ^{187}Os which are based on a deformed pseudospin doublet with $\tilde{A} = 1$ [26].

interaction in nuclei, conserved pseudospin and pseudo-orbital angular momentum [51]. Calculations using a shell model truncation scheme based on conserved pseudospin and pseudo-orbital angular momentum determined the many-nucleon energy spectrum and eigenstates for the $N = 82$ isotones [52].

Experiments inspired by this newly found symmetry demonstrated reasonable agreement with these predictions [53].

By combining isospin symmetry with the pseudospin symmetry, a pseudo-SU(4) symmetry is created. Pseudo-SU(4) symmetry investigations have been limited [54–56] and we shall discuss the relativistic generalization in Section 10.

A big leap was made by including all the normal parity orbitals in a major shell (See Fig. 1) into one representation of an SU(3) group, called pseudo-SU(3) [4,5]. A shell model truncation based on pseudo-SU(3) has been used extensively with increasing sophistication and success in explaining the spectroscopy of heavy nuclei [54,57–64].

With this success attempts were made to forge a deeper understanding of pseudospin symmetry. First transformations between the shell model basis and the pseudo-shell model basis were explored and originally the unitary transformation $U_r = \vec{\sigma} \cdot \vec{r}/r$ [23] was suggested. This transformation predicts correctly that the orbital angular momenta in the doublet differ by two units, but also predicts that the two states in the doublet have the same radial wavefunctions which certainly is not the case. The transformation $U_a = \vec{\sigma} \cdot \vec{a}/a$ [65], where $\vec{a} = \vec{p} - i\vec{r}$, inspired by the harmonic oscillator, does change both the radial quantum number and the orbital angular momentum but is not hermitean. The helicity transformation U_p was originally proposed on the basis that it is both unitary and translationally invariant [8] and was also vindicated by the subsequent discovery that pseudospin symmetry is an approximate symmetry of the Dirac Hamiltonian [6] because, from Eq. (52), the projection of the pseudospin generators onto the non-relativistic upper components is $\tilde{S}_i(1+\beta)/2 = U_p s_i U_p$, where $(1+\beta)/2$ is the Dirac operator that projects onto the upper component. With this helicity transformation it was shown that, in the harmonic oscillator, pseudospin is conserved if the spin–orbit single particle potential and angular momentum single-particle potential are in the combination

$$H_{so} = 2\hat{\ell} \cdot \hat{s} + 0.5\hat{\ell} \cdot \hat{\ell} \quad (94)$$

and that the shell model and the Nilsson model approximately satisfy this condition [66]. Furthermore this transformation from the spin basis to the pseudospin basis was shown to reduce the large spin–orbit interaction in relativistic mean field calculations into a small pseudospin–orbit interaction [8].

However, the status of pseudospin symmetry provoked the statement “It should be emphasized that at the present time there is no deeper understanding of the origin of these (approximate) degeneracies. They are just facts which, as we shall see, can be exploited.” [27]. This status quo was broken when pseudospin symmetry was shown to be a symmetry of the Dirac Hamiltonian [6].

We shall now discuss relativistic nuclear theories and the extent to which they support approximate pseudospin symmetry in nuclei.

5. Relativistic nuclear theories

There are two types of relativistic theories that have been used to describe relativistic dynamics in nuclei. The first is the relativistic theory of nucleons interacting by exchanging mesons, which has a long history [67–71]. The other is a theory of relativistic nucleons interacting via point contact interactions [72–75]. We shall briefly review both types.

5.1. Relativistic field theory

A simple version of this type of model contains nucleon fields $\psi(x_\mu)$ and time independent neutral scalar ($\phi(\vec{r})$) and vector ($V^\mu(\vec{r})$) mesons. The lagrangian density for this model is given by

$$\begin{aligned} \mathcal{L} = & \bar{\psi}(x_\mu)[\gamma_\mu(-\hbar c i \partial^\mu + g_V V_\mu(\vec{r})) + (Mc^2 - g_S \phi(\vec{r}))]\psi(x_\mu) \\ & + \frac{1}{2}(\partial_\mu \phi(\vec{r})\partial^\mu \phi(\vec{r}) - m_S^2 \phi(\vec{r})^2) - \frac{1}{3!}\kappa \phi(\vec{r})^3 \\ & - \frac{1}{4!}\lambda \phi(\vec{r})^4 - \frac{1}{4}F_{\mu\nu}(\vec{r})F^{\mu\nu}(\vec{r}) + \frac{1}{2}m_V^2 V_\mu(\vec{r})V^\mu(\vec{r}) , \end{aligned} \quad (95)$$

where $F^{\mu\nu}(\vec{r}) \equiv \partial^\mu V^\nu(\vec{r}) - \partial^\nu V^\mu(\vec{r})$. The coupling constants, g_S , g_V , κ , λ , and the scalar and vector meson masses m_S , m_V , are determined (in principle) from experimental observables.

Isovector meson fields can be included which will produce isovector scalar and vector potentials.

Other parts of the nucleon–nucleon interaction average essentially to zero in spin-saturated nuclear matter and may be incorporated as refinements to the present model. The important point is that even in more complete models, the dynamics generated by scalar and vector mesons will remain.

The field equations for this model follow from the Euler–Lagrange equations and can be written as

$$(\partial_\mu \partial^\mu + m_S^2)\phi(\vec{r}) + \frac{1}{2}\kappa \phi(\vec{r})^2 + \frac{1}{6}\lambda \phi(\vec{r})^3 = g_S \bar{\psi}(x_\mu)\psi(x_\mu) , \quad (96a)$$

$$\partial_\mu F^{\nu\mu}(\vec{r}) + m_V^2 V_\mu(\vec{r}) = g_V \bar{\psi}(x_\mu)\gamma^\mu \psi(x_\mu) , \quad (96b)$$

$$[\gamma^\mu(-i\hbar c \partial_\mu + g_V V_\mu(\vec{r})) + (Mc^2 - g_S \phi(\vec{r}))]\psi(\vec{r}) = 0 . \quad (96c)$$

Eq. (96a) is a Klein–Gordon equation with a scalar source term and nonlinear scalar self-interactions. Eq. (96b) looks like massive QED with the conserved nucleon current

$$B^\mu(x_\mu) = \bar{\psi}(x_\mu)\gamma^\mu \psi(x_\mu), \quad \partial_\mu B^\mu(x_\mu) = 0 , \quad (97)$$

rather than the (conserved) electromagnetic current as the source. Finally, Eq. (96c) is the Dirac equation with scalar and vector fields entering in a minimal fashion. The solutions (if they exist) of these nonlinear equations quantum field equations are very complicated. An approximate but non-perturbative solution is the Hartree approximation in which the average of the meson fields are replaced by classical fields,

$$-g_S \phi(\vec{r}) \rightarrow -g_S \langle \phi \rangle \equiv V_S(\vec{r}), \quad g_V \langle V^\mu(\vec{r}) \rangle \rightarrow g_V \langle V^\mu(\vec{r}) \rangle \equiv (V_V(\vec{r}), 0) . \quad (98)$$

The average value of $V^i(\vec{r})$, $i = 1, 2, 3$, vanishes if parity conservation is assumed. Therefore the Dirac equation in Eq. (96c) becomes equivalent to the Dirac equation in Eq. (1).

5.2. Relativistic point coupling model

The model consists of four-, six-, and eight-fermion point couplings leading to scalar and vector densities with both isoscalar and isovector components and derivatives of the densities to simulate the finite ranges of the mesonic interactions, but no explicit meson fields. The Lagrangian density is given by

$$\mathcal{L} = \mathcal{L}_{\text{free}} + \mathcal{L}_{4f} + \mathcal{L}_{\text{hot}} + \mathcal{L}_{\text{der}} + \mathcal{L}_{\text{em}} , \quad (99)$$

where \mathcal{L}_{em} is the electromagnetic term, and

$$\mathcal{L}_{\text{free}} = \bar{\psi}(x_\mu)[-i\hbar c \gamma_\mu \partial^\mu + Mc^2]\psi(x_\mu) , \quad (100a)$$

$$\begin{aligned}\mathcal{L}_{4f} = & -\frac{1}{2}\alpha_S(\bar{\psi}\psi)(\bar{\psi}\psi) - \frac{1}{2}\alpha_V(\bar{\psi}\gamma_\mu\psi)(\bar{\psi}\gamma^\mu\psi) \\ & - \frac{1}{2}\alpha_{TS}(\bar{\psi}\vec{\tau}\psi) \cdot (\bar{\psi}\vec{\tau}\psi) - \frac{1}{2}\alpha_{TV}(\bar{\psi}\vec{\tau}\gamma_\mu\psi) \cdot (\bar{\psi}\vec{\tau}\gamma^\mu\psi) ,\end{aligned}\quad (100b)$$

$$\mathcal{L}_{\text{hot}} = -\frac{1}{3}\beta_S(\bar{\psi}\psi)^3 - \frac{1}{4}\gamma_S(\bar{\psi}\psi)^4 - \frac{1}{4}\gamma_V[(\bar{\psi}\gamma_\mu\psi)(\bar{\psi}\gamma^\mu\psi)]^2 , \quad (100c)$$

$$\mathcal{L}_{\text{der}} = -\frac{1}{2}\delta_S(\partial_\nu\bar{\psi}\psi)(\partial^\nu\bar{\psi}\psi) - \frac{1}{2}\delta_V(\partial_\nu\bar{\psi}\gamma_\mu\psi)(\partial^\nu\bar{\psi}\gamma^\mu\psi) , \quad (100d)$$

where the x_μ of the nucleon fields have been suppressed for convenience.

In these equations, $\alpha_{S,V}$, $\alpha_{TS,TV}$, β_S , $\gamma_{S,V}$, $\delta_{S,V}$ are the strengths of the nine different contact interactions with subscripts S and V referring to isoscalar scalar and vector potentials and subscripts TS and TV referring to isovector scalar and vector potentials. The physical makeup of \mathcal{L} is that \mathcal{L}_{4f} is a four-fermion interaction, while \mathcal{L}_{hot} contains higher order six-fermion and eight-fermion interactions, and \mathcal{L}_{der} contains derivatives in the nucleon densities.

Again the solution of this interacting many-nucleon system is not possible so a Dirac–Hartree approximation is made which leads to a Dirac equation with the following potentials:

$$V_S(\vec{r}) = \alpha_S\rho_S(\vec{r}) + \beta_S\rho_S(\vec{r})^2 + \gamma_S\rho_S(\vec{r})^3 + \delta_S\Delta\rho_S(\vec{r}) , \quad (101a)$$

$$V_V(\vec{r}) = \alpha_V\rho_V(\vec{r}) + \gamma_V\rho_V(\vec{r})^3 + \delta_V\Delta\rho_V(\vec{r}) , \quad (101b)$$

$$V_{TS}(\vec{r}) = \alpha_{TS}\rho_{TS}(\vec{r}) , \quad (101c)$$

$$V_{TV}(\vec{r}) = \alpha_{TV}\rho_{TV}(\vec{r}) , \quad (101d)$$

where $\Delta = \partial_i\partial_i$, the Laplacian, and $V_{S,V}(\vec{r})$ are the isoscalar–scalar potential and isoscalar–vector potential, respectively, and $V_{TS,TV}(\vec{r})$ are the isovector–scalar potential and the isovector–vector potential, and $\rho_{S,V}(\vec{r})$ are the isoscalar–scalar and isoscalar–vector nuclear density, respectively, and $\rho_{TS,TV}(\vec{r})$ are the isovector–scalar nuclear density and the isovector–vector nuclear density, respectively. These nuclear densities are determined self consistently from the upper and lower components of the Dirac eigenfunctions ($g_a^\pm(\vec{r})$, $f_a^\pm(\vec{r})$) where a represents all the quantum numbers. For example, the vector density becomes

$$\rho_V(\vec{r}) = \sum_a^{\text{occ.}} [g_a^+(\vec{r})^2 + g_a^-(\vec{r})^2 + f_a^+(\vec{r})^2 + f_a^-(\vec{r})^2] , \quad (102)$$

while the scalar density becomes

$$\rho_S(\vec{r}) = \sum_a^{\text{occ.}} [g_a^+(\vec{r})^2 + g_a^-(\vec{r})^2 - f_a^+(\vec{r})^2 - f_a^-(\vec{r})^2] , \quad (103)$$

where the sum is over all occupied states.

5.3. Features of the relativistic mean field

The features of the relativistic potentials derived from either the relativistic field theory or the relativistic contact interaction model are very similar since they both determine the parameters of the models from nuclear properties [67,74]. In Fig. 8 the isoscalar vector and scalar potentials, $V_S(r)$, $V_V(r)$ (solid line),

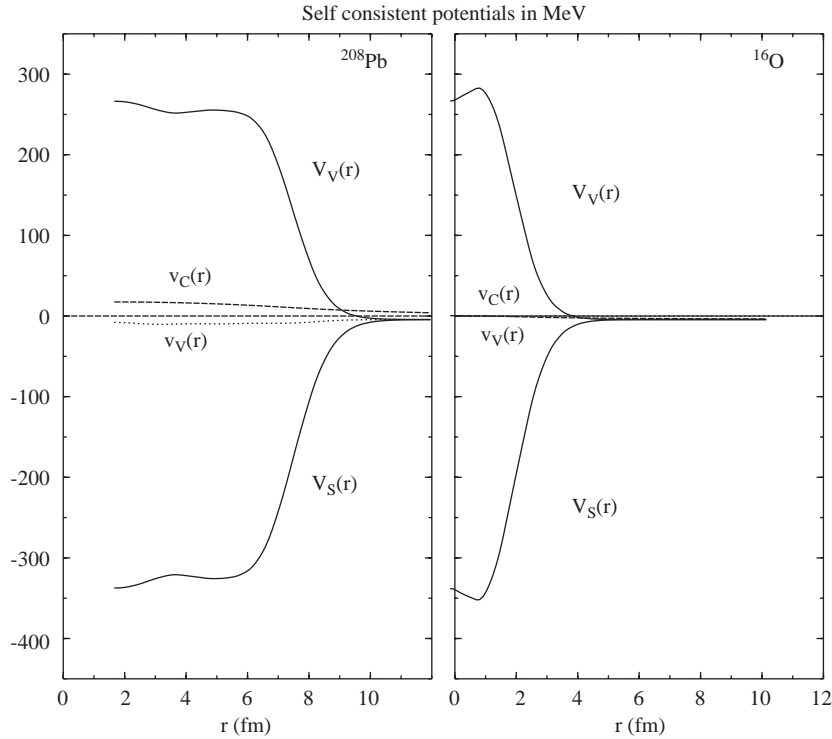


Fig. 8. The mean field potentials as a function of radius r in Fermi. The isoscalar scalar and vector nuclear potential are solid lines, the isovector vector nuclear potential is the dotted line, and the Coulomb potential is the dashed line [76].

are shown for ^{16}O and ^{16}Pb . In both cases the scalar potential is attractive and large while the vector potentials are repulsive and large, but they are similar shape and magnitude, $V_S(r) \approx -V_V(r)$. This is consistent with approximate pseudospin symmetry.

The isovector vector nuclear potential, $v_V(r)$ (dotted), and the Coulomb potential, $v_C(r)$ (dashed), are also shown for each nucleus. These are both vector potentials so they do not satisfy the pseudospin condition but are very small compared to the isoscalar potentials. We shall discuss the isospin dependence of pseudospin symmetry in Section 11. Isospin dependence of pseudospin symmetry will become more important as we increase our knowledge of nuclei far from stability from experiments at rare isotope accelerators.

6. QCD sum rules

QCD sum rules have been used to show that $V_S \approx -V_V$ in nuclear matter [77]. Since the derivation is too complex to repeat here, we shall only attempt to justify the result.

The vector potential will be proportional to the nuclear matter density, Eq. (97), which in nuclear matter is uniform, $V_V \approx \rho_N$. The value of ρ_N is taken to be the central matter density of nuclei which has been measured in electron scattering from nuclei.

In order to determine the scalar potential we need to know the nuclear scalar density which is the term on the right-hand side of the equation in Eq. (96a). There is no direct measurement of the nuclear scalar density, but the scalar density of quarks in a nucleon can be measured experimentally. This scalar density of quarks is given in terms of what is called the sigma term

$$\sigma_N = 2m_q(\langle N|\bar{q}q|N\rangle - \langle 0|\bar{q}q|0\rangle) , \quad (104)$$

where q is quark field operator, $\bar{q} = q^\dagger \gamma_0$, m_q is the quark mass, $|N\rangle$ is the nucleon state, and $|0\rangle$ is the vacuum state. This sigma term can be measured in pion–nucleon scattering [78,79] and, after a sophisticated analysis, is determined to be $\sigma_N \approx 45 \pm 8$ MeV. Averaging over all the nucleons in nuclear matter and ignoring nuclear interactions,

$$\sigma_N \rho_N = 2m_q(\langle \bar{q}q \rangle_{\rho_N} - \langle \bar{q}q \rangle_{\text{vac}}) . \quad (105)$$

The scalar density of quarks in nuclear matter relative to the vacuum is then

$$\frac{\langle \bar{q}q \rangle_{\rho_N}}{\langle \bar{q}q \rangle_{\text{vac}}} = 1 + \frac{\sigma_N \rho_N}{2m_q \langle \bar{q}q \rangle_{\text{vac}}} = 1 - \frac{\sigma_N \rho_N}{m_\pi^2 f_\pi^2} , \quad (106)$$

where the last term follows from the Gell–Mann–Oakes–Renner relation [80],

$$2m_q \langle \bar{q}q \rangle_{\text{vac}} = -m_\pi^2 f_\pi^2 . \quad (107)$$

Both the nucleon mass and the scalar potential are Lorentz scalars. The effective mass will be proportional to the left-hand side of Eq. (106) with the first term on the right-hand side proportional to the mass of the nucleon and the second proportional to the scalar potential.

The detailed QCD sum rule gives

$$V_S = -\frac{4\pi^2 \sigma_N \rho_N}{M^2 m_q} , \quad (108a)$$

$$V_V = \frac{32\pi^2 \rho_N}{M^2} . \quad (108b)$$

Since all the quantities on the right-hand side of Eq. (107) are positive, the scalar potential is attractive and the vector potential is repulsive, just as one finds in relativistic mean field models. Furthermore the ratio becomes

$$\frac{V_S}{V_V} = -\frac{\sigma_N}{8m_q} \approx -1.1 , \quad (109)$$

using accepted values of the average quark mass in the proton (≈ 5 MeV) and the value of σ_N (≈ 45 MeV), which is uncannily close to the ratio of the potentials at the center of the nucleus as determined in relativistic mean field models (See Fig. 8), and indicative of pseudospin symmetry. Also the negative sign originates in the vacuum expectation of the quark scalar density given in Eq. (107). These features suggest that perhaps pseudospin has a more fundamental foundation in terms of QCD.

7. Testing nuclear eigenstates for pseudospin symmetry

Although pseudospin symmetry has been observed in the energy spectra of nuclei, there has not been an attempt to test the eigenstates of nuclei for good pseudospin until recently when the relativistic origins of the symmetry were revealed and the generators determined. There have been two types of test. One is to examine the Dirac eigenstates determined in relativistic models discussed in Section 5 and see how well they fit the relationships between amplitudes given in Eqs. (53) [81,25,82–87]. We shall discuss these comparisons in the next four sections 7.1–7.4. The other type of test is an empirical one in which we ask what predictions in transition strengths follow from pseudospin symmetry. We shall discuss some of the empirical relationships predicted by pseudospin and their comparison with nuclear data in the next two sections, Sections 8 and 9.

7.1. Test of realistic eigenfunctions with spherical symmetry

The Dirac eigenfunctions used in the following tests are from relativistic mean field approximations of the relativistic point coupling model [81] for neutrons in ^{208}Pb but similar conclusions hold for the protons as well.

7.1.1. Lower amplitudes

The most striking predictions of pseudospin symmetry and the most straightforward to check is that the lower amplitudes of the states in the doublet are equal,

$$f_{\tilde{n}_r, \tilde{\ell}, j=\tilde{\ell}+1/2}(r) = f_{\tilde{n}_r, \tilde{\ell}, j=\tilde{\ell}-1/2}(r) = f_{\tilde{n}_r, \tilde{\ell}}(r) \quad (110)$$

as seen in Eq. (69).

In Fig. 9a and b, the upper and lower amplitudes $g(r)$ and $f(r)$ of the $1s_{1/2}$ (solid line) and $0d_{3/2}$ Dirac eigenfunctions (dashed line) ($\tilde{n}_r = 1, \tilde{\ell} = 1$) are plotted as a function of the radial coordinate r [81]. The upper amplitudes of the $1s_{1/2}$ and $0d_{3/2}$ Dirac eigenfunctions have different nodes and radial shape. However the lower amplitudes are almost identical except on the nuclear surface. In Fig. 9c and d the upper and lower amplitudes $g(r)$ and $f(r)$ of the $2s_{1/2}$ and $1d_{3/2}$ Dirac eigenfunctions ($\tilde{n}_r = 2, \tilde{\ell} = 1$) are plotted as a function the radial coordinate r . The agreement between the lower amplitudes is even better than for $\tilde{n}_r = 1$.

Similar plots are made for the upper and lower amplitudes $g(r)$ and $f(r)$ of the $1p_{3/2}$ (solid line) and $0f_{5/2}$ Dirac eigenfunctions (dashed line) ($\tilde{n}_r = 1, \tilde{\ell} = 2$), the $2p_{3/2}$ (solid line) and $1f_{5/2}$ Dirac eigenfunctions (dashed line) ($\tilde{n}_r = 2, \tilde{\ell} = 2$) in Fig. 10, for the upper and lower amplitudes $g(r)$ and $f(r)$ of the $1d_{5/2}$ (solid line) and $0g_{7/2}$ Dirac eigenfunctions (dashed line) ($\tilde{n}_r = 1, \tilde{\ell} = 2$) in Fig. 11, and for the upper and lower amplitudes $g(r)$ and $f(r)$ of the $1f_{7/2}$ (solid line) and $0h_{9/2}$ Dirac eigenfunctions (dashed line) ($\tilde{n}_r = 1, \tilde{\ell} = 2$) in Fig. 12.

From Figs. 9 and 10 we conclude that, for the same pseudo-orbital angular momentum, pseudospin conservation improves as the binding energy decreases. Comparing Fig. 9d with Fig. 11b and comparing Fig. 10d with Fig. 12b we see that, for roughly the same binding energy, pseudospin conservation improves as the pseudo-orbital angular momentum decreases. These features can be derived from a simple square well potential [6].

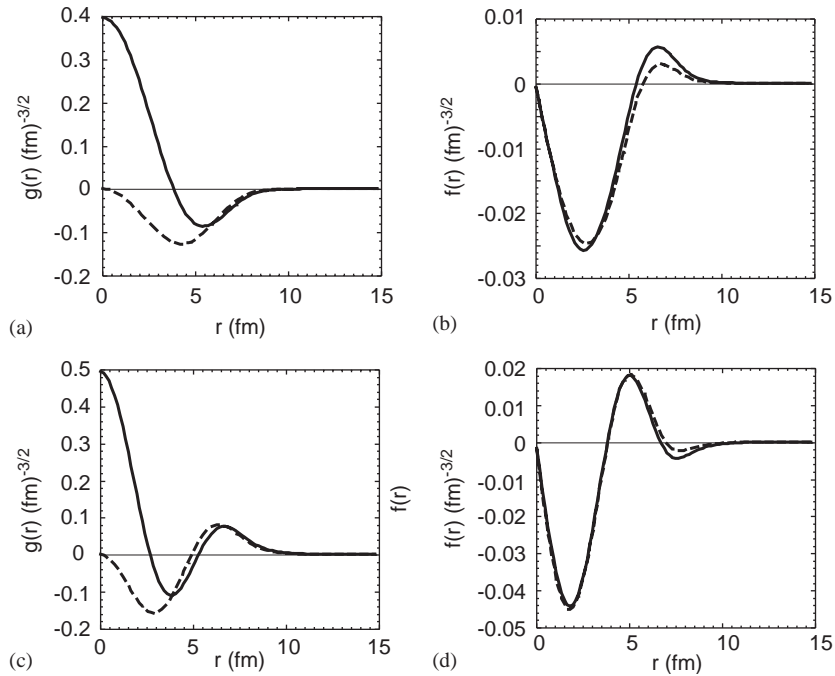


Fig. 9. (a) The upper amplitude $g(r)$ for the $1s_{1/2}$ (solid line) and $0d_{3/2}$ (dashed line) eigenfunctions, (b) the lower amplitude $f(r)$ for the $1s_{1/2}$ (solid line) and $0d_{3/2}$ (dashed line) eigenfunctions, (c) the upper amplitude $g(r)$ for the $2s_{1/2}$ (solid line) and $1d_{3/2}$ (dashed line) eigenfunctions, and (d) the lower amplitude $f(r)$ for the $2s_{1/2}$ (solid line) and $1d_{3/2}$ (dashed line) eigenfunctions as a function the radial coordinate in Fermi (fm). All amplitudes are in $(fm)^{-3/2}$ [81].

We also note that the upper amplitudes for the pseudospin unaligned ($\kappa < 0$) eigenstates ($s_{1/2}$, $p_{3/2}$, $d_{5/2}$, $f_{7/2}$) have the same number of radial nodes as the lower amplitudes, while the upper amplitudes for pseudospin aligned ($\kappa > 0$) eigenstates ($d_{3/2}$, $f_{5/2}$, $g_{7/2}$, $h_{9/2}$) have one radial node less than the lower amplitudes. This is in agreement with Eq. (89).

7.1.2. Upper amplitudes

Recently the differential relations in Eqs. (66) satisfied by the upper components of the Dirac eigenfunctions in the pseudospin symmetry limit have been tested for the pseudospin doublets in spherical nuclei using realistic eigenfunctions determined in relativistic mean field calculations [84,9,86].

In Fig. 13a the upper components for the $1s_{1/2}$ and $0d_{3/2}$ eigenfunctions are plotted ($\tilde{n}_r = 1$, $\tilde{\ell} = 1$); these eigenfunctions are very different in shape with different numbers of radial nodes. In Fig. 13b the differential relations for these eigenfunctions are plotted and we see a remarkable similarity between the two differential relations except near the nuclear surface. In Fig. 13c the upper components for the $2s_{1/2}$ and $1d_{3/2}$ eigenfunctions are plotted ($\tilde{n}_r = 2$, $\tilde{\ell} = 1$); likewise these eigenfunctions are very different in shape. In Fig. 13d the differential relations for these eigenfunctions are plotted and we see even better agreement between the two differential relations than for $\tilde{n}_r = 1$. In Figs. 14–16 similar tests are made for higher radial quantum numbers and larger pseudo-orbital angular momentum [9]. The pseudospin violation decreases for increasing radial quantum number but decreasing pseudo-orbital

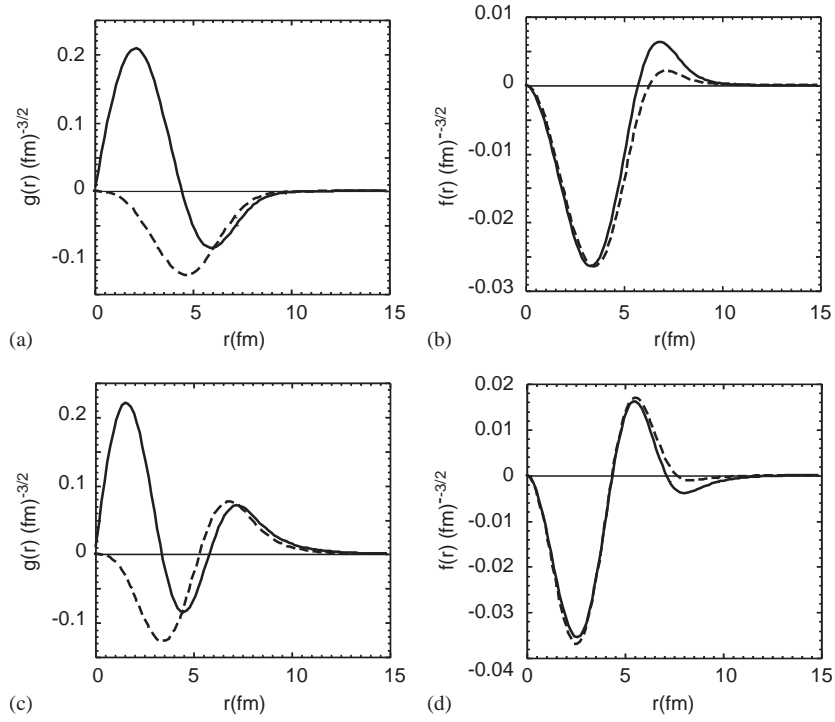


Fig. 10. (a) The upper amplitude $g(r)$ for the $1p_{3/2}$ (solid line) and $0f_{5/2}$ (dashed line) eigenfunctions, (b) the lower amplitude $f(r)$ for the $1p_{3/2}$ (solid line) and $0f_{5/2}$ (dashed line) eigenfunctions, (c) the upper amplitude $g(r)$ for the $2p_{3/2}$ (solid line) and $1f_{5/2}$ (dashed line) eigenfunctions, and (d) the lower amplitude $f(r)$ for the $2p_{3/2}$ (solid line) and $1f_{5/2}$ (dashed line) eigenfunctions as a function the radial coordinate in Fermi (fm). All amplitudes are in $(fm)^{-3/2}$ [81].

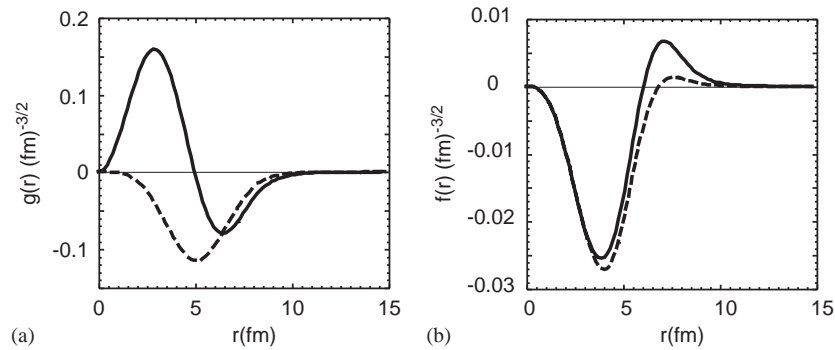


Fig. 11. (a) The upper amplitude $g(r)$ for the $1d_{5/2}$ (solid line) and $0g_{7/2}$ (dashed line) eigenfunctions, (b) the lower amplitude $f(r)$ for the $1d_{5/2}$ (solid line) and $0g_{7/2}$ (dashed line) eigenfunctions as a function the radial coordinate in Fermi (fm). All amplitudes are in $(fm)^{-3/2}$ [81].

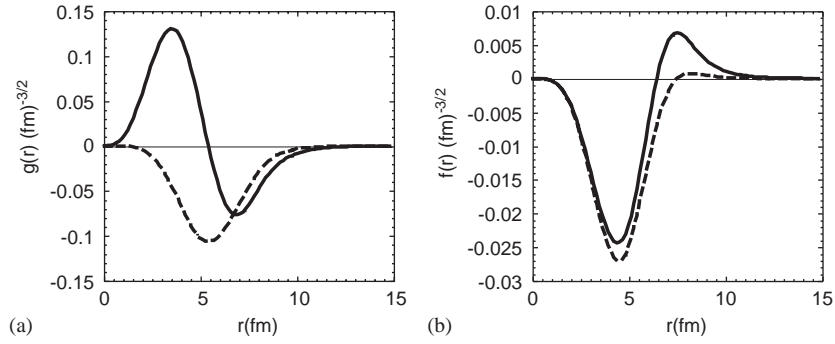


Fig. 12. (a) The upper amplitude $g(r)$ for the $1f_{7/2}$ (solid line) and $0h_{9/2}$ (dashed line) eigenfunctions, (b) the lower amplitude $f(r)$ for the $1f_{7/2}$ (solid line) and $0h_{9/2}$ (dashed line) eigenfunctions as a function the radial coordinate in Fermi (fm). All amplitudes are in $(\text{fm})^{-3/2}$ [81].

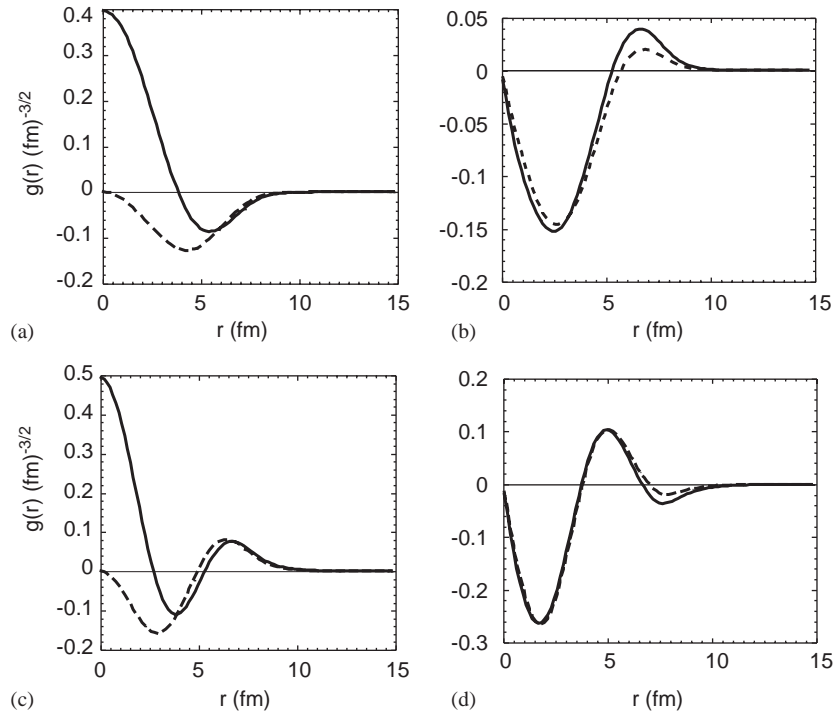


Fig. 13. (a) The upper amplitude $g(r)$ for the $1s_{1/2}$ (solid line) and $0d_{3/2}$ (dashed line) eigenfunctions, (b) the differential equation on the right-hand side (RHS) of Eq. (66) with $\tilde{\ell}=1$ for the $1s_{1/2}$ (solid line) eigenfunction and the differential equation on the left-hand side (LHS) of Eq. (66) with $\tilde{\ell}=1$ for the $0d_{3/2}$ (dashed line) eigenfunction, (c) the upper amplitude $g(r)$ for the $2s_{1/2}$ (solid line) and $1d_{3/2}$ (dashed line) eigenfunctions, and (d) the differential equation on the RHS of Eq. (66) with $\tilde{\ell}=1$ for the $2s_{1/2}$ eigenfunction (solid line) and the differential equation on the LHS of Eq. (66) with $\tilde{\ell}=1$ for the $1d_{1/2}$ (dashed line) eigenfunctions.

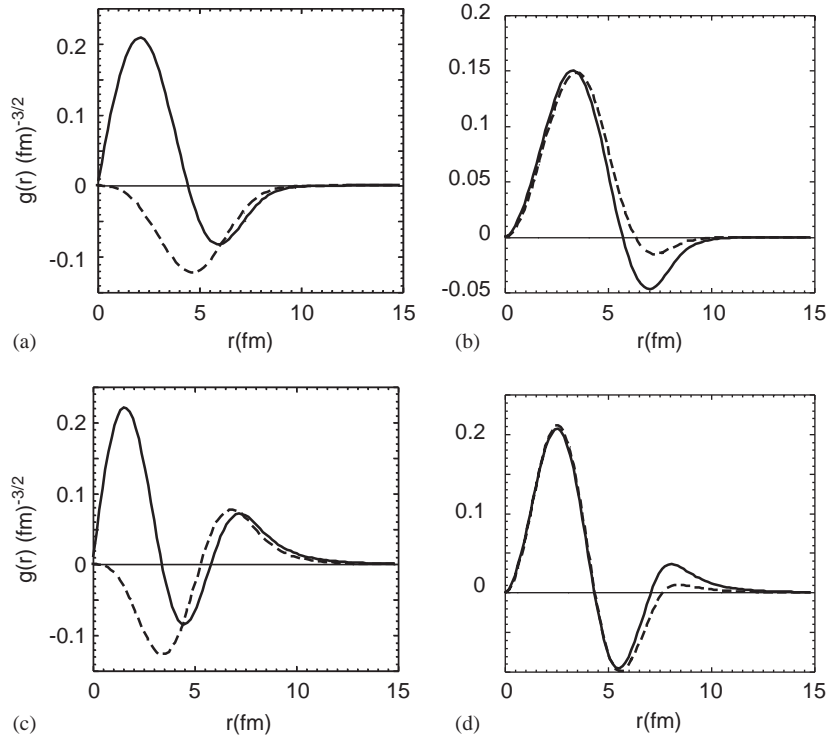


Fig. 14. (a) The upper amplitude $g(r)$ for the $1p_{3/2}$ (solid line) and $0f_{5/2}$ (dashed line) eigenfunctions, (b) the differential equation on the right-hand side (RHS) of Eq. (66) with $\tilde{\ell} = 2$ for the $1p_{3/2}$ (solid line) eigenfunction and the differential equation on the left-hand side (LHS) of Eq. (66) with $\tilde{\ell} = 1$ for the $0f_{5/2}$ (dashed line) eigenfunction, (c) the upper amplitude $g(r)$ for the $2p_{3/2}$ (solid line) and $1f_{5/2}$ (dashed line) eigenfunctions, and (d) the differential equation on the RHS of Eq. (66) with $\tilde{\ell} = 2$ for the $2p_{3/2}$ eigenfunction (solid line) and the differential equation on the LHS of Eq. (66) with $\tilde{\ell} = 2$ for the $1f_{5/2}$ (dashed line) eigenfunctions.

angular momentum, the same pattern followed by the binding energies and the lower amplitudes of the eigenfunctions [81] as seen in the last subsection.

7.1.3. Non-relativistic mean field eigenfunctions

In the limit of small lower components, the upper components are the non-relativistic approximation to the eigenfunctions. The differential relations in Eq. (66) have been tested as well for the non-relativistic eigenfunctions of the harmonic oscillator (HO) and self-consistent Hartree–Fock mean field (HF) [86]. In Fig. 17 these non-relativistic eigenfunctions are shown also to satisfy approximately the differential relations in Eq. (66) which is consistent with the fact that these models reproduce the single-nucleon spectrum well. In Fig. 17a the differential equation on the RHS of Eq. (66) with $2p_{3/2}$ eigenfunction (dashed line) is compared to the differential equation on the LHS of Eq. (66) for the $1f_{5/2}$ (solid line) eigenfunctions ($\tilde{\ell} = 2$), while in Fig. 17b the differential equation on the RHS of Eq. (66) with $1d_{5/2}$ eigenfunction (dashed line) is compared to the differential equation on the LHS of Eq. (66) for the $0g_{7/2}$ (solid line) eigenfunctions ($\tilde{\ell} = 3$). Even for the harmonic oscillator the agreement is good. Of course the

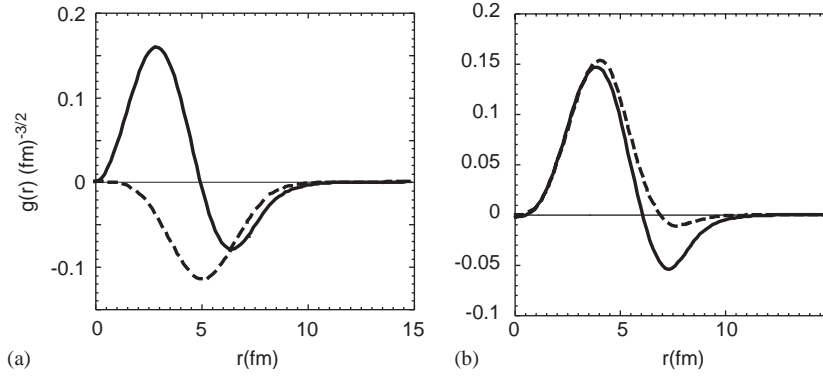


Fig. 15. (a) The upper amplitude $g(r)$ for the $1d_{5/2}$ (solid line) and $0g_{7/2}$ (dashed line) eigenfunctions, (b) the differential equation on the right-hand side (RHS) of Eq. (66) with $\tilde{\ell} = 3$ for the $1d_{5/2}$ (solid line) eigenfunction and the differential equation on the left-hand side (LHS) of Eq. (66) with $\tilde{\ell} = 3$ for the $0g_{7/2}$ (dashed line) eigenfunction.

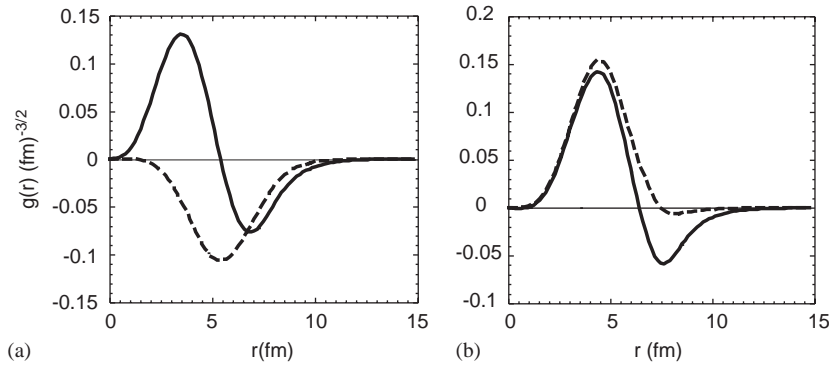


Fig. 16. (a) The upper amplitude $g(r)$ for the $1f_{7/2}$ (solid line) and $0h_{9/2}$ (dashed line) eigenfunctions, (b) the differential equation on the right-hand side (RHS) of Eq. (66) with $\tilde{\ell} = 4$ for the $1f_{7/2}$ (solid line) eigenfunction and the differential equation on the left-hand side (LHS) of Eq. (66) with $\tilde{\ell} = 4$ for the $0h_{9/2}$ (dashed line) eigenfunction.

pseudospin doublets are degenerate in energy for the harmonic oscillator. For the realistic non-relativistic Hartree–Fock eigenfunctions with proper pseudospin doublet energy splitting the agreement is even better. Hence this relativistic symmetry leaves its “smile” in the non-relativistic realistic eigenfunctions.

7.2. Pseudospin singlets and intruders

Eigenstates with $\tilde{\Lambda} = 0$ for axially symmetric deformed potentials and eigenstates with $\tilde{\ell} = 0$ for spherically symmetry potentials are pseudospin singlets and have no pseudospin partners. The non-relativistic quantum numbers for these states are $[N, n_3, \Lambda = 1]_{\frac{1}{2}}$ and $0p_{1/2}$, respectively.

However, in realistic nuclear spectra there are additional states which have no bound partners; namely the states with asymptotic quantum numbers $[N, n_3, \Lambda = N - n_3]\Lambda + \frac{1}{2}$ and spherical quantum numbers $0\ell_{j=\ell+1/2}$. For large ℓ these states are the “intruders” mentioned in Section 4. Prior to the discovery of

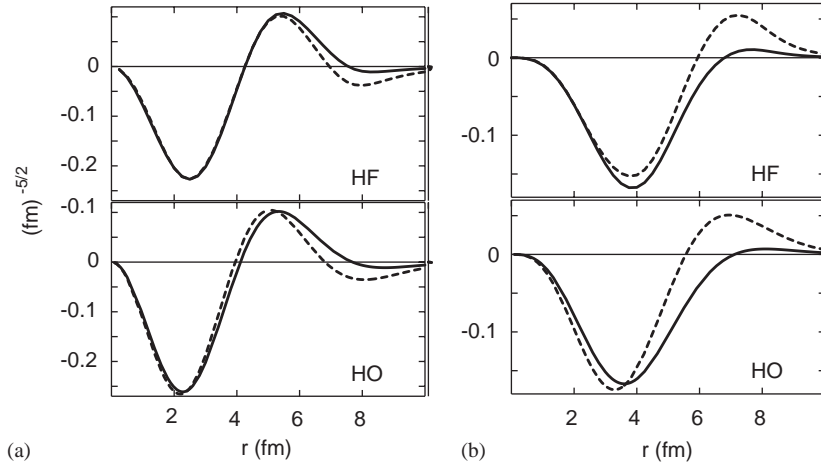


Fig. 17. (a) The differential equation on the right-hand side (RHS) of Eq. (66) for the $2p_{3/2}$ eigenfunction (dashed line) and the differential equation on the left-hand side (LHS) of Eq. (66) for the $1f_{5/2}$ eigenfunction $\tilde{\ell} = 2$ f. (b) the differential equation on the right-hand side (RHS) of Eq. (66) for the $1d_{5/2}$ eigenfunction (dashed line) and the differential equation on the left-hand side (LHS) of Eq. (66) for the $0g_{7/2}$ eigenfunction $\tilde{\ell} = 3$. HF is the non-relativistic Hartree–Fock and HO is the non-relativistic harmonic oscillator.

the relativistic origins of pseudospin symmetry these intruders were interpreted as singlets. However, now that we know the generators of the pseudospin symmetry [16], we can determine their pseudospin partners by operating on the eigenstates with the generators.

In the pseudospin limit the two states in the doublet $j = \tilde{\ell} \pm 1/2$ are degenerate, and are connected by the pseudospin generators \tilde{S}_q given in Eq. (52):

$$\tilde{S}_q \Psi_{\tilde{n}_r, \tilde{\ell}, j_i, m_i}(\vec{r}) = \sum_{j_f, m_f} A_{j_f, m_f, j_i, m_i} \Psi_{\tilde{n}_r, \tilde{\ell}, j_f, m_f} . \quad (111)$$

Here

$$A_{j_f, m_f, j_i, m_i} = (-1)^{1/2 - m_f + \tilde{\ell}} \sqrt{\frac{3(2j_i + 1)(2j_f + 1)}{2}} \begin{pmatrix} j_f & 1 & j_i \\ -m_f & q & m_i \end{pmatrix} \begin{Bmatrix} \frac{1}{2} & \tilde{\ell} & j_i \\ j_f & 1 & \frac{1}{2} \end{Bmatrix} ,$$

where the symbols are Wigner 3-j and 6-j symbols, respectively. For $\tilde{\ell} = 0$, $A_{j_f, m_f, j_i, m_i} = 0$ for $j_f \neq j_i$, which is consistent with the fact that that state is a pseudospin singlet.

In the exact pseudospin limit, $V_S(\vec{r}) = -V_V(\vec{r})$, there are no bound Dirac valence states. For nuclei to exist the pseudospin symmetry must therefore be broken. As we have seen in Section 5, realistic mean fields involve an attractive scalar potential and a repulsive vector potential of nearly equal magnitudes, $V_S(\vec{r}) \sim -V_V(\vec{r})$. Since pseudospin symmetry is broken, the pseudospin partner produced by the raising and lowering operators on an eigenstate will not necessarily be an eigenstate. The question is how different is the pseudospin partner from the eigenstate with the same quantum numbers?

For broken pseudospin Eq. (111) becomes

$$\tilde{S}_q \Psi_{\tilde{n}_r, \tilde{\ell}, j_i, m_i}(\vec{r}) = A_{j_i, m_f, j_i, m_i} \Psi_{\tilde{n}_r, \tilde{\ell}, j_i, m_f}(\vec{r}) + A_{j_f, m_f, j_i, m_i} \Psi_{\tilde{n}_r, \tilde{\ell}, j_f, m_f}^{\text{psp}}(\vec{r}) . \quad (112)$$

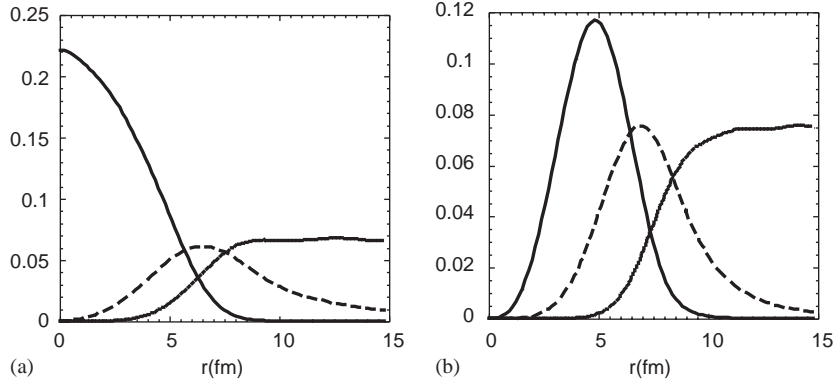


Fig. 18. (a) The upper amplitude $g(r)$ of the $0s_{1/2}$ ($\tilde{n}_r=0, \tilde{\ell}=1$) eigenfunction (solid line), the upper amplitude of its pseudospin partner $g^{\text{psp}}(r)$ (dashed line) both in $(fm)^{-3/2}$, and $r^3 g^{\text{psp}}(r)$ (dotted line), scaled to be comparable to $g^{\text{psp}}(r)$, as a function of the radial coordinate r in Fermi (fm). (b) The upper amplitude $g(r)$ of the $0f_{7/2}$ ($\tilde{n}_r=0, \tilde{\ell}=4$) eigenfunction (solid line), the upper amplitude of its pseudospin partner $g^{\text{psp}}(r)$ (dashed line) both in $(fm)^{-3/2}$, and $r^6 g^{\text{psp}}(r)$ (dotted line), scaled to be comparable to $g^{\text{psp}}(r)$, as a function of the radial coordinate r in Fermi (fm).

Here the superscript psp on the second term denotes the pseudospin partner with $j_f \neq j_i$. Even with pseudospin breaking, the pseudospin generators do not change $\tilde{\ell}$. In addition, from Eq. (112) we see that the first term with $j_f = j_i$ is exactly equal to the original eigenstate, independent of the amount of pseudospin breaking [84].

On the other hand, the upper amplitude for the pseudospin partner with $j_f = j_i + 1$ is [84]

$$g_{\tilde{n}_r, \tilde{\ell}, j_f}^{\text{psp}}(r) = g_{\tilde{n}_r, \tilde{\ell}, j_i}(r) - \frac{(2\tilde{\ell}+1)}{r^{\tilde{\ell}+2}} \int_0^r dx x^{\tilde{\ell}+1} g_{\tilde{n}_r, \tilde{\ell}, j_i}(x), \quad j_i = \tilde{\ell} - \frac{1}{2}, \quad j_f = \tilde{\ell} + \frac{1}{2}. \quad (113)$$

The amplitudes $g_{\tilde{n}_r, \tilde{\ell}, j_f}^{\text{psp}}(r)$ and $g_{\tilde{n}_r, \tilde{\ell}, j_i}(r)$ satisfy the differential conditions in Eq. (66) and therefore we have tested this relationship for the bound state doublets with $\tilde{n}_r > 0$ in the previous subsections.

Dirac bound states fall off exponentially $\sim \exp(-\sqrt{M^2 - E^2} r)$, for large r [15]. However, from Eq. (113) we see that the amplitude of the pseudospin partner, $g_{\tilde{n}_r, \tilde{\ell}, j_f}^{\text{psp}}(r)$, falls off as a power law $r^{-(\tilde{\ell}+2)}$ for large r and not exponentially. As such it has an asymptotic behavior which is very different from that of a Dirac bound state. This behavior of the pseudospin partner of the $j = \tilde{\ell} - 1/2$ Dirac eigenstates is evident in Fig. 18. In Fig. 18a the upper amplitude $g(r)$ of the $0s_{1/2}$ ($\tilde{n}_r=0, \tilde{\ell}=1$) eigenfunction (solid line) and the upper amplitude of its pseudospin partner $g^{\text{psp}}(r)$ (dashed line) are both plotted as a function of r . To make clear that the partner amplitude $g^{\text{psp}}(r)$ falls off as r^{-3} we plot $r^3 g^{\text{psp}}(r)$ (dotted line), scaled to be comparable to $g^{\text{psp}}(r)$, as well. In Fig. 18b The upper amplitude $g(r)$ of the $0f_{7/2}$ ($\tilde{n}_r=0, \tilde{\ell}=4$) eigenfunction (solid line) and the upper amplitude of its pseudospin partner $g^{\text{psp}}(r)$ (dashed line) are both plotted as a function of r . To make clear that the partner amplitude $g^{\text{psp}}(r)$ falls off as r^{-6} we plot $r^6 g^{\text{psp}}(r)$ (dotted line), scaled to be comparable to $g^{\text{psp}}(r)$, as well.

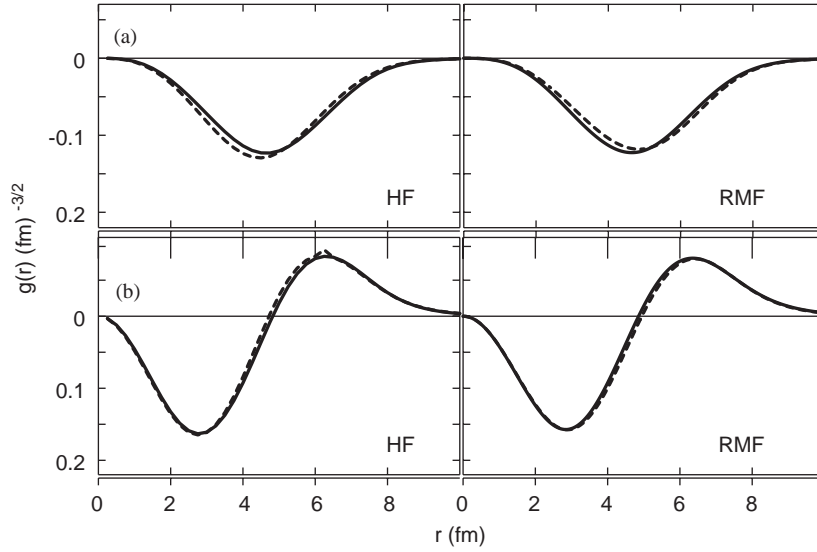


Fig. 19. The eigenfunctions for (a) $1f_{7/2}$ (solid line), $1f_{5/2}$ (dashed line) and (b) $2d_{5/2}$ (solid line), $2d_{3/2}$ (dashed line) spin partners of ^{208}Pb obtained in non-relativistic Hartree–Fock (HF) and relativistic Hartree (RMF) calculations. For RMF the upper component is plotted.

7.3. Spin and pseudospin symmetry breaking

In Fig. 19 we plot the radial eigenfunctions of the non-relativistic Hartree–Fock (HF) approximation and the upper components of the relativistic mean field (RMF) approximation for the (a) $0f$ and (b) $2d$ spin–orbit partners. The self-consistent non-relativistic and relativistic mean fields show very little difference between eigenstates of the spin doublets [86]. Thus, even though the spin–orbit splittings are large, the eigenfunctions retain spin symmetry and thus spin symmetry is an approximate dynamic symmetry.

In the non-relativistic framework, one can explain this apparent puzzle using the Nilsson model (the modified harmonic oscillator model) [22]. For the non-relativistic harmonic oscillator potential, the spin–orbit partners and the pseudospin–orbit partners are degenerate in energy. The spin–orbit eigenfunctions have the same radial eigenfunction whereas the pseudospin eigenfunctions do not exactly satisfy the pseudospin conditions as seen in Fig. 17. Hence in this limit the pseudospin is approximately broken in the eigenfunctions even though the energies are degenerate. If a spin–orbit potential such as that given in Eq. (94) is added, the spin–orbit partners are split in energy but the pseudospin partners remain degenerate. Furthermore, since this spin–orbit potential does not affect the eigenfunctions, the eigenfunctions of the spin–orbit partners will have exact spin symmetry with the radial wave functions being identical even though the partners are not degenerate in energy whereas the pseudospin partners will be degenerate in energy but the eigenfunctions will approximately violate pseudospin symmetry.

For non-relativistic and relativistic realistic potentials the spin–orbit potential is no longer constant. Therefore, the spin eigenfunctions no longer have identical spatial amplitudes and the dynamic spin symmetry is broken. Nevertheless, realistic potentials retain salient features of the Nilsson model to make spin symmetry an approximate dynamic symmetry. As seen in Fig. 8 the scalar and vector potentials are

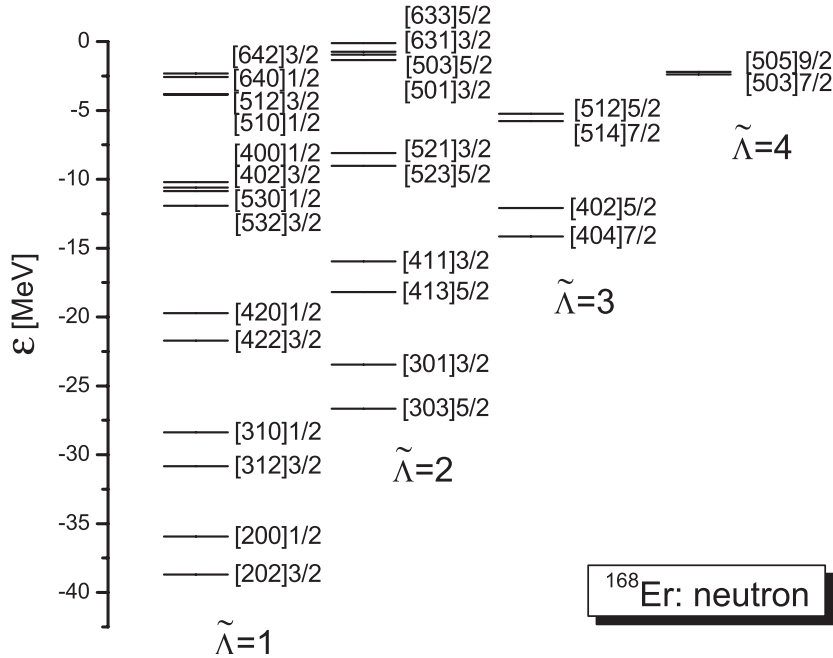


Fig. 20. The neutron single neutron spectrum in MeV for the pseudospin doublets in ^{168}Er .

relatively constant except at the nuclear surface. So most of the breaking takes place at the nuclear surface. At the nuclear surface, $d|V_V(r) - V_S(r)|/dr \gg d|V_S(r) + V_V(r)|/dr$ and thus pseudospin symmetry is favored. Hence the reason for approximate dynamic spin symmetry seems to be the shape of the potentials involved whereas the reason for pseudospin symmetry is the fact that the scalar and vector potentials are approximately equal and opposite in sign.

7.4. Test of realistic eigenfunctions for deformed nuclei with axial symmetry

The single-particle energies and eigenfunctions for axially deformed nucleus ^{168}Er are calculated by the relativistic Hartree theory in a Woods–Saxon basis [88,89]. This method has been developed from nuclear field theory in coordinate space [90–92] and has the advantage that it easily generalizes to include both deformation and pairing correlations self-consistently in the BCS approximation. These calculations lead to a theoretical average binding energy $B/A = 8.107$ MeV, a quadrupole deformation $\beta = 0.3497$ and a root mean square radius $R = 5.376$ fm, which reproduce the data well. For these realistic eigenfunctions the harmonic oscillator quantum numbers are not conserved, but the orbitals are labeled by the quantum numbers of the main spherical basis state in the expansion of the dominant upper component in the Dirac eigenfunctions.

In Fig. 20, the calculated single-neutron energies, $\varepsilon = E - M$, for the pseudospin doublets in ^{168}Er are presented. From left to right, the panels correspond to the pseudo orbital angular momentum projection $\tilde{\Lambda} = 1, 2, 3$ and 4, respectively. The energy splitting between members of pseudospin doublets decreases as the single-particle binding energy, $-\varepsilon$, decreases. For pseudospin doublets with binding

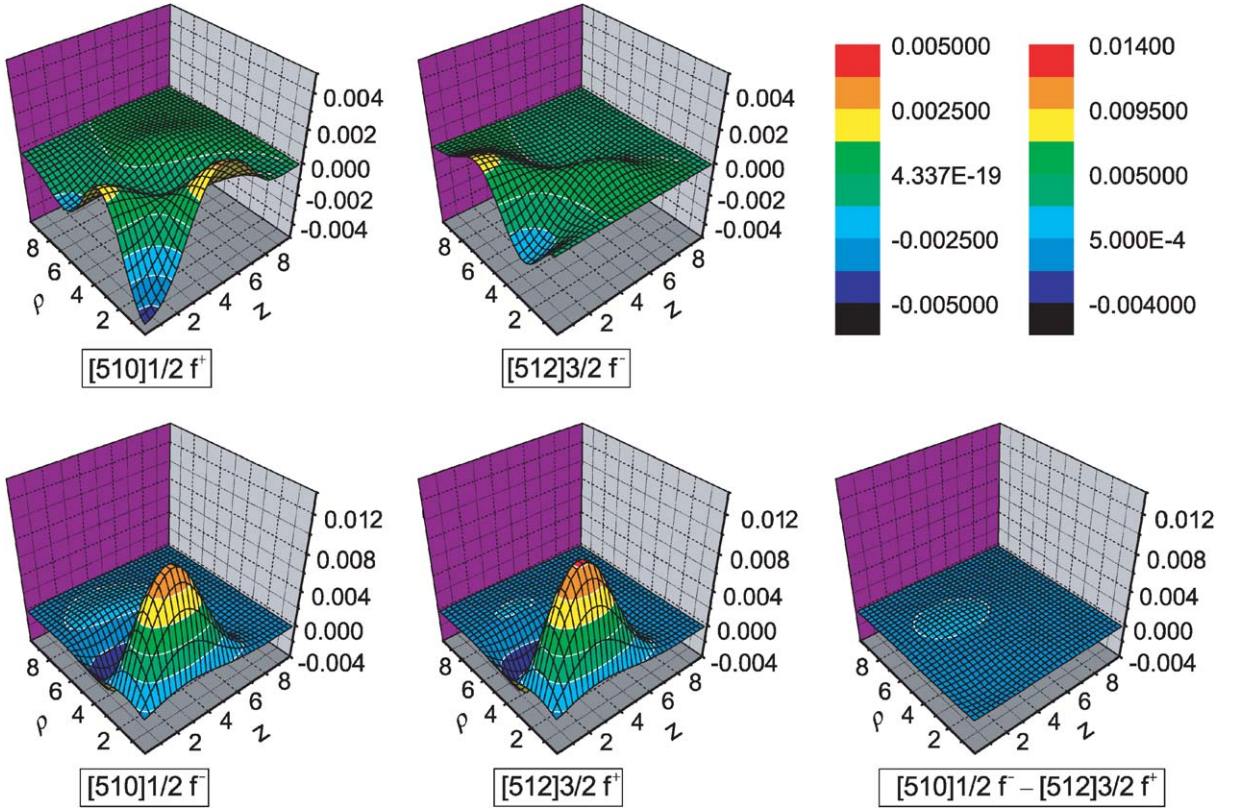


Fig. 21. Eigenfunctions in $(\text{Fermi})^{-3/2}$ as a function of z and ρ in Fermi for the neutron pseudospin doublet $[510]1/2$ and $[512]3/2$ ($\tilde{\Lambda} = 1$) in ^{168}Er . Top row: $f_{\tilde{\eta},\tilde{\Lambda},-1/2}^+$ and $f_{\tilde{\eta},\tilde{\Lambda},1/2}^-$, testing relation (53a), bottom row: $f_{\tilde{\eta},\tilde{\Lambda},-1/2}^-$ and $f_{\tilde{\eta},\tilde{\Lambda},1/2}^+$, and the difference of the two testing relation (53b). Color legends: left legend is for upper graphs; right legend for lower graphs.

energy larger than 5 MeV, the spin-up (pseudospin down) state is higher than the spin-down (pseudospin up) one. On the other hand, for the bound doublets with binding energy less than 5 MeV, the opposite is observed.

Four pairs of neutron pseudospin partners are analyzed in detail in [87]. Here we present the results of the $[510]1/2$ and $[512]3/2$ orbitals ($\tilde{\Lambda} = 1$), which have a tiny energy splitting (less than 0.01 MeV), in both three dimensional contour plots and two dimensional plots.

Three dimensional contour plots for the $[510]1/2$ and $[512]3/2$ pairs of neutron pseudospin partners are shown in Figs. 21–23 as a function of both ρ and z in a color code. Fig. 21 tests the relationships between lower component amplitudes given in Eq. (53a) (top row) and Eq. (53b) (bottom row). On the far right at the bottom row the difference between the two dominant lower amplitudes is plotted to help assess how well these amplitudes agree. In the top row of Fig. 22 the upper amplitudes which correspond to the non-relativistic quantum numbers are plotted and we see how different these amplitudes are for the two states in the doublet. The bottom row tests the relationship between upper component amplitudes given in Eq. (53c). On the far right on the bottom row the sum of the two small upper components is plotted to help assess how well these amplitudes are equal and opposite in sign. Fig. 23 tests the differential

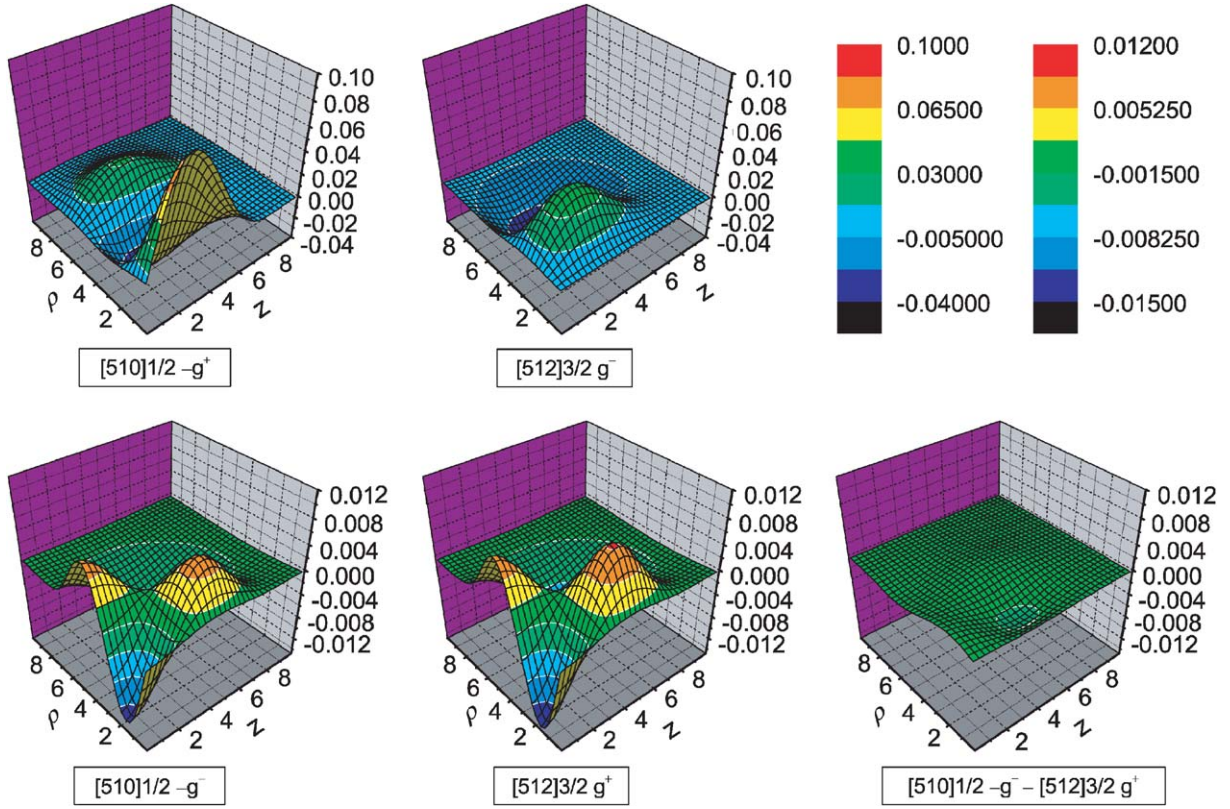


Fig. 22. Eigenfunctions in $(\text{Fermi})^{-3/2}$ as a function of z and ρ in Fermi for the neutron pseudospin doublet $[510]1/2$ and $[512]3/2$ ($\tilde{\Lambda} = 1$) in ^{168}Er . Top row: $g_{\tilde{\eta},\tilde{\Lambda},-1/2}^+$ and $-g_{\tilde{\eta},\tilde{\Lambda},1/2}^-$ (the dominant components), bottom row: $g_{\tilde{\eta},\tilde{\Lambda},-1/2}^-$ and $g_{\tilde{\eta},\tilde{\Lambda},1/2}^+$ and the sum of the two testing relation (53c). Color legends: left legend is for upper graphs; right legend for lower graphs.

relationships given in Eqs. (58). On the far right the difference of the two sides of the equations in Eqs. (58) are plotted to help assess how well these equations are satisfied. The first row tests Eq. (58a) and the second and third rows test Eq. (58b).

For another perspective on these eigenfunctions we look at sections of the amplitudes. The same pseudospin partners are shown in Figs. 24–26, as a function of z for three segments: $\rho = 1, 3, 5$ fm, and in Figs. 27–29 as a function of ρ for three segments: $z = 1, 3, 5$ fm. In each segment the top row displays the relationship between lower component amplitudes given in Eq. (53a) in the first column, the relationship between lower component amplitudes given in Eq. (53b) in the second column, and the relationship between upper component amplitudes given in Eq. (53c). The bottom row displays the differential relationship between upper component amplitudes given in Eq. (58a) in the first column and the differential relationships between upper component amplitudes given in Eq. (58b) in the second and third column.

From these figures, we can draw a number of conclusions. First, while the amplitudes $f_{\tilde{\eta},\tilde{\Lambda},-1/2}^+(\rho, z)$, $f_{\tilde{\eta},\tilde{\Lambda},1/2}^-(\rho, z)$ are not zero as predicted by Eq. (53a), they are much smaller than $f_{\tilde{\eta},\tilde{\Lambda},-1/2}^-(\rho, z)$, $f_{\tilde{\eta},\tilde{\Lambda},1/2}^+(\rho, z) \times$

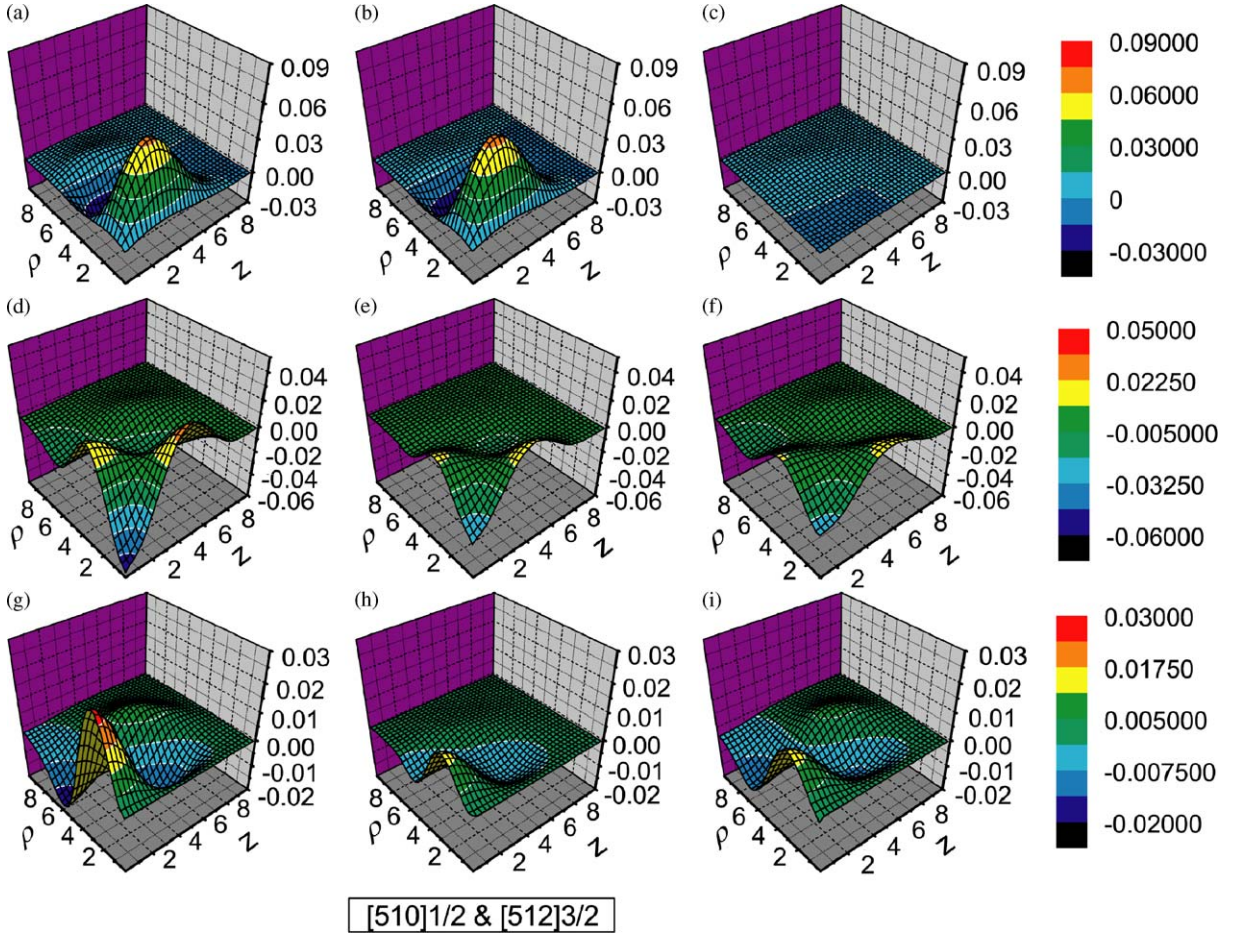


Fig. 23. Eigenfunctions in $(\text{Fermi})^{-3/2}$ as a function of z and ρ in Fermi for the neutron pseudospin doublet $[510]1/2$ and $[512]3/2$ ($\lambda = 1$) in ^{168}Er . Test of the differential relations in Eq. (58). Graphs a, b, c are respectively the left-hand side (LHS) and right-hand side (RHS) of Eq. (58a) and the difference between them. Graphs d, e and f are respectively the LHS and the RHS (with “+” sign) of Eq. (58b) and their difference. Graphs g, h and i are the LHS and RHS (with “−” sign) of Eq. (58b) and their difference.

(ρ, z) . Furthermore, $f_{\tilde{\eta}, \tilde{\lambda}, 1/2}^+(\rho, z)$ and $f_{\tilde{\eta}, \tilde{\lambda}, -1/2}^-(\rho, z)$ have similar shapes as predicted by Eq. (53b). The amplitude $-g_{\tilde{\eta}, \tilde{\lambda}, -1/2}^-(\rho, z)$ has the same shape as the amplitude $g_{\tilde{\eta}, \tilde{\lambda}, 1/2}^+(\rho, z)$, in line with the prediction of Eq. (53c), but they differ in magnitude. These amplitudes are much smaller than the other upper amplitudes, $g_{\tilde{\eta}, \tilde{\lambda}, \mp 1/2}^\pm(\rho, z)$ as suggested by Eq. (60) which is an indication of spin symmetry as discussed in Section 7.3.

The differential relation in Eq. (58a) between the dominant upper components, $g_{\tilde{\eta}, \tilde{\lambda}, 1/2}^-(\rho, z)$ and $g_{\tilde{\eta}, \tilde{\lambda}, -1/2}^+(\rho, z)$, is well obeyed in all cases. The differential relations in Eq. (58b) relate the dominant upper components, $g_{\tilde{\eta}, \tilde{\lambda}, \mp 1/2}^\pm(\rho, z)$ to the small upper components $g_{\tilde{\eta}, \tilde{\lambda}, \pm 1/2}^\pm(\rho, z)$. The shapes of the

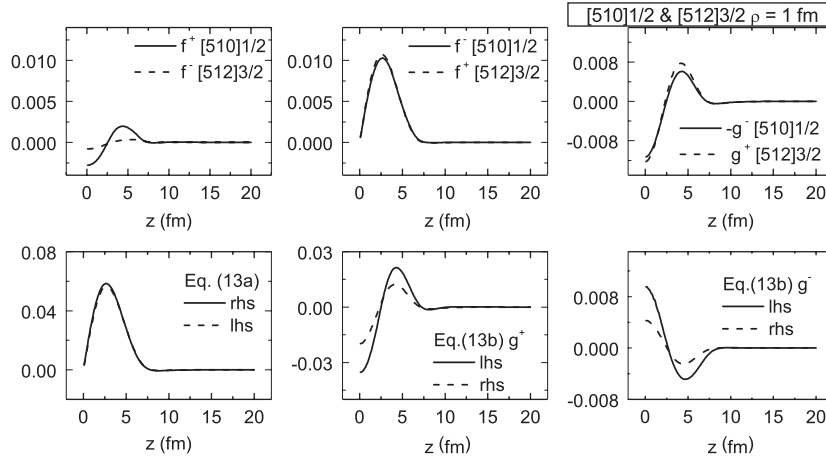


Fig. 24. Eigenfunctions in $(\text{Fermi})^{-3/2}$ as a function of z for $\rho = 1$ fm for the neutron pseudospin doublet $[510]1/2$ and $[512]3/2$ ($\tilde{A} = 1$) in ^{168}Er . In each segment, the top row shows (from left to right) the relations in (i) Eq. (53a), involving $f_{\tilde{\eta},\tilde{A},-1/2}^+$ and $f_{\tilde{\eta},\tilde{A},1/2}^-$, (ii) Eq. (53b), involving $f_{\tilde{\eta},\tilde{A},-1/2}^-$ and $f_{\tilde{\eta},\tilde{A},1/2}^+$, (iii) Eq. (53c), involving $g_{\tilde{\eta},\tilde{A},1/2}^+$ and $-g_{\tilde{\eta},\tilde{A},-1/2}^-$. The bottom row shows (from left to right) the LHS and RHS of (i) Eq. (58a), involving $g_{\tilde{\eta},\tilde{A},1/2}^-$ and $g_{\tilde{\eta},\tilde{A},-1/2}^+$, (ii) Eq. (58b), involving $g_{\tilde{\eta},\tilde{A},-1/2}^+$ and $g_{\tilde{\eta},\tilde{A},+1/2}^+$, (iii) Eq. (58b), involving $g_{\tilde{\eta},\tilde{A},+1/2}^-$ and $g_{\tilde{\eta},\tilde{A},-1/2}^-$.

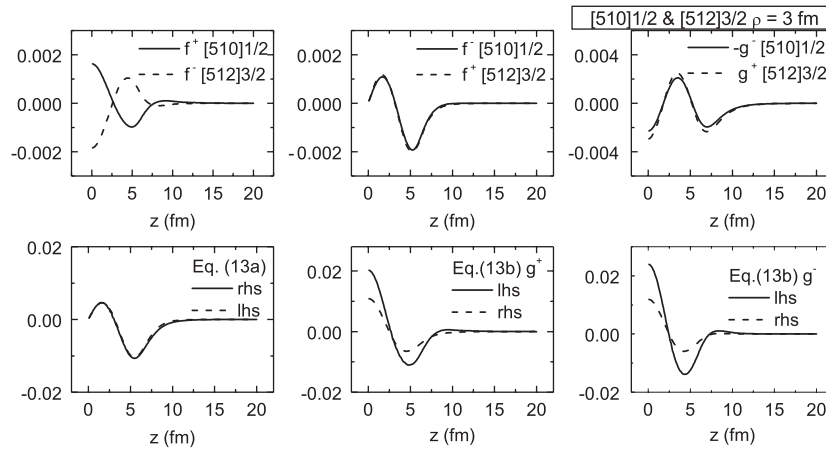


Fig. 25. Eigenfunctions in $(\text{Fermi})^{-3/2}$ as a function of z and $\rho = 3$ fm for the neutron pseudospin doublet $[510]1/2$ and $[512]3/2$ ($\tilde{A} = 1$) in ^{168}Er . The contents of the graphs are the same as Fig. 24.

left-hand side and of the right-hand side of Eq. (58b) are the same, but the corresponding amplitudes are quite different. Therefore, the differential relations in Eq. (58b) are less satisfied. These differences might partly originate from the differences in the magnitudes of the small upper components in Eq. (53c).

As in spherical nuclei, the pseudospin violation increases as the pseudo-orbital angular momentum increases and as the binding energy increases [87]. In both spherical and deformed nuclei the lower

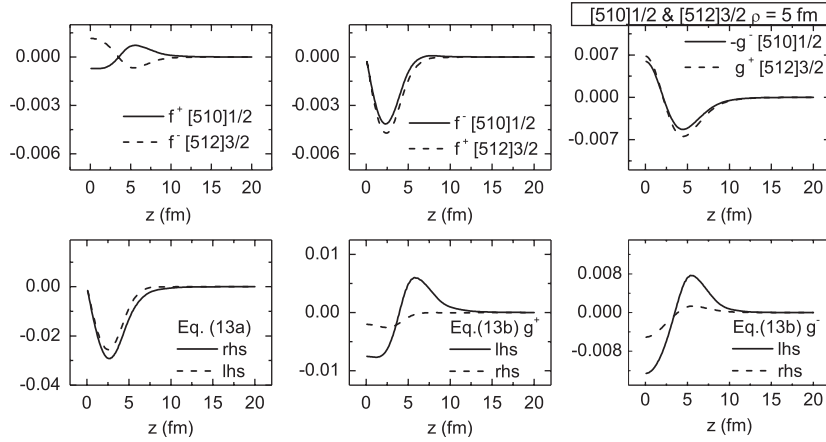


Fig. 26. Eigenfunctions in $(\text{Fermi})^{-3/2}$ as a function of z and $\rho = 5$ fm for the neutron pseudospin doublet $[510]1/2$ and $[512]3/2$ ($\tilde{A} = 1$) in ^{168}Er . The contents of the graphs are the same as Fig. 24.

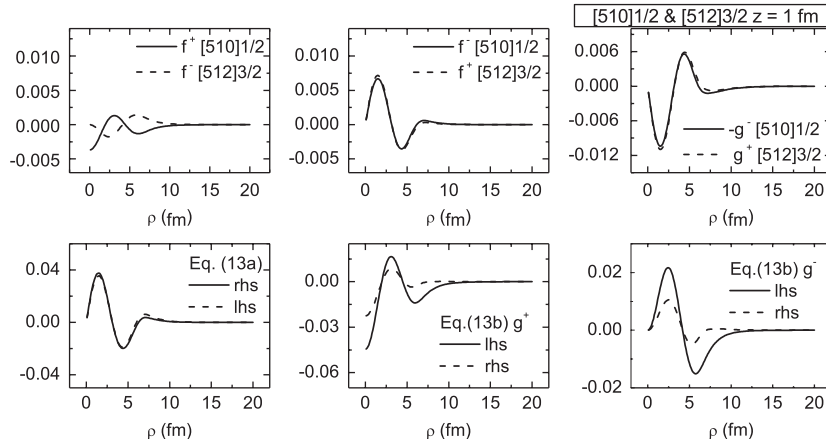


Fig. 27. Eigenfunctions in $(\text{Fermi})^{-3/2}$ as a function of ρ and $z = 1$ fm for the neutron pseudospin doublet $[510]1/2$ and $[512]3/2$ ($\tilde{A} = 1$) in ^{168}Er . The content of the graphs in each segment as in Fig. 24.

components are small compared to the upper components (Compare Figs. 9a–d, 10a–d, 11a and b, 12a and b, and Fig. 21 with the top row of Fig. 22) which is consistent with the fact that nuclei are primarily non-relativistic quantum systems. However relativistic quantum mechanics is necessary for the understanding of pseudospin symmetry.

7.5. Summary

We have reviewed the conditions that pseudospin symmetry places on the Dirac eigenfunctions. We have shown that the conditions on the lower amplitudes, Eqs. (53a)–(53b), are approximately satisfied for axially deformed nuclei and spherical nuclei. The differential relation between the dominant upper

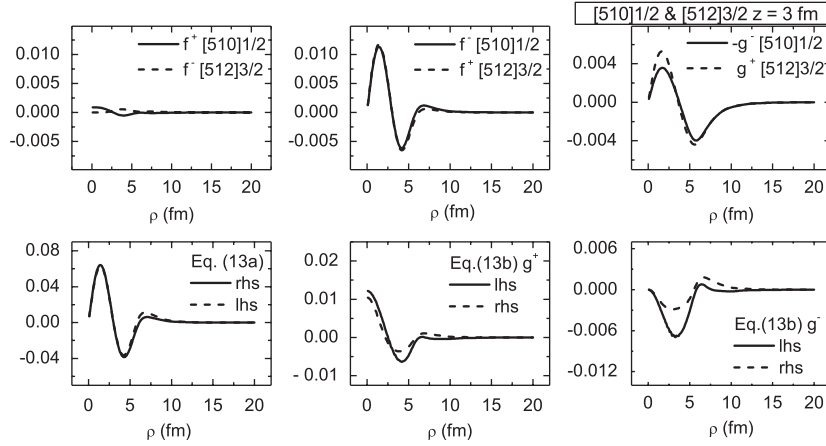


Fig. 28. Eigenfunctions in $(\text{Fermi})^{-3/2}$ as a function of ρ and $z = 3$ fm for the neutron pseudospin doublet $[510]1/2$ and $[512]3/2$ ($\tilde{A} = 1$) in ^{168}Er . The content of the graphs in each segment as in Fig. 24.

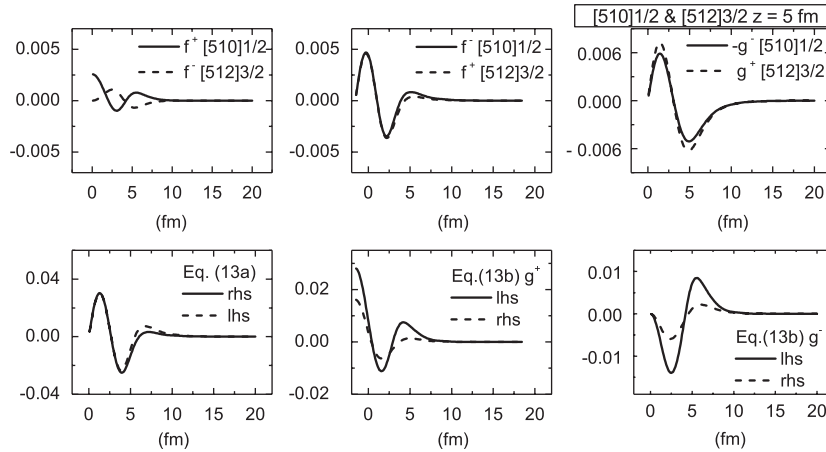


Fig. 29. Eigenfunctions in $(\text{Fermi})^{-3/2}$ as a function of ρ and $z = 5$ fm for the neutron pseudospin doublet $[510]1/2$ and $[512]3/2$ ($\tilde{A} = 1$) in ^{168}Er . The content of the graphs in each segment as in Fig. 24.

component amplitudes for axially deformed nuclei, Eq. (58a), and for spherical nuclei, Eq. (66), are also approximately satisfied. However, for axially deformed nuclei, both the relation between the amplitudes of the small upper components, Eq. (53c), and the differential equations, Eq. (58b), that relate the dominant upper components with the small upper components are not well satisfied. The pseudospin symmetry improves as the binding energy and pseudo-orbital angular momentum projection decrease, for both axially deformed nuclei and spherical nuclei.

8. Magnetic dipole and Gamow–Teller transitions

Horton, an elephant in a Dr. Seuss story, is frolicking in the jungle one day picking flowers and, because of his big ears, is able to hear a cry for help from a microscopic Who living in Whoville, which is perched on a small flower (Fig. 30). Horton vows to help the tiny Whos declaring “A person is a person no matter how small.” [93]. Likewise an amplitude is an amplitude no matter how small.

Since the lower component of the Dirac wavefunction is small [6,81,25,82], the effect of pseudospin symmetry on the relativistic wavefunction is difficult to tested empirically except perhaps in certain forbidden transitions, which, like Horton’s ears, amplify the effects of the small amplitudes. For example, single-nucleon magnetic dipole and Gamow–Teller transitions between pseudospin doublets are forbidden non-relativistically (i.e., “ ℓ forbidden” [94–96]) because the orbital angular momenta of the two states differ by two units. However, they are not forbidden relativistically. We shall use pseudospin symmetry in the wavefunction to derive relations between single-nucleon relativistic magnetic moments and magnetic dipole transitions within a pseudospin doublet on the one hand, and between single-nucleon relativistic Gamow–Teller transitions within a pseudospin doublet on the other hand. These relationships provide a test for the influence of pseudospin symmetry on the single-nucleon wavefunctions.

8.1. Magnetic moments and $M1$ transitions

The relativistic magnetic dipole operator for a particle with charge e is given by [97,98],

$$\hat{\mu}_i = -\frac{e}{2}g_\rho(\vec{\alpha} \times \vec{r})_i + \mu_{A,\rho}\Sigma_i, \quad (114)$$

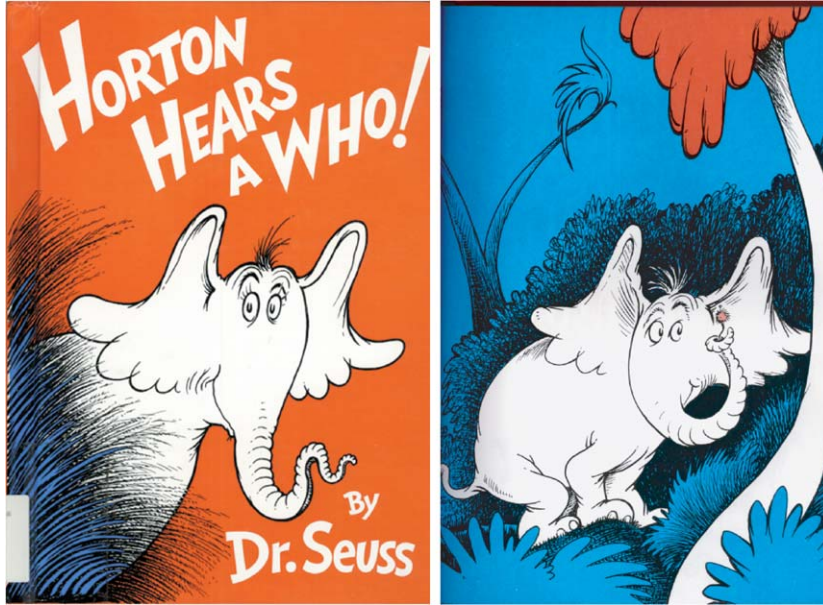


Fig. 30. Horton finds a flower on which the microscopic village of Whoville is located [93].

where $\vec{\alpha}$ is the usual Dirac matrix, \vec{r} is the three space vector, $\rho = \pi$ for a proton and ν for a neutron, g_ρ is the orbital gyromagnetic ratio, $g_\pi = 1$, $g_\nu = 0$, and $\mu_{A,\rho}$ is the anomalous magnetic moment, $\mu_{A,\pi} = 1.793\mu_0$, $\mu_{A,\nu} = -1.913\mu_0$, where $\mu_0 = e\hbar/2Mc$ is the nuclear magneton. The magnetic moment is given in terms of the matrix element of this operator with $m = j$,

$$\mu_{j,\rho} = \langle \Psi_{\tilde{n}_r, \tilde{\ell}, j, m=j, \rho} | \hat{\mu} | \Psi_{\tilde{n}_r, \tilde{\ell}, j, m=j, \rho} \rangle, \quad (115)$$

and the square root of the magnetic transition probability between two states in the doublet is given in terms of the reduced matrix element of this operator,

$$\sqrt{B(M1 : \tilde{n}_r, \tilde{\ell}, j' \rightarrow \tilde{n}_r, \tilde{\ell}, j)_\rho} = \sqrt{\frac{1}{(2j' + 1)}} \langle \Psi_{\tilde{n}_r, \tilde{\ell}, j', \rho} || \hat{\mu} || \Psi_{\tilde{n}_r, \tilde{\ell}, j, \rho} \rangle. \quad (116)$$

8.2. Non-relativistic limit

The non-relativistic limit is valid when $V_V(\vec{r}) + V_S(\vec{r})/2Mc^2$ is small, although in the interior of the nucleus this ratio is $\approx .48$. As shown in [99], the magnetic moments in the non-relativistic limit become,

$$\mu_{j,\rho}^{\text{NR}} = (j + \frac{1}{2})g_\rho\mu_0 + \mu_{A,\rho}; \quad j = \tilde{\ell} - \frac{1}{2}, \quad (117)$$

$$\mu_{j,\rho}^{\text{NR}} = \frac{j}{(j+1)} \left(\left(j + \frac{1}{2} \right) g_\rho\mu_0 - \mu_{A,\rho} \right); \quad j = \tilde{\ell} + \frac{1}{2}. \quad (118)$$

These non-relativistic limits for the magnetic moments in Eqs. (117)–(118) are equivalent to the Schmidt values [100].

For the $M1$ transition

$$B(M1 : \tilde{n}_r, \tilde{\ell}, j' \rightarrow \tilde{n}_r, \tilde{\ell}, j)_\rho^{\text{NR}} = 0; \quad j' \neq j. \quad (119)$$

In the derivation [99], this transition is proportional to $\kappa + \kappa' - 1$ which is zero for the two states in the doublet since $\kappa' = \tilde{\ell} + 1$ and $\kappa = -\tilde{\ell}$ (see Eq. (92)) for the states in the doublet. Thus the non-relativistic limit of the $B(M1)$ is zero which is consistent with the fact that the transition is from ℓ to $\ell \pm 2$.

8.3. Pseudospin symmetry

Instead of looking at the non-relativistic limit, we examine the pseudospin limit which assumes that the spatial wave functions of the lower components of the doublet are equal (up to an over all sign). Using the Dirac eigenfunction in Eq. (69), we obtain for the magnetic moments [99],

$$j = \tilde{\ell} - \frac{1}{2},$$

$$\mu_{j,\rho} = -\frac{eg_\rho(j + \frac{1}{2})}{2(j+1)} \int_0^\infty g_{\tilde{n}_r, \tilde{\ell}, j, \rho} f_{\tilde{n}_r, \tilde{\ell}, \rho} r^3 dr + \mu_{A,\rho} \left(1 - \frac{(2j+1)}{(j+1)} \int_0^\infty f_{\tilde{n}_r, \tilde{\ell}, \rho}^2 r^2 dr \right), \quad (120a)$$

$$j = \tilde{\ell} + \frac{1}{2},$$

$$\mu_{j,\rho} = \frac{eg_\rho(j + \frac{1}{2})}{2(j+1)} \int_0^\infty g_{\tilde{n}_r, \tilde{\ell}, j, \rho} f_{\tilde{n}_r, \tilde{\ell}, \rho} r^3 dr - \frac{\mu_{A,\rho}}{(j+1)} \left(j - (2j+1) \int_0^\infty f_{\tilde{n}_r, \tilde{\ell}, \rho}^2 r^2 dr \right). \quad (120b)$$

The $B(M1)$ is a transition rate between two different states and so it is the square of a matrix element. Because of the overall phase ambiguity of the eigenfunctions, the sign of the matrix element between the two states is indeterminable. Hence we shall present the relationships in terms of the $B(M1)$ and not the transition matrix element. Also, in order to save space we shall use the compressed notation for the quantum numbers $q = \tilde{n}_r, \tilde{\ell}, j$ with $q' = \tilde{n}_r, \tilde{\ell}, j'$, and $j = \tilde{\ell} + \frac{1}{2}$, $j' = \tilde{\ell} + \frac{1}{2}$. We suppress the radial argument $g_{\tilde{n}_r, \tilde{\ell}, j, \rho}(r) = g_{\tilde{n}_r, \tilde{\ell}, j, \rho}$, $f_{\tilde{n}_r, \tilde{\ell}, \rho}(r) = f_{\tilde{n}_r, \tilde{\ell}, \rho}$. Then the $B(M1)$ between the two states in the doublet is given by

$$\begin{aligned} j' &= \tilde{\ell} + \frac{1}{2}, \quad j = \tilde{\ell} - \frac{1}{2}, \\ B(M1 : q' \rightarrow q)_\rho &= \frac{(2j+1)}{(2j+3)} B(M1 : q \rightarrow q')_\rho \\ &= \frac{(2j+1)}{16(j+1)} \left[\frac{eg_\rho}{2} \int_0^\infty [g_{\tilde{n}_r, \tilde{\ell}, j', \rho} + g_{\tilde{n}_r, \tilde{\ell}, j, \rho}] f_{\tilde{n}_r, \tilde{\ell}, \rho} r^3 dr \right. \\ &\quad \left. + 4\mu_{A,\rho} \int_0^\infty f_{\tilde{n}_r, \tilde{\ell}, \rho}^2 r^2 dr \right]^2. \end{aligned} \quad (121)$$

The last term in Eqs. (122)–(121), $\int_0^\infty f_{\tilde{n}_r, \tilde{\ell}, \rho}^2 r^2 dr$, is the same because of pseudospin symmetry, $f_{\tilde{n}_r, \tilde{\ell}, j, \rho} = f_{\tilde{n}_r, \tilde{\ell}, \rho}$.

For neutrons $g_v = 0$, and hence we have one unknown quantity, $\int_0^\infty f_{\tilde{n}_r, \tilde{\ell}, \rho}^2 r^2 dr$. Therefore, if we know one magnetic quantity, we can predict two others [99],

$$B(M1 : q' \rightarrow q)_v = \frac{j+1}{2j+1} [\mu_{j,v} - \mu_{A,v}]^2, \quad (122)$$

$$B(M1 : q' \rightarrow q)_v = \frac{2j+1}{j+1} \left[\frac{j+2}{2j+3} \left(\mu_{j',v} + \frac{j+1}{j+2} \mu_{A,v} \right) \right]^2. \quad (123)$$

For protons there are three unknown integrals, and so we can only derive one relationship between the three magnetic quantities [99],

$$\begin{aligned} B(M1 : q' \rightarrow q)_\pi &= \frac{1}{4(j+1)(2j+1)} \left[\frac{(j+2)(2j+1)\mu_{j',\pi} - (2j+3)(j+1)\mu_{j,\pi} + 4(j+1)^2\mu_{A,\pi}}{(2j+3)} \right]^2. \end{aligned} \quad (124)$$

This follows because the first term under the integral sign in Eq. (121) is equal to the sum of the first term under the integral sign in Eqs. (120a) and (120b). This equality is due to pseudospin symmetry, $f_{\tilde{n}_r, \tilde{\ell}, j, \rho} = f_{\tilde{n}_r, \tilde{\ell}, \rho}$.

If the magnetic moments are given by the Schmidt values as in Eqs. (117) and (118), then the magnetic transitions in Eqs. (122), (123), and (124) will be identically zero, which is consistent with the non-relativistic limit.

The relativistic mean field overestimates the isoscalar magnetic moments of nuclei [98]. However, when the response of the spectator nucleons is included, the relativistic isoscalar magnetic moments agree better with experiment [101]. The response of the spectator nucleons do not significantly affect isovector magnetic moments since the dominant mesons in the relativistic field theory are isoscalar. If we define the isoscalar and vector operators as

$$\begin{aligned}\mu_{j,S} &= \frac{1}{2}(\mu_{j,v} + \mu_{j,\pi}); & \mu_{j,V} &= \frac{1}{2}(\mu_{j,v} - \mu_{j,\pi}); & \mu_{A,S} &= \frac{1}{2}(\mu_{A,v} + \mu_{A,\pi}); \\ \mu_{A,V} &= \frac{1}{2}(\mu_{A,v} - \mu_{A,\pi}); \\ B(M1 : q' \rightarrow q)_S &= \frac{1}{2} \left[\sqrt{B(M1 : q' \rightarrow q)_v} + \sqrt{B(M1 : q' \rightarrow q)_\pi} \right]^2; \\ B(M1 : q' \rightarrow q)_V &= \frac{1}{2} \left[\sqrt{B(M1 : q' \rightarrow q)_v} - \sqrt{B(M1 : q' \rightarrow q)_\pi} \right]^2,\end{aligned}\quad (125)$$

then the relations are separated into relations among the isoscalar and isovector magnetic properties:

$$\begin{aligned}B(M1 : q' \rightarrow q)_{S/V} \\ = \frac{\left[((j+2)(2j+1)\mu_{j',S/V} - (2j+3)(j+1)\mu_{j,S/V} + 4(j+1)^2 \frac{(\mu_{A,S/V})}{4(2j+3)}) \right]^2}{(j+1)(2j+1)}.\end{aligned}\quad (126)$$

8.4. Gamow–Teller transitions

The Gamow–Teller operator is given by

$$GT = \frac{g_A}{\sqrt{2}} \Sigma \tau_{\pm}, \quad (127)$$

where g_A is the axial vector coupling constant ($= 1.2670(35)$) and τ_{\pm} are the isospin raising and lowering operator. Thus this operator is a pure isovector operator. Using the Dirac wavefunction in Eq. (69) but not assuming pseudospin symmetry yet, the transitions become

$$\begin{aligned}j &= \tilde{\ell} - \frac{1}{2}, \\ B(GT : q, \rho \rightarrow q, \bar{\rho}) &= \frac{(j+1)}{j} g_A^2 \left[1 - \frac{(2j+1)}{(j+1)} \int_0^\infty f_{\tilde{n}_r, \tilde{\ell}, j, \rho} f_{\tilde{n}_r, \tilde{\ell}, j, \bar{\rho}} r^2 dr \right]^2,\end{aligned}\quad (128)$$

$$\begin{aligned}j &= \tilde{\ell} + \frac{1}{2}, \\ B(GT : q, \rho \rightarrow q, \bar{\rho}) &= \frac{g_A^2}{j(j+1)} \left[j - (2j+1) \int_0^\infty f_{\tilde{n}_r, \tilde{\ell}, j, \rho} f_{\tilde{n}_r, \tilde{\ell}, j, \bar{\rho}} r^2 dr \right]^2,\end{aligned}\quad (129)$$

$$j' = \tilde{\ell} + \frac{1}{2}, \quad j = \tilde{\ell} - \frac{1}{2},$$

$$\begin{aligned}
B(\text{GT} : q', \rho \rightarrow q, \bar{\rho}) &= \frac{(2j+1)}{(2j+3)} B(\text{GT} : q, \bar{\rho} \rightarrow q', \rho) \\
&= \frac{(2j+1)}{j+1} g_A^2 \left[\int_0^\infty f_{\tilde{n}_r, \tilde{\ell}, j', \rho} f_{\tilde{n}_r, \tilde{\ell}, j, \bar{\rho}} r^2 dr \right]^2.
\end{aligned} \tag{130}$$

where $\bar{\rho} = \pi$ if $\rho = \nu$ and $\bar{\rho} = \nu$ if $\rho = \pi$.

We notice that

$$B(\text{GT} : q, \rho \rightarrow q, \bar{\rho}) = B(\text{GT} : q, \bar{\rho} \rightarrow q, \rho), \tag{131}$$

even if isospin symmetry is broken; that is $f_{\tilde{n}_r, \tilde{\ell}, j, \pi} \neq f_{\tilde{n}_r, \tilde{\ell}, j, \nu}$. However, in general, for $q' \neq q$,

$$B(\text{GT} : q', \rho \rightarrow q, \bar{\rho}) \neq B(\text{GT} : q', \bar{\rho} \rightarrow q, \rho). \tag{132}$$

8.5. Non-relativistic limit of the Gamow–Teller transitions

Since terms quadratic in f are ignored in the non-relativistic limit, we get the usual results,

$$B(\text{GT} : q, \rho \rightarrow q, \bar{\rho}) = \frac{(j+1)}{j} g_A^2; \quad j = \tilde{\ell} - \frac{1}{2}, \tag{133}$$

$$B(\text{GT} : q, \rho \rightarrow q, \bar{\rho}) = \frac{j}{(j+1)} g_A^2; \quad j = \tilde{\ell} + \frac{1}{2}, \tag{134}$$

$$B(\text{GT} : q', \rho \rightarrow q, \bar{\rho}) = 0; \quad j' \neq j. \tag{135}$$

8.6. Pseudospin symmetry

Using pseudospin symmetry, Eq. (69), there is only one unknown for the Gamow–Teller transitions and hence each transition is related to the other [99],

$$j' = \tilde{\ell} + \frac{1}{2}, \quad j = \tilde{\ell} - \frac{1}{2}.$$

$$B(\text{GT} : q', \rho \rightarrow q, \bar{\rho}) = \frac{j}{2j+1} \left[\sqrt{B(\text{GT} : q, \rho \rightarrow q, \bar{\rho})} - \sqrt{\frac{j+1}{j}} g_A \right]^2, \tag{136}$$

$$B(\text{GT} : q', \rho \rightarrow q, \bar{\rho}) = \frac{(j+2)(2j+1)}{(2j+3)^2} \left[B(\text{GT} : q', \rho \rightarrow q', \bar{\rho}) + \sqrt{\frac{j+1}{j+2}} g_A \right]^2, \tag{137}$$

$$\begin{aligned}
&B(\text{GT} : q, \rho \rightarrow q, \bar{\rho}) \\
&= \left[\frac{(2j+1)}{(2j+3)} \right]^2 \frac{j+2}{j} \left[B(\text{GT} : q', \rho \rightarrow q', \bar{\rho}) - \frac{2}{(2j+1)} \sqrt{\frac{j+1}{j+2}} g_A \right]^2,
\end{aligned} \tag{138}$$

$$B(\text{GT} : q', \rho \rightarrow q, \bar{\rho}) = B(\text{GT} : q', \bar{\rho} \rightarrow q, \rho). \tag{139}$$

This last relation, Eq. (139), also follows from isospin symmetry as well, but if pseudospin symmetry is conserved than the relation holds even though isospin may be violated; i.e., $f_{\tilde{n}_r, \tilde{\ell}, \pi} \neq f_{\tilde{n}_r, \tilde{\ell}, \nu}$.

Table 1

Predicted “ ℓ forbidden” magnetic dipole transition in ^{39}Ca

	$B(M1 : g, v \rightarrow g', v)$
Predicted Eq. (123)	0.0166
Predicted Eq. (143)	0.0121
EXP Ref. [102]	0.0121 (14)

8.7. An example: ^{39}K , ^{39}Ca

The nuclei $^{39}_{19}\text{K}_{20}$ and $^{39}_{20}\text{Ca}_{19}$ are mirror nuclei. The ground state and first excited state of $^{39}_{19}\text{K}_{20}$ are interpreted as a $0d_{3/2}$ and $1s_{1/2}$ proton hole, respectively, while the ground state and first excited state of $^{39}_{20}\text{Ca}_{19}$ are interpreted as a $0d_{3/2}$ and $1s_{1/2}$ neutron hole, respectively. These states are members of the $\tilde{n}_r = 1, \tilde{\ell} = 1$ pseudospin doublet. The $M1$ transitions between these two states in both of these nuclei have been measured, although they are forbidden in a non-relativistic single-nucleon model, and are indeed small [102,103]. The magnetic moments of the ground states are known. However, the magnetic moments of the excited states are not known and hence only the magnetic transition in ^{39}Ca can be tested because it is a neutron hole. Using the magnetic moment of ^{39}Ca , $\mu = 1.02168(12)\mu_0$ [21], Eq. (123) leads to a transition rate only about 37% larger than the measured transition as seen in Table 1. However, the two states in the doublet are not pure single-particle states. In the next subsection we discuss a modification of these relations which takes into account the fact that these states are not pure single particle states. The modified relations give a transition rate that agrees with the measured value to within experimental error as seen in Table 1.

In addition, the Gamow–Teller transitions from the ground state of ^{39}Ca to the ground and first excited state of ^{39}K are known, which is enough information to test Eq. (137). For this example, for which $g = \tilde{1}$, $\tilde{1}$, $j = 1/2^+$ and $g' = \tilde{1}$, $\tilde{1}$, $j = 3/2^+$, Eq. (137) becomes

$$B(\text{GT} : g', v \rightarrow g, \pi) = \frac{5}{16} \left(\sqrt{B_{\text{GT}} : g', v \rightarrow g', \pi} + \sqrt{0.6} g_A \right)^2. \quad (140)$$

In order to evaluate this Gamow–Teller transition we need to know the sign of the square root of the experimental Gamow–Teller transition rate $B(\text{GT} : g', v \rightarrow g', \pi)$. The square root of this transition rate and the magnetic moment of the ground state of ^{39}Ca both are proportional to the spin operator as seen from Eqs. (115) and (127). The matrix element of the isospin operator is positive. As seen above the magnetic moment is positive, but the anomalous magnetic moment for the neutron is negative. Therefore the matrix element of the spin operator is negative and hence we take the sign to be negative.

Using the measured transition rate $\sqrt{B(\text{GT} : g', v \rightarrow g', \pi)} = -0.647(10)$ in Eq. (140), we see from Table 2 that the predicted Gamow–Teller transition is about 61 times the experimental value. However, since we are dealing with a single-nucleon model, we can expect renormalization of the axial coupling constant g_A due to omitted shell model configurations just as in the non-relativistic shell model [104–106]. Using two examples of the non-relativistic renormalization of the axial coupling constant for ℓ allowed transitions the predicted transition is reduced to 4.9–1.7 greater than the measured value as shown in Table 2. Because the Gamow–Teller transition in Eq. (137) is quadratic in g_A , fitting the experimental value of the magnetic dipole transition produces two values of the effective axial coupling constant \tilde{g}_A which

Table 2

Predicted “ ℓ forbidden” Gamow–Teller strength, $^{39}\text{Ca} \rightarrow ^{39}\text{K}$, for various values of the effective axial coupling constant

\tilde{g}_A	$B(\text{GT} : g', \nu \rightarrow g, \pi)$
g_A (free)	0.0349 (1)
0.76 (3) g_A Ref. [104]	0.0028 (9)
0.72 (2) g_A Ref. [107]	0.0010 (3)
0.70 g_A (fit)	0.00058 (2)
0.62 g_A (fit)	0.00058 (2)
EXP Ref. [103]	0.00058 (2)

Table 3

Predicted “ ℓ allowed” Gamow–Teller strength, $^{39}\text{Ca} \rightarrow ^{39}\text{K}$, for two values of the effective axial coupling constant

\tilde{g}_A	$B(\text{GT} : g, \nu \rightarrow g, \pi)$
g_A (free)	3.31 (1)
0.70 g_A	2.22 (1)

we show in Table 2. We see that the renormalization of g_A necessary to reproduce the experimental “ ℓ forbidden” Gamow–Teller transition is consistent with the renormalization needed in the non-relativistic shell model to reproduce ℓ allowed Gamow–Teller transitions.

Since the transition operator is proportional to the spin (Eq. (127)), in the non-relativistic shell model the transition vanishes (Eq. (135)). An effective tensor term $g_{\text{eff}}[Y_2\sigma]^{(1)}$ is added to the Gamow–Teller operator to produce a transition. Using a calculated effective coupling constant g_{eff} which includes core polarization, isobar excitations, meson exchange currents, and relativistic corrections, a value of the “ ℓ forbidden” transition $B(\text{GT} : g', \nu \rightarrow g, \pi)_{NR} = 0.0013(9)$ is calculated. This value agrees with the experimental value within the limits of experimental and theoretical uncertainty. However, the isoscalar and isovector magnetic dipole transitions calculated between the same states and using the same model underestimates the experimental transitions by a factor of an order of magnitude [103]. This inconsistency has been a puzzle for the non-relativistic shell model. On the other hand, as we just have seen, the relativistic single-nucleon model gives a consistent description of both of these transitions.

We can now predict the “ ℓ ” allowed $1/2^+ \rightarrow 1/2^+$ transition using Eq. (138). The results are tabulated in Table 3; this transition is the largest within the doublet. Furthermore, the final transition, which is also “ ℓ forbidden”, can be determined from Eqs. (130) and (139):

$$B(\text{GT} : g, \nu \rightarrow g', \pi) = 2B(\text{GT} : g', \nu \rightarrow g, \pi) = 0.00116(5) . \quad (141)$$

This relationship does not depend on the effective g_A but also follows from isospin symmetry as well.

8.8. Global test of the M1 pseudospin relations

Instead of studying a particular nucleus we now do a global survey of the magnetic dipole pseudospin relations [108]. Most nuclei are not close to being pure single particle states. The single particle strength is

distributed over many states by the residual interaction and only in odd-mass nuclei near closed shells can one expect to find states which carry large fractions of the total strength. Therefore, we restrict ourselves to nuclei with one or three particles (holes) with respect to a closed shell. The calculation of $B(M1)$ values from magnetic moments given in Eqs. (122)–(124) is modified to include the fractional single particle strength by correcting with spectroscopic factors from single-nucleon stripping (pick-up) reactions.

This leads to the following relations:

$$\frac{B(M1; q' \rightarrow q)_v}{S_q S_{q'}} = \frac{j+1}{2j+1} \left(\frac{\mu_{j,v}}{S_q} - \mu_{A,v} \right)^2, \quad (142)$$

$$\frac{B(M1; q' \rightarrow q)_v}{S_q S_{q'}} = \frac{2j+1}{j+1} \left(\frac{j+2}{2j+3} \right)^2 \left(\frac{\mu_{j'}}{S_{q'}} + \frac{j+1}{j+2} \mu_{A,v} \right)^2, \quad (143)$$

for neutron-odd nuclei and

$$\frac{B(M1; q' \rightarrow q)_\pi}{S_q S_{q'}} = \frac{\left[(j+2)(2j+1) \frac{\mu_{j'}}{S_{j'}} - (2j+3)(j+1) \frac{\mu_j}{S_j} + 4(j+1)^2 \mu_{A,\pi} \right]^2}{4(2j+3)^2(j+1)(2j+1)}, \quad (144)$$

for proton-odd nuclei where $S_{q,q'}$ are the spectroscopic factors.

The experimental information [109] on l -forbidden $M1$ transitions fulfilling the selection criteria described above are summarized in Table 4 for neutron-odd and in Table 5 for proton-odd cases. The spectroscopic factors $S_{j,j'}$ are taken from one-nucleon transfer reactions populating the respective states. For transitions between neutron-odd states one has in principle two independent predictions from Eqs. (142) and (143). However, there is only one case (^{57}Fe) where experimental information on the magnetic moments of both pseudospin partners is available. Because of the need to know the magnetic moments of both levels, the data are much more limited for proton-odd transitions. The second-last columns of the Tables 4 and 5 present the predictions of Eqs. (142)–(144). Note that generally $B(M1) \downarrow$ values are given for the experiments. Thus, if the state with $j' = \ell + \frac{1}{2}$ is lower, the prediction in Eq. (123) have to be corrected by a statistical factor $(\tilde{l} + 1)/\tilde{l}$ where appropriate.

8.9. Discussion

A comparison of the experimental l -forbidden strengths with the pseudospin predictions is displayed in Fig. 31 for neutron and proton transitions. Nuclei with 1 and 3 particles (holes) with respect to the shell closure are distinguished as circles and triangles, respectively. In neutron-odd nuclei (Fig. 31a) the theoretical $B(M1)_{\text{th}}$ strengths on the average agree reasonable well with experimental $B(M1)_{\text{exp}}$ strengths although a few cases scatter considerably. The predictive power is better for closed-shell ± 1 nuclei (with two marked exceptions, see below), while the pseudospin results for closed-shell ± 3 nuclei tend to be somewhat too large. For proton-odd transitions (Fig. 31b) a clear separation in two groups is observed. For three out of seven experimental results the pseudospin predictions are acceptable while the other four are about an order of magnitude above the data.

Since the pseudospin predictions are calculated from data it is necessary to evaluate the effect of the experimental uncertainties. The largest contribution clearly comes from the spectroscopic factors. It is difficult to quantify, but comparison of S values deduced from different reactions [e.g., (d, p) vs. (t, d) etc.]

Table 4

Experimental information on the magnetic properties of pseudospin partners and pseudospin symmetry predictions for neutron-odd nuclei

Nucl.	\tilde{l}	Conf.	E^* (MeV)	S	μ (μ_N)	Conf.	E^* (MeV)	S	μ (μ_N)	$B(M1)_{\text{exp}}$ (μ_N^2)	$B(M1)_{\text{th}}$ (μ_N^2)
$^{37}_{18}\text{Ar}_{19}$	1	$2s_{1/2}$	1.409	0.44		$1d_{3/2}$	0.000	0.88	+1.15 (1)	0.0139 (28) ^a	0.0048
$^{39}_{20}\text{Ca}_{19}$	1	$2s_{1/2}$	2.469	0.93		$1d_{3/2}$	0.000	0.99	+1.02 (0)	0.0121 (14)	0.0121
$^{53}_{24}\text{Cr}_{29}$	2	$2p_{3/2}$	0.000	0.56	−0.48(0)	$1f_{5/2}$	1.006	0.25		0.0930 (69)	0.0992
$^{57}_{28}\text{Ni}_{29}$	2	$2p_{3/2}$	0.000	0.90 ^b	−0.80(0)	$1f_{5/2}$	0.769	0.90 ^b		0.0259 (20)	0.430
$^{57}_{26}\text{Fe}_{31}$	2	$2p_{3/2}$	0.014	0.42		$1f_{5/2}$	0.137	0.59	+0.94 (1)	0.0021 (1)	0.0066
$^{59}_{28}\text{Ni}_{31}$	2	$2p_{3/2}$	0.000	0.82		$1f_{5/2}$	0.339	0.68	+0.43 (19)	0.0149 (14)	0.1600
$^{91}_{40}\text{Zr}_{51}$	3	$2d_{5/2}$	0.000	0.75	−1.30(0)	$1g_{7/2}$	2.201	0.44		0.0090 (35)	0.0059
$^{95}_{42}\text{Mo}_{53}$	3	$2d_{5/2}$	0.000	0.59	−0.91(0)	$1g_{7/2}$	0.762	0.18		0.0199 (36)	0.0083
$^{97}_{44}\text{Ru}_{53}$	3	$2d_{5/2}$	0.000	0.57	−0.79(1)	$1g_{7/2}$	0.421	0.61		0.0149 (7) ^c	0.0581
$^{139}_{58}\text{Ce}_{81}$	1	$3s_{1/2}$	0.255	0.90		$2d_{3/2}$	0.000	0.85	0.96(4)	0.0061 (20)	0.0002
$^{141}_{60}\text{Nd}_{81}$	1	$3s_{1/2}$	0.193	0.95		$2d_{3/2}$	0.000	1.00	1.01(1)	0.0038 (4)	0.0180
$^{145}_{60}\text{Nd}_{85}$	4	$2f_{7/2}$	0.000	0.52	−0.66(0)	$1h_{9/2}$	0.748	0.22		0.0048 (20) ^c	0.0269
$^{207}_{82}\text{Pb}_{125}$	2	$3p_{3/2}$	0.898	0.95		$2f_{5/2}$	0.570	0.80	+0.80 (3)	0.053 (7)	0.0829
$^{209}_{82}\text{Pb}_{127}$	5	$2g_{9/2}$	0.000	0.83	−1.47(0)	$1i_{11/2}$	0.779	0.86		0.0100 (7) ^c	0.0073

Given are the pseudo-orbital angular momentum \tilde{l} , the single particle states, their excitation energies E^* , spectroscopic factors S , and magnetic moments μ , and the $B(M1)_{\text{exp}}$ \downarrow transition strength between them. All experimental results are from [109] except where noted. The last column presents the pseudospin symmetry prediction for the $B(M1)_{\text{th}}$ \downarrow strengths.

^a $E2$ contribution estimated from shell model [110].

^b From shell model [111].

^c Pure $M1$ transition assumed.

and typical errors of the measured cross sections suggest a range of $\pm 20\%$. Agreement can be achieved for all neutron transitions within the estimated uncertainty for the spectroscopic factors indicated, with two exceptions. For the proton transitions most of the transitions fall outside the experimental error of the spectroscopic factors [108].

As pointed out above, Eqs. (142) and (143) can provide independent results for the same transition. For the data selected here, there is only one case (^{57}Fe) where experimental data on magnetic moments of both states are available. Besides the result given in Table 4, a value $\mu = -0.15\mu_N$ has been measured for the $E^* = 0.014$ MeV, $J^\pi = 3/2^-$ state [109]. The prediction of Eq. (142) would be $B(M1) = 0.0924\mu_N^2$ in poor agreement with experiment. The spectroscopic information for this level suggests a more complex structure beyond the single particle picture. This is also reflected in shell-model calculations [112,113] which provide a successful description of the $M1$ transitions strengths in ^{57}Fe . While these calculations can account for the magnetic moments of $1/2^-$ g.s. and the lowest $5/2^-$ state used in Table 4, they completely fail for the $3/2^-$ state.

Table 5

Same as Table 4, but for proton-odd nuclei

Nucl.	\tilde{l}	Conf.	E^* (MeV)	S	μ (μ_N)	Conf.	E^* (MeV)	S	μ (μ_N)	$B(M1)_{\text{exp}}$ (μ_N^2)	$B(M1)_{\text{th}}$ (μ_N^2)
$^{67}_{31}\text{Ga}_{36}$	2	$2p_{3/2}$	0.000	0.36	+1.85 (0)	$1f_{5/2}$	0.359	0.79	1.40 (65)	0.0169 (13)	0.011
$^{121}_{51}\text{Sb}_{70}$	3	$3d_{5/2}$	0.000	0.92	+3.36 (0)	$2g_{7/2}$	0.058	0.75 ^a	+2.52 (1)	0.0180 (8)	0.740
$^{127}_{53}\text{I}_{74}$	3	$3d_{5/2}$	0.000	0.60 ^b	+2.81 (0)	$2g_{7/2}$	0.058	0.70 ^b	+2.54 (1)	0.0219 (15)	0.230
$^{129}_{53}\text{I}_{76}$	3	$3d_{5/2}$	0.028	0.59	+2.80 (0)	$2g_{7/2}$	0.000	0.66	+2.62 (3)	0.0180 (13)	0.370
$^{131}_{53}\text{I}_{78}$	3	$3d_{5/2}$	0.150	0.53	+2.79 (50)	$2g_{7/2}$	0.000	0.64	+2.74 (1)	0.010 (1)	0.314
$^{203}_{81}\text{Tl}_{122}$	1	$3s_{1/2}$	0.000	0.70	+1.62 (0)	$2d_{3/2}$	0.279	0.46	−0.02 (17)	0.0021 (1)	0.0071
$^{205}_{81}\text{Tl}_{122}$	1	$3s_{1/2}$	0.000	0.70	+1.64 (0)	$2d_{3/2}$	0.204	0.42	−0.08 (5)	0.00078 (4)	0.0019

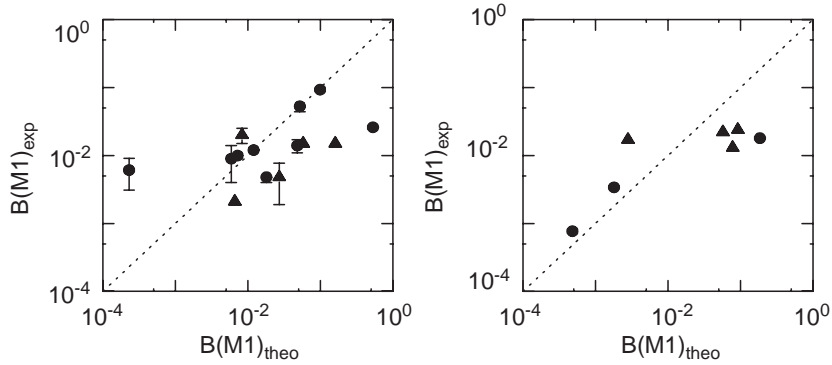
^aEstimated from systematics in Sb isotopes.^bEstimated from systematics in I isotopes.

Fig. 31. Experimental l -forbidden $M1$ transition strengths in (a) neutron-odd nuclei and (b) proton-odd nuclei vs. pseudospin symmetry predictions, Eqs. (142), (143). Circles correspond to 1 particle (hole), triangles to 3 particles (holes) with respect to closed shells.

8.10. Summary

The relativistic $SU(2)$ pseudospin symmetry has been tested through experimental magnetic properties of the pseudospin doublets of single particle states in near-closed shell nuclei. After correction for the fragmentation of the single particle strength in the wave functions, predictions connecting the l -forbidden $M1$ transitions between pseudospin partners with their magnetic moments agree reasonable with the data throughout the nuclear landscape. Considering the simplicity of the approach neglecting any explicit account for the well-established quenching of magnetic moments with respect to the Schmidt values, this success seems remarkable. However, pronounced deviations occur at the $N = 28$ and $Z = 50$ shell closures the origin of which is at present not clear.

In the non-relativistic shell model, particular interest has focused on l -forbidden GT and $M1$ transitions in doubly magic plus one particle (hole) nuclei as a test of tensor corrections to the respective one-body

operators. Microscopic predictions [114–116] account for the former, but fail for the latter. For the two cases where data are sufficient for a description in pseudospin symmetry we find perfect agreement for one (^{39}Ca) and disagreement for the other (^{57}Ni). However, the mass-57 system needs further investigation because of the unexpected softness of the ^{56}Ni closed core. Clearly, a measurement of the magnetic moments of the $2s_{1/2}^{-1}$ excited levels in ^{39}K and ^{39}Ca and the $1f_{5/2}$ levels in ^{57}Ni and ^{57}Cu would be of considerable interest to test the predictive power of the approach.

9. Quadrupole transitions in the pseudospin limit

Transitions that are not “ ℓ -forbidden” are dominated by the upper components. The upper components of the pseudospin generators in Eq. (52) are the spin generators transformed by the unitary operator U_p . Likewise the i th single particle electromagnetic multipole operators of rank ℓ , $Q^{(\ell)}_m = r^{\ell}_i Y^{(\ell)}(\theta_i, \phi_i)$ are similarly transformed

$$\tilde{Q}^{(\ell)}_m(\vec{r}_i) = U_{p_i} Q^{(\ell)}_m(\vec{r}_i) U_{p_i} . \quad (145)$$

For A nucleons,

$$\sum_{i=1}^A \tilde{Q}^{(\ell)}_m(\vec{r}_i) = \sum_{i=1}^A Q^{(\ell)}_m(\vec{r}_i) + \sum_{i=1}^A [\vec{p}_i, Q^{(\ell)}_m(\vec{r}_i)] \cdot \vec{p}_i + \sum_{i=1}^A [\vec{p}_i, Q^{(\ell)}_m(\vec{r}_i)] \times \vec{p}_i \cdot \sigma_i . \quad (146)$$

The first two terms on the right-hand side do not depend on the spin. If we assume that the pseudospin zero state is lowest for even–even nuclei, then the contribution of the third term is zero. If we assume that the pseudospin $\frac{1}{2}$ state is lowest for odd nuclei, then the contribution of the third term is small. Ignoring the spin term then the multipole transitions between pseudospin doublets are related and the quadrupole moments are related to the multipole transitions within a doublet. For example, for quadrupole transitions, $\ell=2$, using the notation $\frac{B(E2: \tilde{L}, J \rightarrow \tilde{L}_f, J_f)}{B(E2: \tilde{L}', J' \rightarrow \tilde{L}'_f, J'_f)}$ for the ratio of transitions rates and $Q(\tilde{L}, J)$ for the quadrupole moment,

$$\frac{B(E2: \tilde{L}, \tilde{L} - \frac{1}{2} \rightarrow \tilde{L} - 1, \tilde{L} - \frac{1}{2})}{B(E2: \tilde{L}, \tilde{L} - \frac{1}{2} \rightarrow \tilde{L} - 1, \tilde{L} - \frac{3}{2})} \approx \frac{3}{(\tilde{L} + 1)(2\tilde{L} - 3)} , \quad (147a)$$

$$\frac{B(E2: \tilde{L}, \tilde{L} + \frac{1}{2} \rightarrow \tilde{L} - 1, \tilde{L} - \frac{3}{2})}{B(E2: \tilde{L}, \tilde{L} + \frac{1}{2} \rightarrow \tilde{L} - 1, \tilde{L} - \frac{1}{2})} \approx \frac{4}{(2\tilde{L} - 3)(2\tilde{L} + 3)} , \quad (147b)$$

$$\frac{B(E2: \tilde{L}, \tilde{L} - \frac{1}{2} \rightarrow \tilde{L} - 2, \tilde{L} - \frac{3}{2})}{B(E2: \tilde{L}, \tilde{L} + \frac{1}{2} \rightarrow \tilde{L} - 2, \tilde{L} - \frac{3}{2})} \approx \frac{1}{\tilde{L}(\tilde{L} - 2)} , \quad (147c)$$

$$\frac{B(E2: \tilde{L}, \tilde{L} - \frac{1}{2} \rightarrow \tilde{L} - 2, \tilde{L} - \frac{3}{2})}{B(E2: \tilde{L}, \tilde{L} - \frac{1}{2} \rightarrow \tilde{L} - 2, \tilde{L} - \frac{5}{2})} \approx \frac{4}{(2\tilde{L} + 1)(2\tilde{L} - 3)} , \quad (147d)$$

Table 6

The ratio of quadrupole transition strengths, $\frac{B(E2: \tilde{L}, J \rightarrow \tilde{L}_f, J_f)}{B(E2: \tilde{L}, J' \rightarrow \tilde{L}_f, J'_f)}$, for pseudospin symmetry (ps) and experimental values (exp) for ^{189}Os with errors in parenthesis

\tilde{L}	\tilde{L}_f	J	J_f	J'	J'_f	ps	Exp [26]
3	2	$\frac{7}{2}$	$\frac{3}{2}$	$\frac{7}{2}$	$\frac{5}{2}$	0.148	0.183 (0.073)
3	1	$\frac{5}{2}$	$\frac{3}{2}$	$\frac{7}{2}$	$\frac{3}{2}$	0.333	0.281 (0.118)
3	2	$\frac{5}{2}$	$\frac{5}{2}$	$\frac{5}{2}$	$\frac{3}{2}$	0.250	0.438 (0.280)
2	1	$\frac{3}{2}$	$\frac{3}{2}$	$\frac{3}{2}$	$\frac{1}{2}$	1.000	0.355 (0.110)

Table 7

The ratio of quadrupole transition strengths, $\frac{B(E2: \tilde{L}, J \rightarrow \tilde{L}_f, J_f)}{B(E2: \tilde{L}, J' \rightarrow \tilde{L}_f, J'_f)}$, for pseudospin symmetry (ps) and experimental values (exp) for ^{187}Os with errors in parenthesis

\tilde{L}	\tilde{L}_f	J	J_f	J'	J'_f	ps	Exp [26]
3	2	$\frac{5}{2}$	$\frac{5}{2}$	$\frac{5}{2}$	$\frac{3}{2}$	0.250	0.293 (0.077)
3	1	$\frac{5}{2}$	$\frac{3}{2}$	$\frac{5}{2}$	$\frac{1}{2}$	0.286	0.410 (0.094)

$$\frac{B(E2 : \tilde{L}, \tilde{L} - \frac{1}{2} \rightarrow \tilde{L}, \tilde{L} + \frac{1}{2})}{Q(\tilde{L}, \tilde{L} + \frac{1}{2})^2} \approx \frac{15(\tilde{L} + 1)}{\tilde{L}^2(2\tilde{L} + 1)^2(2\tilde{L} - 1)}, \quad (147e)$$

$$\frac{Q(\tilde{L}, \tilde{L} - \frac{1}{2})}{Q(\tilde{L}, \tilde{L} + \frac{1}{2})} \approx \frac{(\tilde{L} - 1)(2\tilde{L} + 3)}{\tilde{L}(2\tilde{L} + 1)}. \quad (147f)$$

We test these relations by comparing them with experimental transition rates for ^{189}Os and ^{187}Os in Tables 6 and 7, respectively. Except for the transition in the last entry in Table 6 the agreement is good.

These relations in Eqs. (147) are approximately valid to order $1/A$. If the U_r pseudospin transformation is used instead of the correct helicity transformation, the relations in Eqs. (147) become exact [117].

10. Pseudo-SU(4) symmetry

Pseudo-SU(4) symmetry is the symmetry generated by the pseudospin generators \tilde{S}_i (Eq. (52)), the isospin generators T_i , and the generators $\tilde{S}_i T_j$, $i, j = 1, 2, 3$. Shell model studies in the nickel region studied the pseudo SU(4) composition of the eigenstates and found mixed results [54]. More recent shell model studies in the same region found more reasonable conservation of this pseudo-SU(4) symmetry [55,56]. However, both of these studies used the U_r pseudospin transformation instead of the correct helicity pseudospin transformation U_p . As seen in the last section, Section 9, the U_r pseudospin transformation is valid only for large atomic mass. More research on pseudo-SU(4) symmetry is needed.

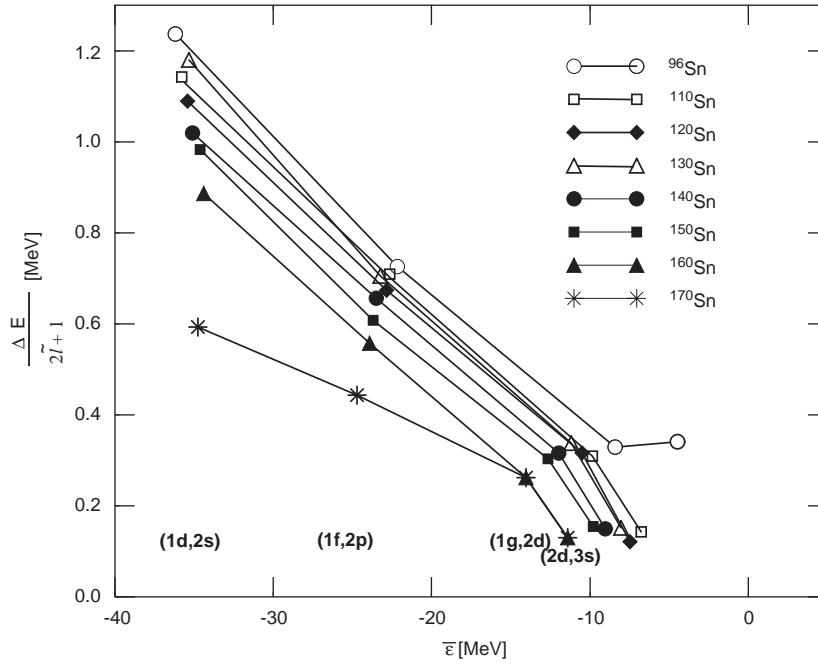


Fig. 32. The energy splitting (Eq. (93)) divided by $2\tilde{\ell} + 1$ for various tin isotopes as a function of the average single nucleon energy (Eq. (148)). From left to right the pseudospin doublets are $(1d_{3/2}, 2s_{1/2})$, $(1f_{5/2}, 2p_{3/2})$, $(1g_{7/2}, 2d_{5/2})$, $(2d_{3/2}, 3s_{1/2})$.

11. Isospin dependence of pseudospin symmetry

Rare isotope accelerators (RIA) will be exploring nuclei beyond the valley of stability and therefore it is of interest to explore the isospin dependence of pseudospin symmetry. The energy splittings (Eq. (93)) of the neutron pseudospin doublets $(1d_{3/2}, 2s_{1/2})$, $(1f_{5/2}, 2p_{3/2})$, $(1g_{7/2}, 2d_{5/2})$, and $(2d_{3/2}, 3s_{1/2})$ are plotted for the average single nucleon energy of the doublets

$$\bar{\varepsilon} = \frac{\tilde{\ell} E_{\tilde{\ell}, j=\tilde{\ell}-1/2} + (\tilde{\ell} + 1) E_{\tilde{\ell}, j=\tilde{\ell}+1/2}}{2\tilde{\ell} + 1} - M \quad (148)$$

for various isotopes of Sn (Fig. 32) and Zr (Fig. 33), from the proton drip line to the neutron drip line [118]. These energies were calculated in the relativistic mean field approximation of the nuclear field theory discussed in Section 5 which includes the exchange of the isovector vector ρ field and the exchange of the photon, which produces the Coulomb interaction, as well as the usual isoscalar σ and ω fields. Since the energy splittings are proportional to $2\tilde{\ell} + 1$ [6], they are divided by $2\tilde{\ell} + 1$ in the figures in order to remove most of the dependence on $\tilde{\ell}$. The pseudospin doublets considered are $(1d_{3/2}, 2s_{1/2})$, $(1f_{5/2}, 2p_{3/2})$, $(1g_{7/2}, 2d_{5/2})$, $(2d_{3/2}, 3s_{1/2})$.

First we note that the energy splittings decrease as the binding energy decreases consistent to what we have observed previously. However, we note as well that the energy splittings decrease as the neutron number increases except for the least bound states, which have the smallest splittings, for which there is very little variation in the splitting.

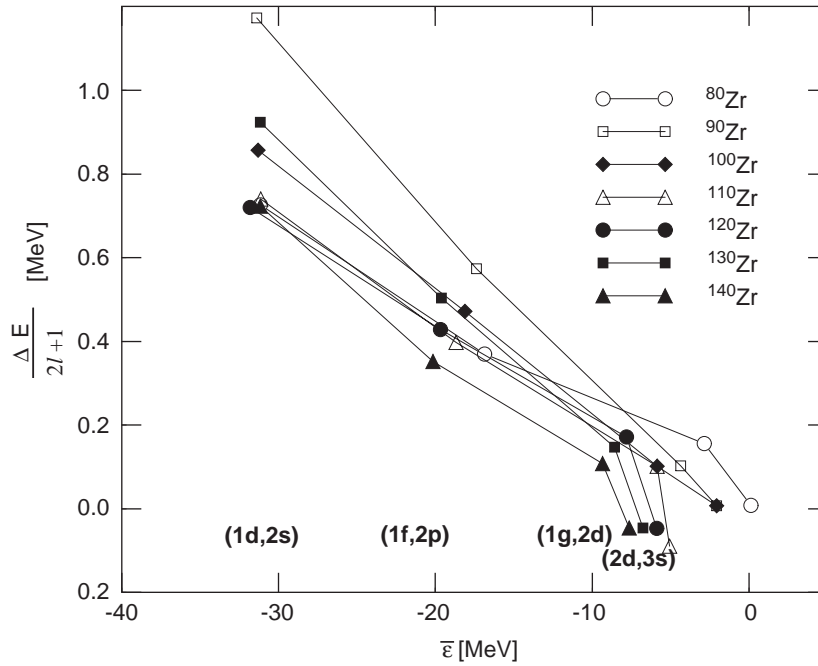


Fig. 33. The energy splitting (Eq. (93)) divided by $2\tilde{\ell} + 1$ for various zirconium isotopes as a function of the average single nucleon energy (Eq. (148)). From left to right the pseudospin doublets are $(1d_{3/2}, 2s_{1/2})$, $(1f_{5/2}, 2p_{3/2})$, $(1g_{7/2}, 2d_{5/2})$, $(2d_{3/2}, 3s_{1/2})$.

An independent calculation of the Sn isotopes with a Dirac Hamiltonian and realistic Woods–Saxon potentials including scalar, vector, isovector vector and Coulomb potentials [119–121] studies the effect of the isovector vector ρ field. In Fig. 34 the neutron energy splitting (Eq. (93)) is shown with and without the isovector vector ρ field included. Without the vector potential the energy splitting increases. On the other hand, the proton energy splittings (Eq. (93)) shown in Fig. 35 increase with the inclusion of the isovector vector ρ field. Inclusion of the Coulomb potentials also increases the proton energy splittings shown as seen in Fig. 35. Experiments at RIA facilities will determine empirically the importance of the ρ mesons or other isovector mesons in pseudospin symmetry.

12. Nucleon scattering from nuclei

For nuclear bound states the scalar and vector relativistic potentials are real. However, pseudospin symmetry exists for complex mean fields as well as long as they satisfy the condition $V_S(\vec{r}) = -V_V(\vec{r})$. Therefore, if the potentials are complex as in nucleon–nucleus scattering and they satisfy this condition, pseudospin symmetry will be valid. Indeed relativistic optical model analyses of proton scattering on nuclei is very well described by treating the nucleon as a Dirac particle moving in an complex scalar, $V_S(\vec{r})$, and vector, $V_V(\vec{r})$, optical potential with $V_S(\vec{r}) \approx -V_V(\vec{r})$ [122,123]. In a paper entitled “Sudden Death of a Symmetry” [124], the authors used the fact that the Dirac Hamiltonian has a symmetry for $V_S(\vec{r}) = -V_V(\vec{r})$ to predict the analyzing power and spin rotation function for proton scattering. Since

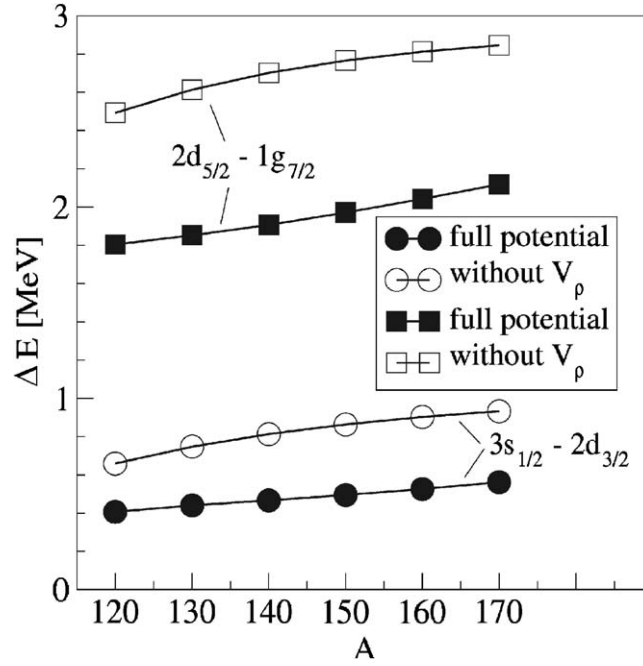


Fig. 34. The energy splitting of the neutron states (Eq. (93)) for the $(1g_{7/2}, 2d_{5/2})$, $(2d_{3/2}, 3s_{1/2})$ pseudospin doublets as a function of the atomic mass of the tin isotopes.

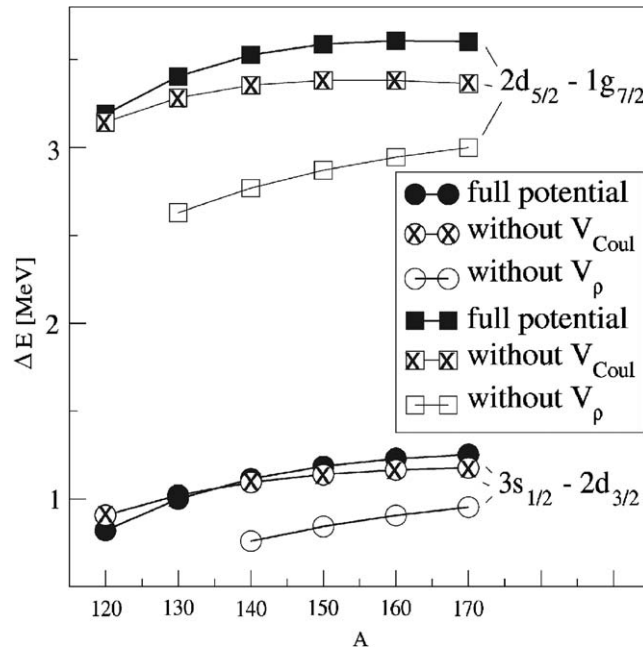


Fig. 35. The energy splitting of the proton states (Eq. (93)) for the $(1g_{7/2}, 2d_{5/2})$, $(2d_{3/2}, 3s_{1/2})$ pseudospin doublets as a function of the atomic mass of the tin isotopes.

the experimental data does not agree with this prediction, they correctly concluded that the symmetry is broken for nucleon–nucleus scattering. Furthermore, they demonstrated that the pseudospin symmetry breaking depends on the nucleon energy and may decrease as the nucleon energy is increased.

First we discuss the conventional formalism of scattering in terms of spin. We then discuss the formalism of scattering in terms of pseudospin. Finally we discuss pseudospin symmetry as a broken symmetry and extract from the experimental data an empirical estimate of the amount of pseudosymmetry breaking in medium energy nucleon–nucleus scattering.

12.1. Nucleon–nucleus scattering amplitude in the spin representation

The scattering amplitude, f , for the elastic scattering of a nucleon with momentum k on a spin zero target is given by [125]

$$f = A(k, \theta) + B(k, \theta) \vec{\sigma} \cdot \vec{n} , \quad (149)$$

where \vec{n} is the unit vector perpendicular to the scattering plane and θ is the scattering angle,

$$\vec{k}_i \cdot \vec{k}_f = k^2 \cos(\theta) , \quad (150)$$

$\hbar\vec{k}_i$ is the incident momentum, and $\hbar\vec{k}_f$ is the final momentum. The spin independent scattering amplitude, A , and the spin dependent amplitude, B , can be expanded in terms of partial waves,

$$A = \frac{-i}{2k} \sum_{\ell} [(S(k)_{\ell, \ell+1/2} - 1)(\ell + 1) + (S(k)_{\ell, \ell-1/2} - 1)\ell] P_{\ell}(\cos(\theta)) ,$$

$$B = \frac{1}{2k} \sum_{\ell} [S(k)_{\ell, \ell+1/2} - S(k)_{\ell, \ell-1/2}] P_{\ell}^{(1)}(\cos(\theta)) , \quad (151)$$

where $S(k)_{\ell, j}$ is the partial wave scattering amplitude with orbital angular momentum ℓ and total momentum j , $j = \ell \pm 1/2$, and $P_{\ell}(\cos(\theta))$ and $P_{\ell}^{(1)}(\cos(\theta))$ are the Legendre and associated Legendre polynomial of rank ℓ , respectively.

The differential cross section is given by the total absolute square of the scattering amplitude average over the spin,

$$\frac{d\sigma}{d\Omega}(k, \theta) = |A|^2 + |B|^2 . \quad (152)$$

By measuring the asymmetry in the cross section with respect to the spin, the polarization can be determined,

$$P(k, \theta) = \frac{BA^* + B^*A}{|A|^2 + |B|^2} , \quad (153)$$

and by measuring the asymmetry in the cross section with respect to the spin in a second scattering the spin rotation function can be determined,

$$Q(k, \theta) = \frac{i(BA^* - B^*A)}{|A|^2 + |B|^2} . \quad (154)$$

Clearly, if the scattering function does not depend on spin, $S_{\ell, \ell+1/2} = S_{\ell, \ell-1/2}$, then $B = 0$, and both the polarization, P , and the spin rotation function, Q , will both vanish. The deviation from spin conservation is determined by the ratio of the square of the spin breaking amplitude B to the square of the spin conserving amplitude A and can be determined from the polarization and the spin rotation functions [126,127]

$$|R_s|^2 = \frac{|B|^2}{|A|^2} = \frac{4[(P/2)^2 + (Q/2)^2]}{2 + 2\sqrt{1 - P^2 - Q^2} - P^2 - Q^2} . \quad (155)$$

12.2. Nucleon–nucleus scattering amplitude in the pseudospin representation

From the relation of the pseudo-orbital angular momentum to the orbital angular momentum given in Eq. (70) we define the scattering amplitudes for pseudo-orbital angular momentum as

$$\tilde{S}_{\tilde{\ell}, j=\tilde{\ell}-1/2} = S_{\tilde{\ell}-1, j=\tilde{\ell}-1/2}, \quad \tilde{S}_{\tilde{\ell}, j=\tilde{\ell}+1/2} = S_{\tilde{\ell}+1, j=\tilde{\ell}+1/2} . \quad (156)$$

If we substitute these relations into (151) and use relationships between the Legendre polynomials, we find that the pseudo scattering amplitudes,

$$\begin{aligned} \tilde{A} &= \frac{-i}{2k} \sum_{\tilde{\ell}} [(\tilde{S}_{\tilde{\ell}, \tilde{\ell}+1/2} - 1)(\tilde{\ell} + 1) + (\tilde{S}_{\tilde{\ell}, \tilde{\ell}-1/2} - 1)\tilde{\ell}] P_{\tilde{\ell}}(\cos(\theta)) , \\ \tilde{B} &= \frac{-1}{2p} \sum_{\tilde{\ell}} [\tilde{S}_{\tilde{\ell}, \tilde{\ell}+1/2} - \tilde{S}_{\tilde{\ell}, \tilde{\ell}-1/2}] P_{\tilde{\ell}}^{(1)}(\cos(\theta)) . \end{aligned} \quad (157)$$

are related by a unitary transformation,

$$\begin{pmatrix} \tilde{A} \\ \tilde{B} \end{pmatrix} = \begin{pmatrix} \cos(\theta) & i\sin(\theta) \\ i\sin(\theta) & \cos(\theta) \end{pmatrix} \begin{pmatrix} A \\ B \end{pmatrix} . \quad (158)$$

The polarization and the spin rotation function then become

$$\begin{aligned} P &= \frac{\tilde{B}\tilde{A}^* + \tilde{B}^*\tilde{A}}{|\tilde{A}|^2 + |\tilde{B}|^2} , \\ Q &= \frac{\sin(2\theta)[|\tilde{A}|^2 - |\tilde{B}|^2] + i \cos(2\theta)[\tilde{B}\tilde{A}^* - \tilde{B}^*\tilde{A}]}{|\tilde{A}|^2 + |\tilde{B}|^2} . \end{aligned} \quad (159)$$

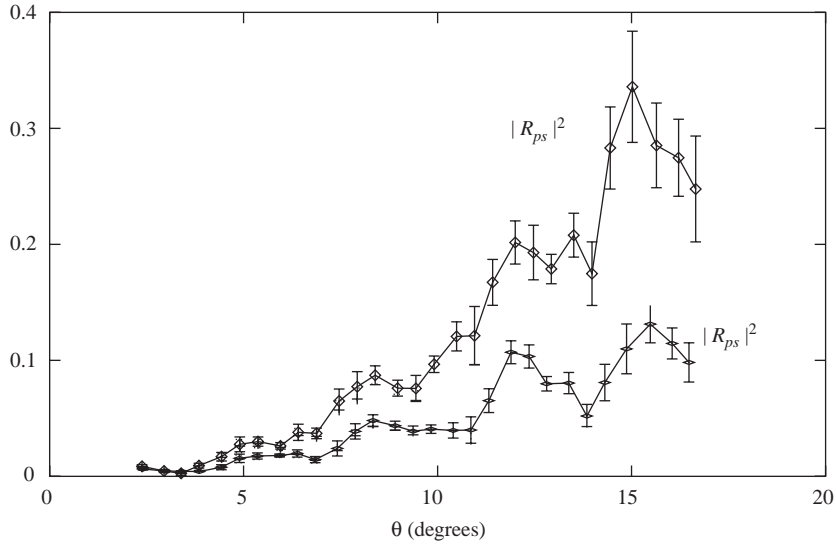


Fig. 36. The spin breaking R_s^2 and pseudospin breaking R_{ps}^2 versus the scattering angle for 800 MeV proton scattering on ^{208}Pb . The lines are a guide to the eye.

In the pseudospin symmetry limit $\tilde{S}_{\tilde{\ell}, \tilde{\ell}+1/2} = \tilde{S}_{\tilde{\ell}, \tilde{\ell}-1/2}$ and hence \tilde{B} will vanish in this limit. Therefore, $P = 0$, just as in the spin limit, but $Q = \sin(2\theta)$ [124].

Of course, just as for the nuclear bound states, pseudospin is broken. The amount of breaking is determined by the ratio of the square of the spin breaking amplitude \tilde{B} to the square of the spin conserving amplitude \tilde{A} and can be determined from the polarization and the spin rotation functions [126,127]

$$|R_{ps}|^2 = \frac{|\tilde{B}|^2}{|\tilde{A}|^2} = \frac{\tan^2(\theta) - Q \tan(\theta) + |R_s|^2(1 - Q \tan(\theta))}{1 + Q \tan(\theta) + |R_s|^2(\tan^2(\theta) + Q \tan(\theta))}. \quad (160)$$

12.3. Experimental tests

We shall now extract the amount of spin and pseudospin breaking from the experimental polarization and spin rotation function measured for 800 MeV proton scattering from ^{208}Pb [128]. For $\theta=0$, $B=0$ because it depends on $P_\ell^{(1)}(\cos(\theta))$ and therefore both the spin and pseudospin violation starts out as zero. In Fig. 36, we see that, up to the angles measured (about a momentum transfer of 2.3 fm^{-1}), the pseudospin symmetry violation increases and reaches a maximum of about 12% whereas the spin breaking reaches a maximum of about 35% about three times pseudospin breaking. Hence, pseudospin symmetry has validity for medium energy nucleon scattering.

However as the energy decreases the pseudospin violation increases [124,129] as seen in Fig. 37 proton scattering from ^{58}Ni and ^{208}Pb at 295 and 200 MeV, respectively. Also the Coulomb potential increases the pseudospin violation in proton nucleus scattering [129] which is consistent with studies on bound states discussed in the last section, Section 11 [121].

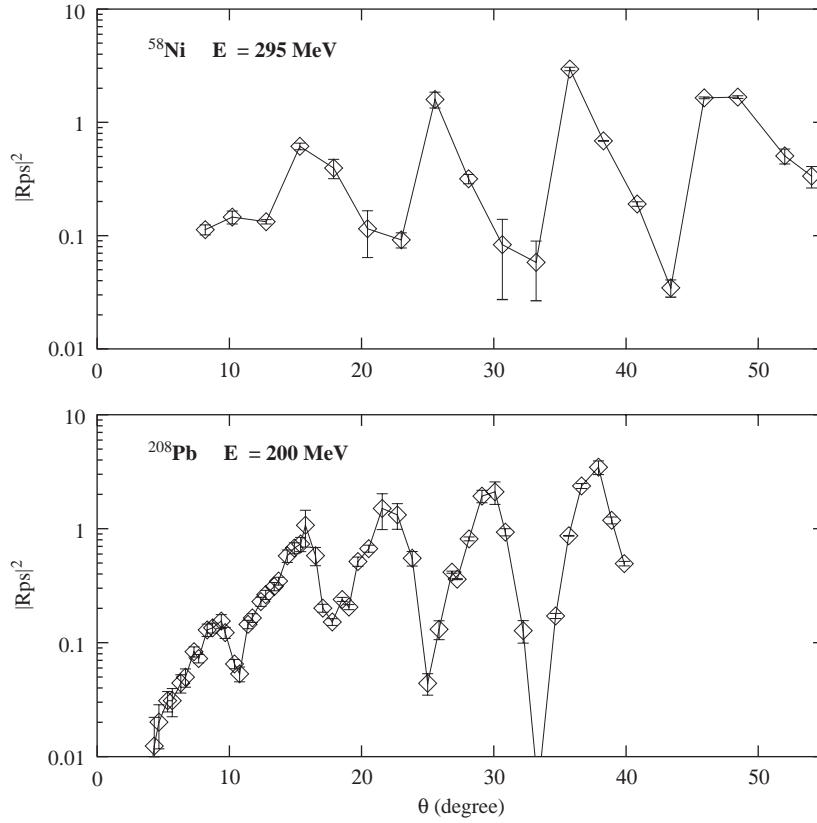


Fig. 37. The pseudospin breaking R_{ps}^2 versus the scattering angle for ^{58}Ni (top) and ^{208}Pb (bottom). The lines are a guide to the eye.

The fact that pseudospin violation decreases as the binding energy decreases for bound nuclei, whereas the pseudospin violation decreases as the scattering energy increases seems puzzling at first sight. However, this outcome makes sense in a simple square well. The energy difference (Eq. (93)) between pseudospin doublets in a simple square well is approximately [6]

$$\Delta E_{\tilde{n}_r, \tilde{\ell}} \approx \frac{(2\tilde{\ell} + 1)(V_S + V_V)}{2MR^2((V_S + V_V) + \bar{\varepsilon}_{\tilde{n}_r, \tilde{\ell}})} , \quad (161)$$

where $\bar{\varepsilon}$ is the average single nucleon energy (Eq. (148)), and the strength of the potentials are V_S , V_V for $r \leq R$ and zero for $r > R$. For bound states $\bar{\varepsilon}_{\tilde{n}_r, \tilde{\ell}}$ is negative and $V_S + V_V$ is negative. Therefore the denominator $((V_S + V_V) + \bar{\varepsilon}_{\tilde{n}_r, \tilde{\ell}})$ increases in magnitude as $\bar{\varepsilon}_{\tilde{n}_r, \tilde{\ell}}$ goes to zero and thus the splitting decreases. However, for scattering states, $\bar{\varepsilon}_{\tilde{n}_r, \tilde{\ell}}$ is positive. Thus, as $\bar{\varepsilon}_{\tilde{n}_r, \tilde{\ell}}$ increases, the denominator increases and thus the splitting decreases.

13. Anti-nucleon spectrum

The anti-nucleon is the anti-particle of the nucleon. Therefore, the potential of the anti-nucleon in the nuclear environment is the charge conjugate of the nucleon. Under charge conjugation the scalar potential remains invariant, $\bar{V}_S(\vec{r}) = C^\dagger V_S(\vec{r}) C = V_S(\vec{r})$, but the vector potential changes sign, $\bar{V}_V(\vec{r}) = C^\dagger V_V(\vec{r}) C = -V_V(\vec{r})$. Therefore for an anti-nucleon in a nuclear environment $\bar{V}_S(\vec{r}) \approx \bar{V}_V(\vec{r})$, and we have approximate spin symmetry [130]. In fact the negative energy solutions to the nucleon mean field do show a strong spin symmetry [131]. However, there are self-consistent effects which mitigate this conclusion [132]. Also the annihilation potential needs to be taken into account to give a reliable prediction of the anti-nucleon spectrum. But, since the annihilation potential exists only for the anti-nucleon mean field potential and not the nucleon mean field potential, the annihilation potential must be equally scalar and vector so that it will vanish under charge conjugation. This means that approximate spin symmetry will remain intact. Indeed, the limited polarized antinucleon scattering data available shows a vanishing small polarization which implies approximate spin symmetry [133].

14. Spin symmetry in hadrons

14.1. Introduction

Spin–orbit splittings in meson and baryon systems, which might be expected to originate from one-gluon-exchange (OGE) effects between quarks, are absent from the observed spectrum for mesons composed of one light quark (antiquark) and one heavy antiquark (quark) [134]. We first elucidate the experimental evidence for small spin–orbit splittings.

14.2. Experimental and lattice QCD spectrum

In the limit where some of the (anti)quarks are infinitely heavy, the angular momentum of the light degrees of freedom, j , is separately conserved [135]. The states can be labelled by l_j , where l is the orbital angular momentum of the light degrees of freedom. In non-relativistic models of conventional mesons and baryons the splitting between $l_{j+1/2}$ and $l_{j-1/2}$ levels, e.g. the $p_{3/2}$ and $p_{1/2}$ or $d_{5/2}$ and $d_{3/2}$ levels, can *only* arise from spin–orbit interactions [134]. The l_j level corresponds to two degenerate broad states with different total angular momenta $J = j \pm s_Q$, where s_Q is the spin of the heavy (anti)quarks [135]. For example in the case of D -mesons, which have a charm quark and a light quark, $l_j = p_{1/2}$ and $p_{3/2}$ and $s_Q = \frac{1}{2}$. For $p_{1/2}$ the two states are called D_0^* and D_1' and for $p_{3/2}$ states D_1 the two states are called D_2^* [135]. The degenerate states separate as one moves slightly away from the heavy quark limit, and their spin-averaged mass remains approximately equal to the mass before separation.

For the D -mesons, the Belle collaboration [136] observes two broad states with masses $M_{D_0^*} = 2308 \pm 17 \pm 15 \pm 28$ MeV and $M_{D_1'} = 2427 \pm 26 \pm 20 \pm 15$ MeV and two narrow states with masses $M_{D_2^*} = 2461.6 \pm 2.1 \pm 0.5 \pm 3.3$ MeV and $M_{D_1} = 2421.4 \pm 1.5 \pm 0.4 \pm 0.8$ MeV giving a remarkably small $p_{3/2} - p_{1/2}$ spin–orbit splitting of 49 ± 50 MeV.

For the K -mesons, which have a strange quark and a light quark, the $p_{1/2}$ level is at 1409 ± 5 MeV, with $p_{3/2}$ nearby at 1371 ± 3 MeV, corresponding to a $p_{3/2} - p_{1/2}$ splitting of -38 ± 6 MeV. The splitting between the higher-lying $d_{5/2}$ and $d_{3/2}$ levels is -4 ± 14 or 41 ± 13 MeV, depending on how the states

are paired into doublets. These results indicate a near spin–orbit degeneracy if the strange quark can be treated as heavy, although it has certainly not been established that such a treatment is valid.

For B -mesons, which have a bottom quark and a light quark, L3 has performed an analysis, using input from theoretical models and heavy quark effective theory, to determine that the $p_{3/2} - p_{1/2}$ splitting is 97 ± 11 MeV [137]. Note that this is *not* a model-independent experimental result. In the same analysis the mass difference between the B_2^* and B_0^* , an approximate indicator of the $p_{3/2} - p_{1/2}$ splitting, is 110 ± 11 MeV. The latter agrees with lattice QCD estimates of $155_{-13}^{+9} \pm 32$ MeV [138] and 183 ± 34 MeV [139]. However, according to another estimate [140], the splitting is less than 100 MeV, and consistent with zero. Most recently, 31 ± 18 MeV was calculated [141]. One lattice QCD study found evidence for a change of sign in the splitting somewhere between the charm and bottom quark masses, albeit with large error bars [142]. A splitting of 40 MeV serves as an example of relativized quark model predictions [143].

In order to measure quantitatively the spin–orbit splitting, we take the ratio of the spin–orbit energy splitting between the $p_{1/2}$ and $p_{3/2}$ states to the difference of the average $p_{1/2}$ and $p_{3/2}$ energies with the ground state, $r = (p_{3/2} - p_{1/2}) / ((4p_{3/2} + 2p_{1/2})/6 - s_{1/2})$, where all entries refer to masses. The experimental data on D , K and B mesons give respectively $r = 0.10 \pm 0.05$, -0.06 ± 0.00 and 0.23 ± 0.04 . For the Dirac equation with arbitrary vector and scalar Coulomb potentials, the only potential for which the relevant analytic solutions are known, $-0.7 \leq r \leq 0.6$. It is hence evident that the spin–orbit splittings extracted from experimental results are indeed small.

Dynamical QCD calculations on the lattice for which one quark is light and the other is taken to be infinitely heavy give small spin–orbit splittings which decrease as the orbital angular momentum increases [144].

There is also evidence in light quark mesons and baryonic systems that the spin–orbit interaction is small [134]. In non-relativistic models, meson and “two-body” baryon spin–orbit interactions are related and, for a specific class of baryons, the spin–orbit interaction is small for exactly the same reasons that it is small in mesons, which is conjectured to be an “accidental” cancellation between OGE and Thomas precession effects [134].

We speculate that the small spin–orbit splittings are due to a relativistic symmetry. The dynamics of a light quark (antiquark) in the field of a heavy antiquark (quark) can be approximated by the Dirac Hamiltonian. So, therefore, the system will have a spin symmetry if the scalar and vector potentials are equal in magnitude.

14.3. Experimental test of relativistic spin symmetry

As discussed in Section 7.3, in the spin symmetry limit, the radial amplitudes of the upper components of the Dirac wavefunction of the two states in the spin doublet will be identical, behaving “non-relativistically”, whereas the lower components will have different radial wavefunctions.

Likewise the momentum space wavefunctions for the upper components will be identical in the spin symmetry limit, again because the spin operator does not affect the wavefunction. However, since U_p depends only on the angular part of the momentum, $\hat{p} = \frac{\vec{p}}{p}$, it does not affect the radial momentum space wavefunction.

The potential between quarks at small distances is due to one gluon exchange and hence is Coulomb-like. In order to see the effect of the small spin symmetry breaking on the amplitudes we use the analytical Coulomb Dirac eigenfunctions derived in Section 15.4. We take $V_S(r) = \alpha_S/r + U_S$ and $V_V(r) =$

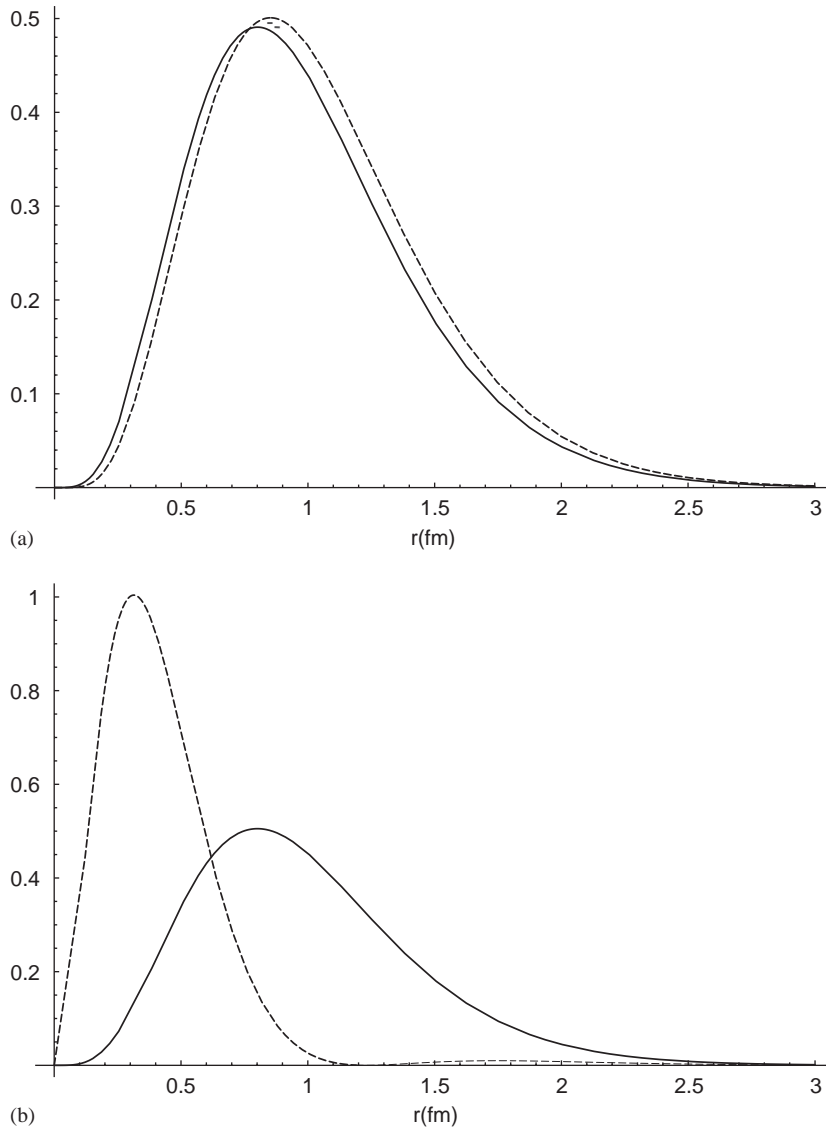


Fig. 38. (a) The square of the Dirac radial wavefunction of the upper component times r^2 . (b) The square of the Dirac radial wavefunction of the lower component times r^2 . $p_{3/2}$ is the solid line and $p_{1/2}$ is the dashed line. Note that the lower component is comparable to the upper component. The wavefunctions are solutions of the Dirac equation (see Eq. (1)) with Coulomb potentials $V_S(r) = \alpha_S/r + U_S$ and $V_V(r) = \alpha_V/r + U_V$, where $\alpha_S = -1.279$, $U_S = 506$ MeV, $\alpha_V = -0.779$, $U_V = 515$ MeV, $m = 330$ MeV and $M = 1480$ MeV. This corresponds to a $p_{3/2} - p_{1/2}$ splitting of -52 MeV.

$\alpha_V/r + U_V$, where $U_{S,V}$ are constants. As an example, in Fig. 38 the upper and lower components for Dirac wavefunctions of the $p_{1/2} - p_{3/2}$ doublet. The scalar and vector potentials were determined by matching the available spectral data of mesons, assuming a $p_{3/2} - p_{1/2} = -52$ MeV. This maximizes the wavefunction differences. In this realistic case, $V_V(r) \approx V_S(r) + U_S - U_V$, so the radial wavefunctions

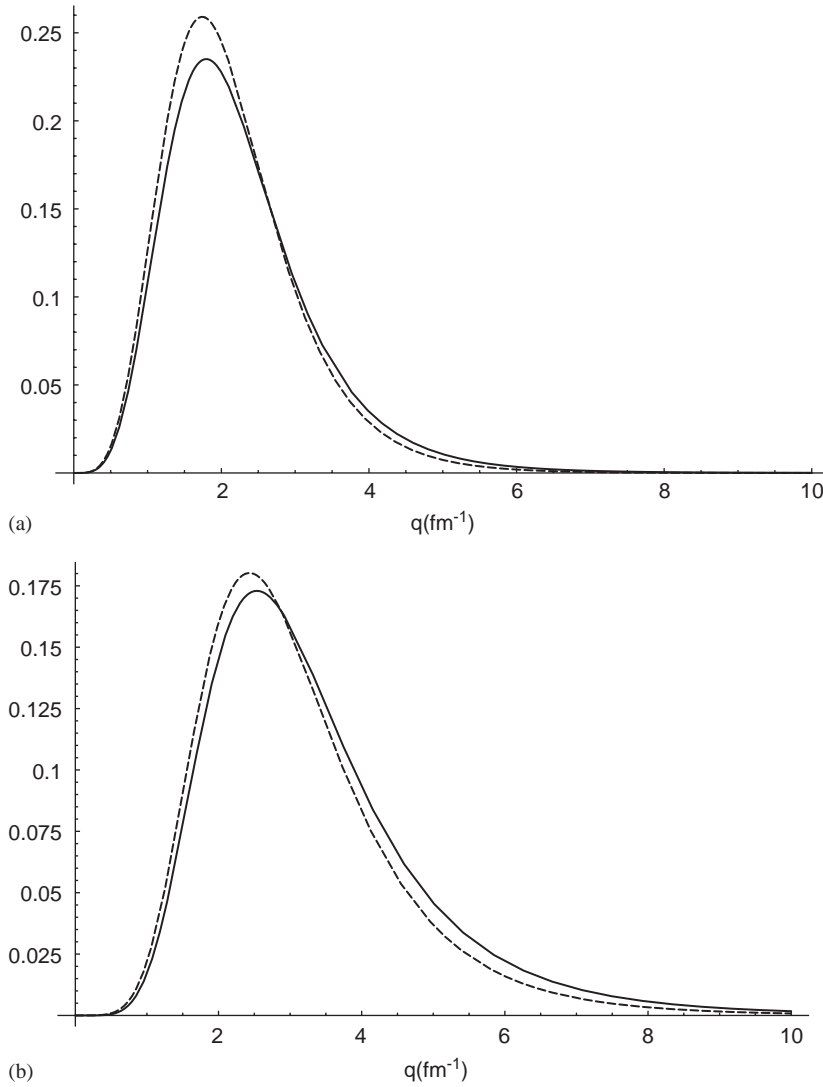


Fig. 39. (a) The square of the Dirac momentum space wavefunction of the upper component times q^2 . (b) The square of the Dirac momentum space wavefunction of the lower component times q^2 . Other conventions are the same as in Fig. 38.

for the upper components are not exactly identical but are very close, whereas the radial wavefunctions for the lower components are very different. The lower components are also comparable in magnitude to the upper components implying that the system is very relativistic. In Fig. 39 we see that the radial momentum space amplitudes are very similar for both the upper and the lower components as well. This prediction of spin symmetry can be tested in the following experiments.

The annihilation $e^+e^- \rightarrow D_0^*D_0^*, D_0^*D_2^*$ and $D_2^*D_2^*$ allows for the extraction of the D_0^* and D_2^* electromagnetic static form factors and the D_0^* to D_2^* electromagnetic transition form factor. The photon interaction ensures that all radial amplitudes of the light quark are accessed. When spin symmetry is realised, there are only two independent radial momentum space amplitudes, which should enable the

prediction of one of the three form factors in terms of the other two. Thus the verification of the predictions of spin symmetry is possible. On the other hand, non-relativistic models, with no lower components for the wavefunctions, have only one independent radial wavefunction, which will lead to the prediction of two of the form factors in terms of the remaining one. This might be too restrictive. The proposed experiment can be carried out at the Beijing Electron Positron Collider at an energy of approximately 1 GeV above the $\psi(4040)$ peak in the final state $DD\pi\pi$.

An equivalent experiment for K -mesons would involve detection of the $KK\pi\pi$ final state, which has already been measured [145]. The wavefunctions of K -mesons fitting the experimental spectrum show similar behaviour to the D -mesons, with the $p_{3/2}$ and $p_{1/2}$ wavefunctions even more similar than in Figs. 38a and 39.

If B -mesons do also exhibit spin symmetry, one can do equivalent experiments around 1 GeV above the $\Upsilon(3S)$ peak at the SLAC, KEK or CESR B -factories.

14.4. QCD origins

One gluon exchange produces a linearly increasing vector potential between a quark and an antiquark [146]. Presumably the scalar potential comes from two or more gluon exchange [147] which is consistent with lattice QCD results [148]. Hence spin symmetry in hadrons has QCD origins as does pseudospin symmetry as we have seen in Section 6. The puzzle is why do we have spin symmetry in hadrons and pseudospin symmetry in nuclei?

14.5. Summary

The observation of “accidental” spin–orbit degeneracies observed in heavy-light quark mesons can be explained by a relativistic symmetry of the Dirac Hamiltonian which occurs when the vector and scalar potentials exerted on the light quark by the heavy antiquark differ approximately by a constant, $V_V(r) \approx V_S(r) + U$. Conversely, if future experiments determine that spin–orbit splittings are small not only for the lowest excited states in mesons but are small throughout the meson spectrum, this experimental fact dictates that the effective QCD vector and scalar potentials between a quark and antiquark are approximately equal up to a constant, which would be a significant observation about the nature of non-perturbative QCD. Furthermore, the approximate symmetry predicts that the spatial Dirac wavefunction for the spin doublets will be approximately equal in momentum space, a feature which can be tested in electron-positron annihilation.

15. Exactly solvable Dirac Hamiltonians

The Dirac Hamiltonian can be solved exactly in terms of the special functions for two potentials: harmonic oscillator in either the spin or pseudospin limit and the Coulomb for all strengths. We discuss both.

15.1. Relativistic harmonic oscillator with spin symmetry

If the scalar and vector potentials are equal up to a constant, $V_S(\vec{r}) = V(\vec{r})/2 + V_S^0$, $V_V(\vec{r}) = V(\vec{r})/2 + V_V^0$, and are harmonic oscillator, $V(\vec{r}) = (\tilde{M}/2) \sum_{i=1}^3 \omega_i x_i^2$, with $\tilde{M} = M + V_S^0$ (we have set $\hbar = c = 1$), the

Dirac Hamiltonian is exactly solvable [11]. We shall only discuss the spherical symmetry limit, $\omega_i = \omega$, here [150–154].

15.1.1. Eigenfunctions

The upper amplitudes of the eigenfunctions are

$$g_{n_r, \ell}(r) = \mathcal{N}(E_N) \sqrt{\frac{2\lambda^3 n!}{\Gamma(\ell + n + \frac{3}{2})}} e^{-x^2/2} x^\ell L_{n_r}^{(\ell+1/2)}(x^2), \quad (162)$$

where $L_n^{(\ell+1/2)}(x^2)$ is the Laguerre polynomial, $x = \lambda r$, $r = \sqrt{\sum_{i=1}^3 x_i^2}$ is the radial coordinate,

$$\lambda = \left[(\tilde{E}_N + \tilde{M}) \frac{\tilde{M}\omega^2}{2} \right]^{1/4}, \quad (163)$$

and

$$\mathcal{N}(E) = \sqrt{\frac{2(\tilde{E} + \tilde{M})}{3\tilde{E} + \tilde{M}}}, \quad (164)$$

with $\tilde{E} = E - V_V^0$. The lower components are

$$f_{n_r, \ell, j=\ell-1/2}(r) \quad (165)$$

$$\begin{aligned} &= -\frac{\mathcal{N}(E_N)}{\tilde{M} + \tilde{E}_N} \sqrt{\frac{2\lambda^5 n!}{\Gamma(\ell + n_r + \frac{3}{2})}} e^{-x^2/2} x^{\ell-1} \\ &\quad \times ((n_r + 1)L_{n_r+1}^{(\ell-1/2)}(x^2) + \left(n_r + \ell + \frac{1}{2}\right) L_{n_r}^{(\ell-1/2)}(x^2)), \end{aligned} \quad (166)$$

$$f_{n_r, \ell, j=\ell+1/2}(r) = \frac{\mathcal{N}(E_N)}{\tilde{M} + \tilde{E}_N} \sqrt{\frac{2\lambda^5 n!}{\Gamma(\ell + n_r + \frac{3}{2})}} e^{-x^2/2} x^{\ell+1} (L_{n_r}^{(\ell+3/2)}(x^2) + L_{n_r-1}^{(\ell+3/2)}(x^2)). \quad (167)$$

The function $f_{n_r, \ell, j=\ell-1/2}(r)$ has $n_r + 1$ nodes, one more node than the upper component. The amplitude $f_{n_r, \ell, j=\ell+1/2}(r)$ has the same number of nodes as the upper component. This agrees with the general theorem relating the number of radial nodes of the lower components to the number of radial nodes of the upper component [16].

15.1.2. Energy eigenvalues

The energy eigenvalue solution is

$$E_N = \tilde{M} \left[B(A_N) + \frac{1}{3} + \frac{4}{9B(A_N)} \right] + V_V^0, \quad (168)$$

where

$$B(A_N) = \left[\frac{A_N + \sqrt{A_N^2 - \frac{32}{27}}}{2} \right]^{2/3}, \quad (169)$$

$A_N = C(N + \frac{3}{2})$, $C = \sqrt{2}\omega/\tilde{M}$, and N is the total oscillator quantum number, $N = 2n + \ell = 0, 1, \dots$. We note that there is not only a degeneracy due to spin symmetry but there is also the usual degeneracy of the non-relativistic harmonic oscillator; namely, that the energy depends only on the total harmonic oscillator quantum number and the states with $\ell = N, N - 2, \dots, 0$ or 1 are all degenerate.

The eigenvalues E_N are real for all values of N as long as $C_i, V_{S,V}^0$ are real. Although true it is not obvious because $B(A_N)$ is not real for all A_N real. From Eq. (169), $B(A_N)$ is clearly complex for $A_N < \sqrt{\frac{32}{27}}$. However, we now show analytically that E_N will still be real even if $B(A_N)$ is complex as long as $|B(A_N)| = 2/3$.

The imaginary part of E_N is

$$\text{Im } E_N = \frac{\left[B(A_N) + \frac{1}{3} + \frac{4}{9B(A_N)} \right] - \left[B(A_N) + \frac{1}{3} + \frac{4}{9B(A_N)} \right]^*}{2i}. \quad (170)$$

Writing $B(A_N) = |B(A_N)|e^{i\psi}$

$$\text{Im } E_N = \left(|B(A_N)| - \frac{4}{9|B(A_N)|} \right) \sin \psi, \quad (171)$$

and therefore E_N is real if $|B(A_N)| = 2/3$ independent of ψ . One can show numerically that $|B(A_N)| = 2/3$ for all A_N in the range from zero to $\sqrt{\frac{32}{27}}$, $0 \leq A_N \leq \sqrt{\frac{32}{27}}$. For $A_N \geq \sqrt{\frac{32}{27}}$, $B(A_N)$ is clearly real and hence E_N is real.

The spectrum is non-linear in contrast to the non-relativistic harmonic oscillator. However for small A_N

$$E_N \approx \tilde{M} \left(1 + \frac{A_N}{\sqrt{2}} + \dots \right) + V_V^0 \quad (172)$$

and therefore the binding energy, $E_N - \tilde{M} \approx \omega(N + \frac{3}{2}) + V_V^0$, in agreement with the non-relativistic harmonic oscillator. For large A_N the spectrum goes as

$$E_N \approx \tilde{M} \left(A_N^{2/3} + \frac{1}{3} + \dots \right) + V_V^0, \quad (173)$$

which, in lowest order, agrees with the spectrum for $\tilde{M} \rightarrow 0$ [155].

In Fig. 40 we plot the spherical harmonic oscillator energies $\varepsilon_N = E_N - M$ with E_N given in Eq. (168), the solid curve, as a function of N . We chose the parameters to fit the lowest eigenenergies

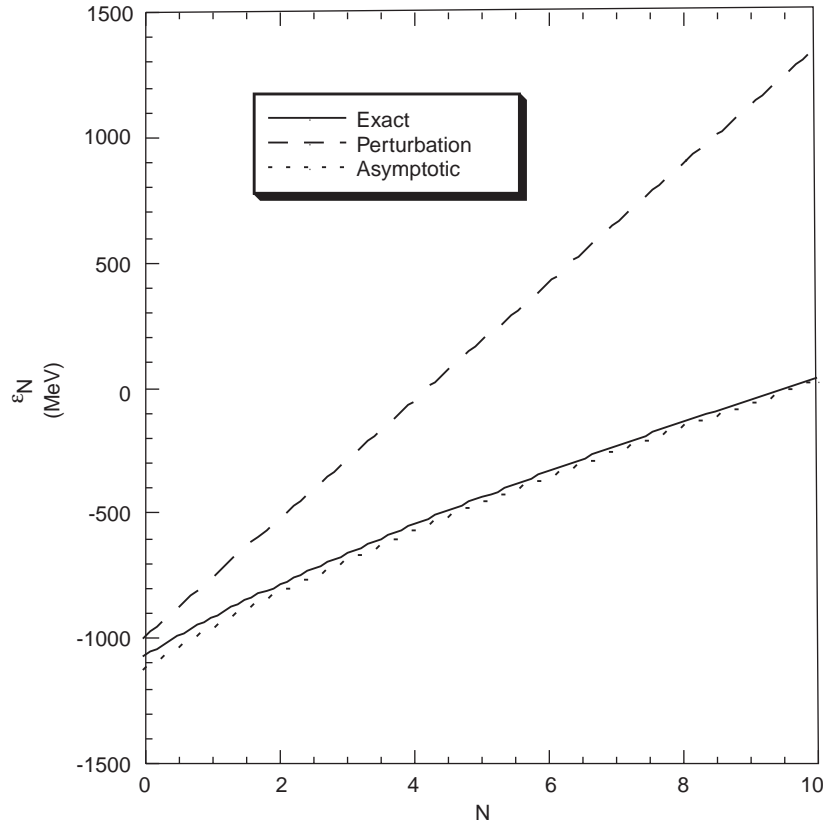


Fig. 40. The Dirac single particle energies, ε_N , for the spherical harmonic oscillator as a function of N . The exact energies are the solid line, the perturbation approximation is the dashed line, and the asymptotic approximation is the short dashed line.

of the spectrum of an anti-proton outside of ^{16}O in the relativistic mean field approximation [132] and they are $C = 1.33$, $\tilde{M} = 252 \text{ MeV}$, and $V_V^0 = -677 \text{ MeV}$.

The dashed curve is ε_N using the perturbation approximation of E_N given in Eq. (172). The short-dashed curve is ε_N using the asymptotic limit of E_N given in Eq. (173). Clearly the eigenenergies are in the relativistic asymptotic regime and not the linear regime of the non-relativistic harmonic oscillator.

In Fig. 41 we plot the spherical harmonic oscillator excitation energies $E_N^* = E_N - E_0$ for different N on the far left. Each level has a $(N + 2)(N + 1)$ degeneracy because of spin symmetry and because the allowed orbital angular momenta are $\ell = N, N - 2, \dots, 0$ or 1 and the allowed orbital angular momentum projections are $m = \ell, \ell - 1, \dots, -\ell$.

The non-spherical spin symmetric relativistic harmonic oscillator for triaxial and deformed axially symmetric shapes has been solved as well [11]. The energy eigenvalues have the same functional form as in Eq. (168) but the variable A is given by the sum of the number of nodes along each of the three axes weighted by the harmonic oscillator strength in that direction. In the right of Fig. 41 we plot the deformed excitation energies $E_{N,n_3}^* = E_{N,n_3} - E_{0,0}$ where n_3 is the number of harmonic oscillator quanta in the z -direction [11]. The deformed excitation energies are staggered in groups for each N and each group contains the levels for $n_3 = 0, 1, \dots, N$ with the excitation energy increasing with decreasing n_3 . The

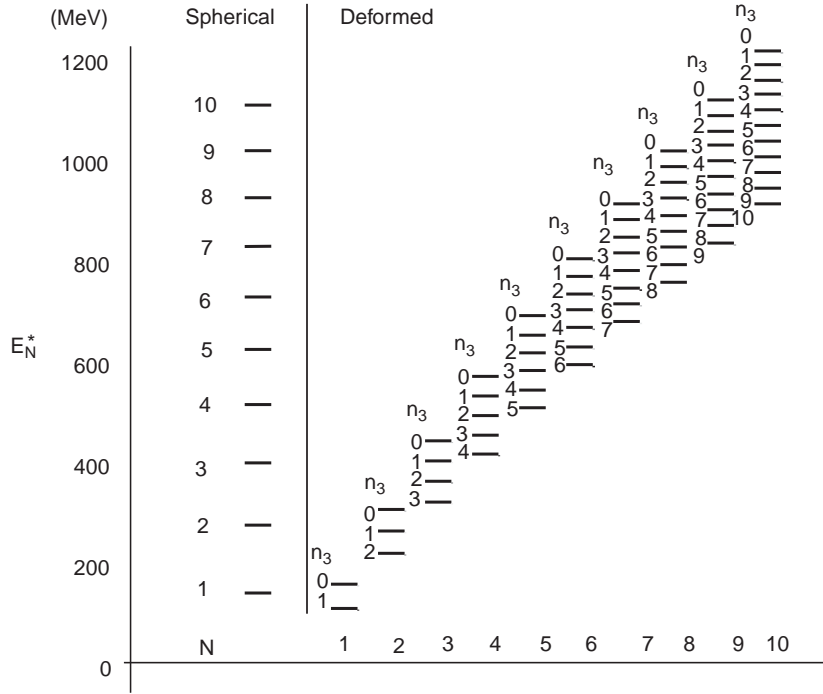


Fig. 41. On the left the excitation energies, E_N^* , for the spherical harmonic oscillator are plotted for each N . Each level has a $(N+2)(N+1)$ degeneracy because of spin symmetry and because the allowed orbital angular momenta are $\ell = N, N-2, \dots, 0$ or 1 and the allowed orbital angular momentum projections are $m = \ell, \ell-1, \dots, -\ell$. On the right the excitation energies, E^* , for the deformed harmonic oscillator are plotted in staggered groups for each N . Each group contains the levels for $n_3 = 0, 1, \dots, N$. Each level has a $2(N-n_3)+1$ degeneracy for $(N-n_3)$ even and a $2(N-n_3+1)$ degeneracy for $(N-n_3)$ odd because of spin symmetry and because the allowed orbital angular momentum projections are $A = \pm(N-n_3), \pm(N-n_3-2), \dots, \pm 1$ or 0.

dimensionless oscillator strengths are determined by $C^3 = C_\perp^2 C_3$ and assuming a deformation $\delta = 0.33$ which leads to $C_\perp = 1.49$, $C_3 = 1.05$ [10]. Each level has a $2(N-n_3)+1$ degeneracy for $(N-n_3)$ even and a $2(N-n_3+1)$ degeneracy for $(N-n_3)$ odd because of spin symmetry and because the allowed orbital angular momentum projections are $A = \pm(N-n_3), \pm(N-n_3-2), \dots, \pm 1$ or 0. The splitting of the levels within each N appears to be approximately linear with n_3 .

15.1.3. Relativistic contribution

The normalization $\mathcal{N}(E)$ has the same functional form independent on whether the harmonic oscillator is triaxial, axially deformed, or spherical [11]. This normalization has also been calculated independently by using $\int_{-\infty}^{\infty} dx \int_{-\infty}^{\infty} dy \int_{-\infty}^{\infty} dz (|f_{\mu}^+(\vec{r})|^2 + |f_{\mu}^-(\vec{r})|^2) = \int_{-\infty}^{\infty} dx \int_{-\infty}^{\infty} dy \int_{-\infty}^{\infty} dz g(\vec{r})^* \frac{p^2}{(E+\tilde{M})^2} g(\vec{r})$ and we find agreement between the two different ways of calculating $\mathcal{N}(E)$.

This also tells us that the probability of the lower component to the upper component is given by

$$R_k = \frac{\int_{-\infty}^{\infty} dx \int_{-\infty}^{\infty} dy \int_{-\infty}^{\infty} dz (|f_{k,\mu}^+(\vec{r})|^2 + |f_{k,\mu}^-(\vec{r})|^2)}{\int_{-\infty}^{\infty} dx \int_{-\infty}^{\infty} dy \int_{-\infty}^{\infty} dz |g_k(\vec{r})|^2} = \frac{\tilde{E}_k - \tilde{M}}{2(\tilde{E}_k + \tilde{M})}. \quad (174)$$

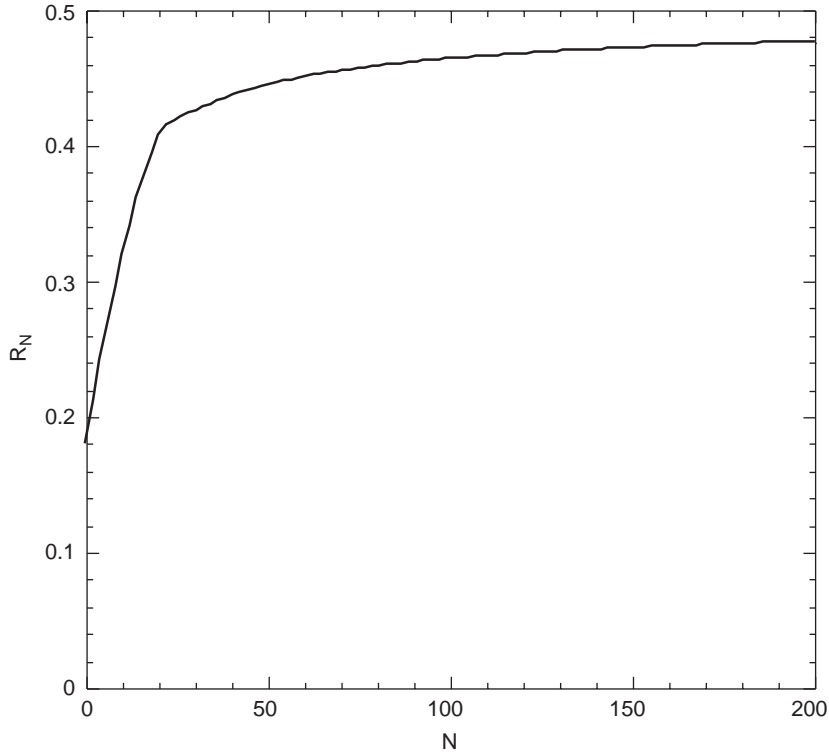


Fig. 42. The ratio of the probability of the lower components to the upper components, R_N , for the spherical harmonic oscillator as a function of N .

Thus for $\tilde{E}_k \approx \tilde{M}$ the system is not very relativistic and the contribution of the lower components is small. For $\tilde{E}_k \gg \tilde{M}$, this ratio approaches $\frac{1}{2}$. For free particles this ratio approaches unity which indicates that the harmonic oscillator reduces the relativistic effect.

In Fig. 42 we plot this ratio for the spherical harmonic oscillator, R_N , as a function of N . Even for the most bound states this probability is about 20% and thus the antinucleon bound inside the nucleus is much more relativistic than a nucleon inside a nucleus for which this probability is about 1%.

15.2. Relativistic harmonic oscillator with pseudospin symmetry

The relativistic harmonic oscillator in the pseudospin limit does have positive energy bound states [157,158]. This is in contrast to finite potentials, which, as shown in Section 3, do not have positive energy bound states. The reason the argument in Section 3 is not valid for the harmonic oscillator is that $A(r)$ in Eq. (81a) is not always positive because $V_S(r) - V_V(r) \rightarrow -\infty$ as $r \rightarrow \infty$ instead of going to zero as is the case for finite potentials.

The energy eigenvalue equation is

$$\tilde{E}_{\tilde{N}} = \tilde{M} \left[\tilde{B}(A_{\tilde{N}}) - \frac{1}{3} + \frac{4}{9\tilde{B}(A_{\tilde{N}})} \right] + \tilde{V}_V^0, \quad (175)$$

where

$$\tilde{B}(A_{\tilde{N}}) = \left[\frac{A_{\tilde{N}} + \sqrt{A_{\tilde{N}}^2 + \frac{32}{27}}}{2} \right]^{\frac{2}{3}}, \quad (176)$$

where $A_{\tilde{N}} = C(\tilde{N} + \frac{3}{2})$, $C = \sqrt{2}\omega/\tilde{M}$, and \tilde{N} is the total pseudo-oscillator quantum number, $\tilde{N} = 2\tilde{n}_r + \tilde{\ell} = 0, 1, \dots$. We note that there is not only a degeneracy due to pseudospin symmetry but the energy depends only on the total pseudo-oscillator quantum number and the states with pseudo-angular momentum $\tilde{\ell} = \tilde{N}, \tilde{N} - 2, \dots, 0$ or 1 are all degenerate. Thus the energy spectrum is positive and real for all \tilde{N} .

However, the spectrum of this pseudospin symmetric relativistic harmonic oscillator will be unrealistic. For example the lowest energy state will be the $0p_{1/2}$ state since it has $\tilde{n}_r = 0, \tilde{\ell} = 0$. In addition the spin aligned states with zero radial nodes, $0s_{1/2}, 0p_{3/2}$, etc., do not exist which means that there are no “intruder” states. Furthermore, the eigenstates will have the wrong nodal structure for “positive” energy states as given in Eq. (89). For example, the lower component of the $1s_{1/2}$ state has no radial nodes instead of one node [158]. In fact the eigenstates have the nodal structure of the “negative” energy states shown in Eq. (90).

15.3. Dirac Hamiltonian with a tensor potential

Although in this review we have focussed on vector and scalar potentials, a particle interacting with an external electric field E_j through its anomalous magnetic moment, μ_A , is described by a Dirac Hamiltonian with a tensor potential $2i\mu_A\beta\gamma_j E_j$. If the electric field is linear in the radial coordinate, $E_j = E_0 r_j$, then this Dirac Hamiltonian can be solved exactly and this system has become known as a “Dirac Oscillator” because its eigenfunctions are harmonic oscillator wavefunctions [159–162]. However, its spectrum is far from harmonic oscillator-like. The eigenvalues for the spin aligned states with the same radial quantum number have the same energy producing infinite degeneracies. Therefore this potential is not realistic for nuclei. However a small admixture with equal scalar and vector potentials provide realistic spin–orbit splittings [153,158].

15.4. Relativistic Coulomb potential and its analytical solutions

The Dirac Hamiltonian, H_c , with spherical scalar and vector potentials of the Coulomb shape, $V_S = \alpha_S/r$, $V_V = \alpha_V/r$, can be solved analytically for arbitrary strengths of vector and scalar potentials, not just in the spin and pseudospin limits [7]. We use the convention introduced in Section 3.2 with the κ quantum number defined in Eqs. (75)–(77). The upper and lower radial amplitudes are

$$g_{\tilde{n}_r, \kappa}(x) = N_{\tilde{n}_r, \kappa} e^{-x/2} x^{\gamma-1} F_{\tilde{n}_r, \kappa}^+(x), \quad (177a)$$

$$f_{\tilde{n}_r, \kappa}(x) = -\frac{N_{\tilde{n}_r, \kappa}}{\mu_{\tilde{n}_r, \kappa}} e^{-x/2} x^{\gamma-1} F_{\tilde{n}_r, \kappa}^-(x), \quad (177b)$$

where

$$F_{\bar{n}_r, \kappa}^{\pm}(x) = v_{\bar{n}_r, \kappa} F[-\bar{n}_r, 2\gamma + 1, x] \pm \bar{n}_r F[-\bar{n}_r + 1, 2\gamma + 1, x] , \quad (177c)$$

$F[a, b, x]$ is the confluent hypergeometric function and

$$N_{\bar{n}_r, \kappa} = \frac{2\lambda\sqrt{2\lambda\Gamma[2\gamma + 1 + \bar{n}_r]}}{\bar{n}_r! \Gamma[2\gamma + 1] \sqrt{(1 + \mu_{\bar{n}_r, \kappa}^{-2}) \left(1 + \frac{2\gamma + \bar{n}_r}{v_{\bar{n}_r, \kappa}^2}\right)}} , \quad (178a)$$

$$\gamma = \sqrt{\kappa^2 - \alpha_V^2 + \alpha_S^2} , \quad (178b)$$

$$\lambda = \sqrt{M^2 - E_{\bar{n}_r, \kappa}^2} , \quad (178c)$$

$$\mu_{\bar{n}_r, \kappa} = \sqrt{\frac{M + E_{\bar{n}_r, \kappa}}{M - E_{\bar{n}_r, \kappa}}} , \quad (178d)$$

$$v_{\bar{n}_r, \kappa} = \frac{1}{2}(\alpha_S + \alpha_V)\mu_{\bar{n}_r, \kappa} + \frac{1}{2} \frac{(\alpha_V - \alpha_S)}{\mu_{\bar{n}_r, \kappa}} + \kappa . \quad (178e)$$

For $\kappa < 0$ the quantum number \bar{n}_r takes on integer values $\bar{n}_r = 0, 1, 2, \dots$ and is the number of radial nodes. For $\kappa > 0$ the quantum number \bar{n}_r takes on integer values $\bar{n}_r = 1, 2, \dots$ and $\bar{n}_r - 1$ is the number of radial nodes. This follows from the fact that $v_{0, \kappa} = 0$ for $\kappa > 0$ and thus the amplitudes $g_{\bar{n}_r, \kappa}(x)$, $f_{\bar{n}_r, \kappa}(x)$ in Eq. (177) vanish for $\kappa > 0$.

The energy eigenvalues are

$$E_{\bar{n}_r, \kappa}^{\pm} = M \left[\frac{-\alpha_V \alpha_S \pm (\bar{n}_r + \gamma) \sqrt{\alpha_V^2 - \alpha_S^2 + (\bar{n}_r + \gamma)^2}}{\alpha_V^2 + (\bar{n}_r + \gamma)^2} \right] . \quad (179)$$

In the non-relativistic limit $\alpha_{S, V}$ small, the eigenenergies become

$$E_{\bar{n}_r, \kappa}^+ \approx M \left[1 - \alpha_S \alpha_V - \frac{\alpha_S^2 + \alpha_V^2}{2n^2} \right] , \quad (180)$$

where n is the principal quantum number $n = \bar{n}_r + |\kappa|$ [7]. Thus the eigenstates with the same principal quantum number are degenerate which follows from an $O(4)$ symmetry [163].

The relativistic Coulomb potential breaks this symmetry but the eigenstates with the same \bar{n}_r and $|\kappa|$ will have the same energy; that is, the states with the same principal quantum number *and* the same j , $1s_{1/2}$ and $0p_{1/2}$, $1p_{3/2}$ and $0d_{3/2}$, etc., will remain degenerate. The generator of this symmetry

$$B = -i\hat{K}\gamma_5(H_c - \beta M) + \frac{\vec{\sigma} \cdot \vec{r}}{r} (\alpha_V M + \alpha_S H_c) , \quad (181)$$

commutes with the Dirac Hamiltonian H_c and anticommutes with $\hat{\kappa}$ given in Eq. (75), producing a supersymmetry [164].

In the spin limit, $\alpha_S = \alpha_V$, and the pseudospin limit, $\alpha_S = -\alpha_V$, the eigenenergies become

$$E_n^{s\pm} = M \left[\frac{-\alpha_V^2 \pm n^2}{\alpha_V^2 + n^2} \right], \quad (182)$$

$$E_n^{ps\pm} = M \left[\frac{\alpha_V^2 \pm n^2}{\alpha_V^2 + n^2} \right], \quad (183)$$

respectively, and thus only depend on the principal quantum number which follows from spin and pseudospin symmetry.

In the spin limit $E_n^{s-} = -M$ so there are no bound Dirac negative energy or sea states, while in the pseudospin limit $E_n^{ps+} = M$ so there are no bound Dirac positive energy or valence states as shown in general in Section 3.3. However, even for an infinitesimal difference between strengths $\alpha_S = -\alpha_V + \delta$ an infinite number of bound states appear and the positive energy is, up to third order in δ ,

$$E_{\tilde{n}_r, \kappa}^+ \approx M \left[1 - \frac{\delta^2}{2n^2} + \frac{\alpha_V \delta^3}{2n^4(1 - 2n/|\kappa|)} + \dots \right]. \quad (184)$$

Therefore pseudospin symmetry exists up to second order in δ and is broken only in third order [6].

16. Pseudospin in nucleon–nucleon scattering

Because of the success of approximate pseudospin symmetry in nuclei and because of the relationship of pseudospin symmetry with QCD, we would like to determine if pseudospin symmetry has a more fundamental rationale. For this reason we ask the question: Is pseudospin symmetry approximately conserved in the nucleon–nucleon interaction? The nucleon–nucleon interaction is quite complicated including both central and non-central interactions like the tensor interaction. For this reason it is obvious that the nucleon–nucleon interaction does not conserve spin. On the other hand, there exists nucleon–nucleon interactions that conserve pseudospin symmetry and have both central and non-central interactions. Hence the issue of pseudospin conservation is not obvious.

16.1. Spin–pseudospin transformation matrix for scattering states

The nucleon–nucleon scattering matrix is tabulated in the spin basis. The spin (S)-orbital angular momentum (L) non-relativistic basis for the nucleon–nucleon scattering states is of the form

$$|f_L, L, S, J, M, T, T_z\rangle = f_L(r)[Y^{(L)}(\hat{r})[\chi(1)\chi(2)]^{(S)}]_M^{(J)}[\psi(1)\psi(2)]_{T_z}^{(T)}, \quad (185)$$

where f_L is a spherical Bessel of the first or second kind or a linear combination of both, \vec{r} is the relative distance between the two nucleons and \hat{r} its unit vector, $\chi(i)$ is the spin function for the i th particle, $\psi(i)$

is the isospin function for the i th particle, J, M are the total angular momentum and its projection, and T, T_z are the total isospin and its projection. For $S=0$ the basis states will have $L=J$, whereas for $S=1$, $L=J, J-1, J+1$. Since the states must be antisymmetric, $L+S+T$ must be odd.

The spin generators and pseudospin generators for two nucleons is just the sum of the generators for each nucleon. From Eqs. (20) and (52) we see that the transformation from spin to pseudospin is for two nucleons is

$$\vec{\tilde{S}} = \mathbf{U}_p \vec{S} \mathbf{U}_p, \quad (186a)$$

where

$$\mathbf{U}_p = \sigma_1 \cdot \hat{p} \sigma_2 \cdot \hat{p}, \quad (186b)$$

and σ_i is the spin of the i th nucleon and \hat{p} is the unit relative momentum since we have assumed that the total momentum is zero.

Clearly \mathbf{U}_p does not change J, M, T, T_z . Just as for spin, for $\tilde{S}=0$ the basis states will have $\tilde{L}=J$, whereas for $\tilde{S}=1$, $\tilde{L}=J, J-1, J+1$. Also $\tilde{L}+\tilde{S}+T$ must be odd. Since the operator \mathbf{U}_p is symmetric in the particle number, the states with $\tilde{S}+\tilde{L}$ odd (even) are a linear combination with states with $S+L$ odd (even). By the same token, \mathbf{U}_p does not change parity which means it does not mix even and odd L . Therefore that means that states with different spin, S , do not mix and $\tilde{S}=S$.

Therefore the transformation from the spin basis to the pseudospin (\tilde{S})-pseudo-orbital angular momentum (\tilde{L}) basis will be given by

$$M^{(J)} = \langle \tilde{f}_L, \tilde{L}, \tilde{S}, J, M, T, T_z | \mathbf{U}_p | f_L, L, S, J, M, T, T_z \rangle \quad (187)$$

which will be a four by four matrix for each J since $(\tilde{L}, \tilde{S}), (L, S) = (J, 0), (J, 1), (J-1, 1), (J+1, 1)$. Evaluation of these matrix elements gives [165]

$$M^{(J)} = \begin{pmatrix} -1 & 0 & 0 & 0 \\ 0 & 1 & 0 & 0 \\ 0 & 0 & \frac{1}{N_J} & \frac{\sqrt{N_J^2-1}}{N_J} \\ 0 & 0 & \frac{\sqrt{N_J^2-1}}{N_J} & -\frac{1}{N_J} \end{pmatrix}, \quad (188)$$

where $N_J = 2J+1$.

A simple calculation shows that M is orthogonal, $\sum_{L,S} M_{\tilde{L}', \tilde{S}', L, S}^{(J)} M_{L, S, \tilde{L}, \tilde{S}}^{(J)} = \delta_{\tilde{L}, \tilde{L}'} \delta_{\tilde{S}, \tilde{S}'}$.

16.2. Scattering matrix in the spin representation

For $S=0$ clearly $L=J$. There can be no mixing between $S=0$ and 1 for $L=J$ because these states have different isospin. There can be no mixing between $L=J$ and $J \pm 1$ for $S=1$ because these states have different parity and different isospin. Using the standard parametrization of the scattering

matrix [166,167] we have

$$S^{(1,J)} = \begin{pmatrix} e^{2i\delta_{0,J,J}} & 0 & 0 & 0 \\ 0 & e^{2i\delta_{1,J,J}} & 0 & 0 \\ 0 & 0 & e^{2i\delta_{1,J-1,J}} \cos(2\epsilon_J) & ie^{i\delta_J^{(+)}} \sin(2\epsilon_J) \\ 0 & 0 & ie^{i\delta_J^{(+)}} \sin(2\epsilon_J) & e^{2i\delta_{1,J+1,J}} \cos(2\epsilon_J) \end{pmatrix}, \quad (189)$$

where $\delta_J^{(\pm)} = (\delta_{1,J-1,J} \pm \delta_{1,J+1,J})$, $\delta_{S,L,J}$ is the phase shift, and ϵ_J is the mixing angle.

What conditions do spin symmetry and orbital angular momentum symmetry impose on the scattering matrix? The conditions depend on whether the symmetry is an invariant symmetry or a dynamical symmetry. An invariant symmetry is the most restrictive because the generators commute with the Hamiltonian. A dynamical symmetry requires only that the representations of the symmetry not be admixed. For example, a spin–orbit interaction, $\vec{S} \cdot \vec{L}$, will conserve spin and orbital angular momentum quantum numbers, but the generators will not commute with it so it will lead to a dynamical symmetry rather than an invariant symmetry.

As we have seen already, total angular momentum plus isospin conservation imply no mixing of spin and no mixing of orbital angular momentum $L = J$ with $L = J \pm 1$. Clearly, the condition for orbital angular momentum conservation of either an invariant or dynamical symmetry is that there be no mixing between $L = J \pm 1$ and therefore

$$\epsilon_J = 0. \quad (190)$$

The condition for spin and angular momentum invariance implies additional restrictions on the phase shifts. These conditions are that the phase shifts are independent of the orientation of the spin with respect to the orbital angular momentum:

$$\delta_{1,L,J} = \delta_{1,L,J+1} = \delta_{1,L,J-1}. \quad (191)$$

However, if for example the Hamiltonian had a spin–orbit interaction, $\hat{S} \cdot \hat{L}$, the Hamiltonian will conserve spin and orbital angular momentum, but the phase shifts will not be equal. Therefore Eq. (191) is a test of an invariant spin symmetry.

16.3. Scattering matrix in the pseudospin representation

The same restrictions hold for pseudospin and pseudo-orbital angular momentum as spin and orbital angular momentum and the scattering matrix is

$$\tilde{S}^{(J)} = \begin{pmatrix} e^{2i\tilde{\delta}_{0,J,J}} & 0 & 0 & 0 \\ 0 & e^{2i\tilde{\delta}_{1,J,J}} & 0 & 0 \\ 0 & 0 & e^{2i\tilde{\delta}_{1,J-1,J}} \cos(2\epsilon_J) & ie^{i\tilde{\delta}_J^{(+)}} \sin(2\epsilon_J) \\ 0 & 0 & ie^{i\tilde{\delta}_J^{(+)}} \sin(2\epsilon_J) & e^{2i\tilde{\delta}_{1,J+1,J}} \cos(2\epsilon_J) \end{pmatrix}. \quad (192)$$

Likewise the condition for pseudo-orbital angular momentum conservation is

$$\tilde{\epsilon}_J = 0 \quad (193)$$

and the condition for pseudospin and pseudo-orbital angular momentum invariance is

$$\tilde{\delta}_{1,\tilde{L},J} = \tilde{\delta}_{1,\tilde{L},J+1} = \tilde{\delta}_{1,\tilde{L},J-1}. \quad (194)$$

Table 8

$T = 0$ pseudospin phase shifts $\tilde{\delta}_{1,\tilde{L},J}$ and mixing angles $\tilde{\epsilon}_J$ both in degrees as a function of the kinetic energy

$K.E.$ (MeV)	$\tilde{\delta}_{1,0,1}$ (deg)	$\tilde{\delta}_{1,2,1}$ (deg)	$\tilde{\epsilon}_1$ (deg)	$\tilde{\delta}_{1,2,3}$ (deg)	$\tilde{\delta}_{1,4,3}$ (deg)	$\tilde{\epsilon}_3$ (deg)	$\tilde{\delta}_{1,4,5}$ (deg)	$\tilde{\delta}_{1,6,5}$ (deg)	$\tilde{\epsilon}_5$ (deg)	$\tilde{\delta}_{1,6,7}$ (deg)	$\tilde{\delta}_{1,8,7}$ (deg)	$\tilde{\epsilon}_7$ (deg)
0.0	0.0	180	0.0	0.0	0.0	0.0	0.0	0.0	0.0	0.0	0.0	0.0
50	−3.058	59.392	20.000	0.206	−0.141	1.617	0.014	−0.086	0.198	0.001	−0.010	0.028
100	−7.514	38.506	17.778	0.101	0.422	3.665	0.006	−0.292	0.697	0.000	−0.062	0.161
150	−11.334	25.570	16.127	−0.275	1.273	5.238	−0.050	−0.467	1.231	−0.013	−0.140	0.350
200	−14.371	15.874	14.809	−0.767	1.977	6.374	−0.141	−0.566	1.730	−0.037	−0.226	0.554
250	−16.772	7.945	13.675	−1.284	2.385	7.172	−0.252	−0.586	2.182	−0.071	−0.309	0.759
300	−18.641	1.104	12.647	−1.772	2.493	7.726	−0.375	−0.538	2.586	−0.112	−0.382	0.954
350	−20.036	−5.036	11.677	−2.202	2.357	8.111	−0.501	−0.434	2.946	−0.157	−0.444	1.140

However, if for example the Hamiltonian had a pseudospin–pseudo-orbit interaction, $\vec{\tilde{S}} \cdot \vec{\tilde{L}}$, the Hamiltonian will conserve spin and orbital angular momentum, but the phase shifts will not be equal. Therefore Eq. (194) is a test of an invariant pseudospin symmetry.

In order to determine the pseudo phase shifts in terms of the phase shifts we use the fact that $\tilde{S}^{(J)} = M^{(J)} S^{(J)} M^{(J)}$. This gives

$$\tilde{\delta}_{S,J,J} = \delta_{S,J,J} , \quad (195)$$

$$\tilde{\delta}_J^{(+)} = \delta_J^{(+)} , \quad (196)$$

$$\cos(\tilde{\delta}_J^{(-)}) \cos(2\tilde{\epsilon}_J) = \cos(\delta_J^{(-)}) \cos(2\epsilon_J) , \quad (197)$$

$$\tan(\tilde{\delta}_J^{(-)}) = \frac{2\sqrt{N_J^2 - 1} \sin(2\epsilon_J) - (N_J^2 - 2) \sin(\delta_J^{(-)}) \cos(2\epsilon_J)}{N_J^2 \cos(\delta_J^{(-)}) \cos(2\epsilon_J)} , \quad (198)$$

$$\sin(2\tilde{\epsilon}_J) = \frac{2\sqrt{N_J^2 - 1} \sin(\delta_J^{(-)}) \cos(2\epsilon_J) + (N_J^2 - 2) \sin(2\epsilon_J)}{N_J^2} . \quad (199)$$

16.4. Test of spin and pseudospin conservation

We use the compilation on NN-Online [168,167], which tabulates measured phase shifts and mixing angles in the spin representation for angular momentum up to $J = 8$ and kinetic energy up to 350 MeV, to calculate the pseudospin phase shifts and mixing angles from Eqs. (195)–(199). Because Eq. (195) states that the spin and pseudospin phase shifts with $\tilde{L} = L = J$ are equal we need only calculate the pseudospin scattering matrix for $\tilde{L} = J \pm 1$. These calculated pseudospin phase shifts and mixing angles as a function of the kinetic energy ($K.E.$) using the plane wave analysis (PW) are tabulated in Tables 8 and 9.

An analysis of the phase shifts shows [165] that the largest violations of the conditions in Eqs. (191) and (194) for the $T = 0$ are for $L = \tilde{L} = 2$. The spin violations are smaller than the pseudospin violations for small kinetic energy, but for larger kinetic energy the pseudospin differences are smaller, except for $L = \tilde{L} = 2$. As L and \tilde{L} increase the violations decrease until they are very small indeed but pseudospin

Table 9

$T = 1$ pseudospin phase shifts $\tilde{\delta}_{1,\tilde{L},J}$ and mixing angles $\tilde{\epsilon}_J$ both in degrees as a function of the kinetic energy

$K, E.$ (MeV)	$\tilde{\delta}_{1,1,2}$ (deg)	$\tilde{\delta}_{1,3,2}$ (deg)	$\tilde{\epsilon}_2$ (deg)	$\tilde{\delta}_{1,3,4}$ (deg)	$\tilde{\delta}_{1,5,4}$ (deg)	$\tilde{\epsilon}_4$ (deg)	$\tilde{\delta}_{1,5,6}$ (deg)	$\tilde{\delta}_{1,7,6}$ (deg)	$\tilde{\epsilon}_6$ (deg)	$\tilde{\delta}_{1,7,8}$ (deg)	$\tilde{\delta}_{1,9,8}$ (deg)	$\tilde{\epsilon}_8$ (deg)
0.0	0.0	0.0	0.0	0.0	0.0	0.0	0.0	0.0	0.0	0.0	0.0	0.0
50	−0.111	6.300	−0.408	−0.016	0.134	−0.155	−0.006	0.013	−0.018	−0.000	0.001	−0.003
100	0.162	11.538	−0.389	−0.012	0.555	−0.438	−0.021	0.068	−0.090	−0.000	0.008	−0.022
150	0.539	14.422	−0.112	0.021	1.158	−0.684	−0.025	0.147	−0.184	0.001	0.022	−0.055
200	0.842	15.941	0.249	0.074	1.842	−0.875	−0.009	0.233	−0.285	0.005	0.042	−0.096
250	0.982	16.758	0.612	0.137	2.516	−1.019	0.028	0.323	−0.386	0.010	0.067	−0.140
300	0.925	17.223	0.928	0.200	3.097	−1.126	0.084	0.413	−0.486	0.017	0.096	−0.184
350	0.676	17.508	1.169	0.255	3.517	−1.205	0.157	0.501	−0.583	0.025	0.129	−0.226

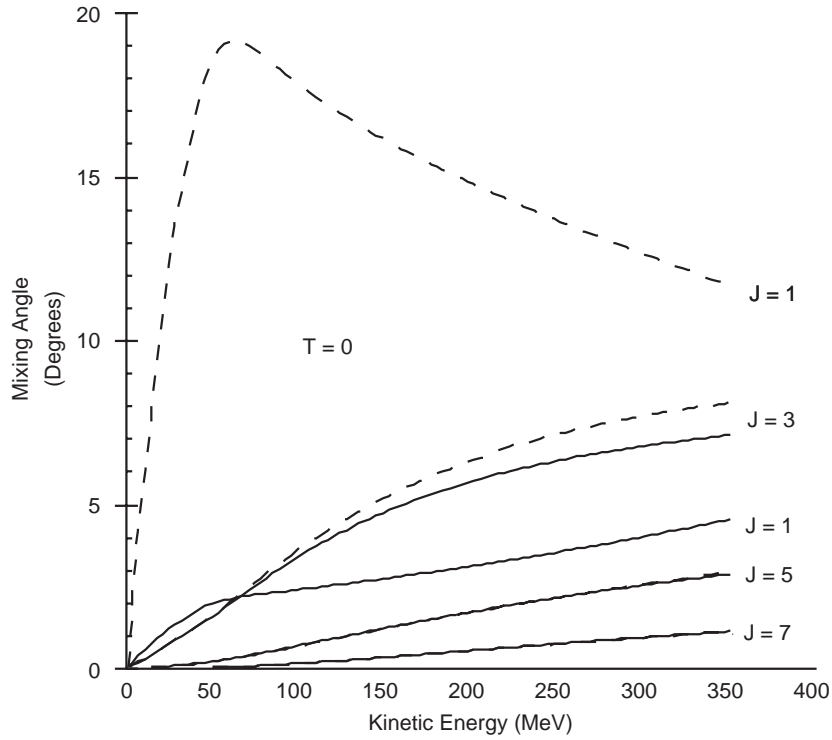


Fig. 43. The $T = 0$ mixing angles ϵ_J (solid line) and $\tilde{\epsilon}_J$ (dashed line) as a function of kinetic energy and angular momentum J .

is no better conserved than spin. For the $T = 1$, the spin phase violations are smaller than the pseudospin phase violations as a function of kinetic energy, except for $L = \tilde{L} = 1$. As L and \tilde{L} increase the violations decrease until they are very small indeed but pseudospin is no better conserved than spin. Therefore neither spin nor pseudospin is an invariant symmetry.

In Figs. 43 and 44 the mixing angles ϵ_J and $\tilde{\epsilon}_J$ are plotted for $T = 0$ and 1, respectively. For $T = 0$ the pseudo-orbital angular momentum mixing angles are larger than orbital angular momentum mixing

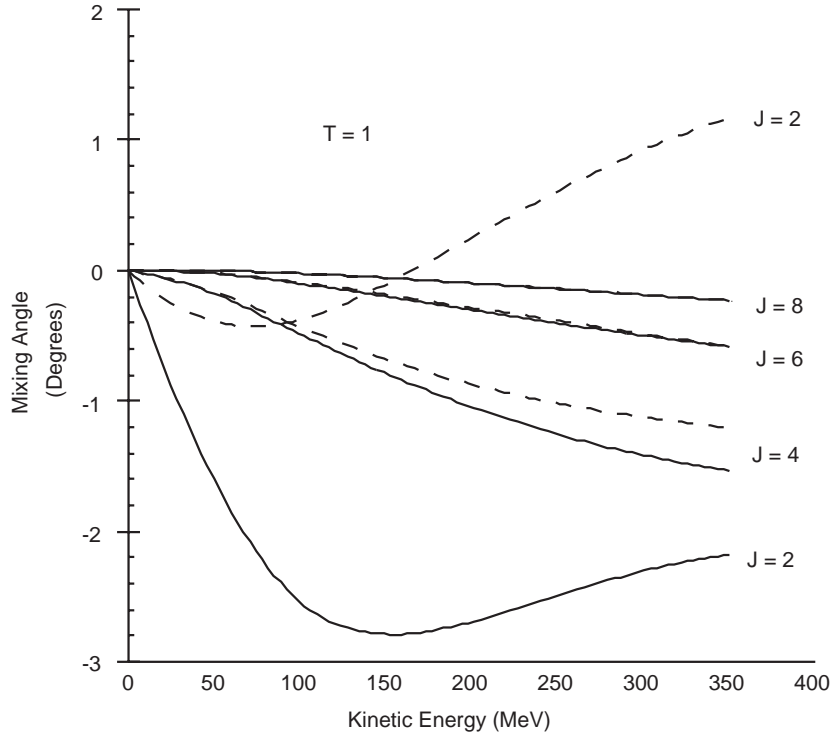


Fig. 44. The $T = 1$ mixing angles ϵ_J (solid line) and $\tilde{\epsilon}_J$ (dashed line) as a function of kinetic energy and angular momentum J .

angles for low total angular momentum, but the mixing angles become identical for large total angular momentum J , while for $T = 1$ the orbital angular momentum mixing angles are larger than the pseudo-orbital angular momentum mixing angles for low total angular momentum, but become identical for large total angular momentum J . The mixing angles for $T = 1$ are generally smaller than for $T = 0$.

These results suggest that the pseudospin symmetry generated by operators in Eq. (52) is neither an invariant symmetry nor a dynamic symmetry of the nucleon–nucleon interaction.

16.5. Summary and conclusions

Spin (pseudospin) invariance implies the phase shifts for a given orbital angular momentum (pseudo-orbital angular momentum) L (\tilde{L}) should be independent of the total angular momentum J . There are substantial differences between the phase shifts for low orbital angular momentum and pseudo-orbital angular momentum but these differences decrease as the orbital angular momentum and pseudo-orbital angular momentum increases. The phase differences show that neither spin or pseudospin is an invariant symmetry but there is the possibility that one or/and the other may be a dynamical symmetry since dynamical symmetry does not demand that the phase shifts for a given L or \tilde{L} and different J be identical.

On the other hand the non-zero mixing angles imply that orbital angular momentum and pseudo-orbital angular momentum breaking is neither an invariant symmetry nor a dynamical symmetry. However the mixing angles are not large for the energies measured except for $T = 0$, $J = 1$ in the pseudospin

representation. The symmetry breaking is more substantial for the $T = 0$ states than for the $T = 1$ states and in both cases the symmetry breaking decreases as J increases. Furthermore, the pseudospin mixing angles are less than the spin mixing angles for $T = 1$ which suggests that pseudospin may improve as the neutron excess increases which is consistent with systematic studies in nuclei [118,120,121].

In summary although pseudospin symmetry is favored over spin symmetry for the $T = 1$ part of the nucleon–nucleon interaction there are no dramatic differences between spin and pseudospin breaking in nucleon–nucleon scattering.

17. Summary and future

We have reviewed the theoretical and empirical evidence for relativistic pseudospin symmetry in nuclei and spin symmetry in hadrons. Small energy splittings between pseudospin doublets are measured in nuclei and calculated in the relativistic mean field approximation. These same relativistic mean field calculations show that the scalar and vector potentials approximately satisfy the conditions for pseudospin symmetry and their eigenfunctions approximately satisfy the conditions imposed by pseudospin symmetry. Pseudospin symmetry conservation increases as the binding energy decreases and as the pseudo-orbital angular momentum decreases. Pseudospin symmetry predicts the small magnetic dipole transitions measured between the states in the doublets very well for ^{39}Ca and quite well throughout the nuclear table. The Gamow–Teller transition $^{39}\text{Ca} \rightarrow ^{39}\text{K}$ is predicted well but empirical tests throughout the nuclei chart have yet to be carried out. Approximate pseudospin symmetry predictions for quadrupole transitions are remarkably well obeyed.

Expectations are that the pseudospin symmetry will improve for the neutron orbitals in neutron rich nuclei and for the proton orbitals in proton rich nuclei. Such nuclei shall be produced in rare isotope accelerators.

For nucleon scattering from nuclei the pseudospin conservation increases with the kinetic energy. Also neutron scattering from nuclei should show better pseudospin conservation than proton scattering from nuclei at comparable energies.

Pseudospin symmetry in nuclei predicts spin symmetry for anti-nucleons in a nuclear environment. A limited amount of data on polarized anti-nucleon scattering from nuclei supports this conclusion. Perhaps more data will become available as more intense anti-nucleon beams are produced.

18. Future—beyond the mean field

The fact that nuclei, which are dominantly non-relativistic, have a relativistic symmetry is reminiscent of Alice in Wonderland. In her journey through Wonderland, Alice encounters a cat with a grin which she finds curious. While conversing with the cat, the cat slowly disappears except for its smile as in Fig. 45. “Well! I’ve often seen a cat without a grin,” thought Alice, “but a grin without a cat! It’s the most curious thing I ever saw in all my life!” [169]. Relativistic dynamics in nuclei is like the cat whereas pseudospin symmetry is like the grin and to have one without the other is indeed curious. Even more curiouser is the fact that the conditions for pseudospin symmetry have origins in QCD. This situation implies that there is a fundamental rationale for pseudospin symmetry. For that reason we investigated pseudospin conservation in nucleon–nucleon scattering. We found that pseudospin symmetry is an approximate dynamic symmetry in the isospin one channel and less so in the isospin zero channel. However, a more generalized pseudospin

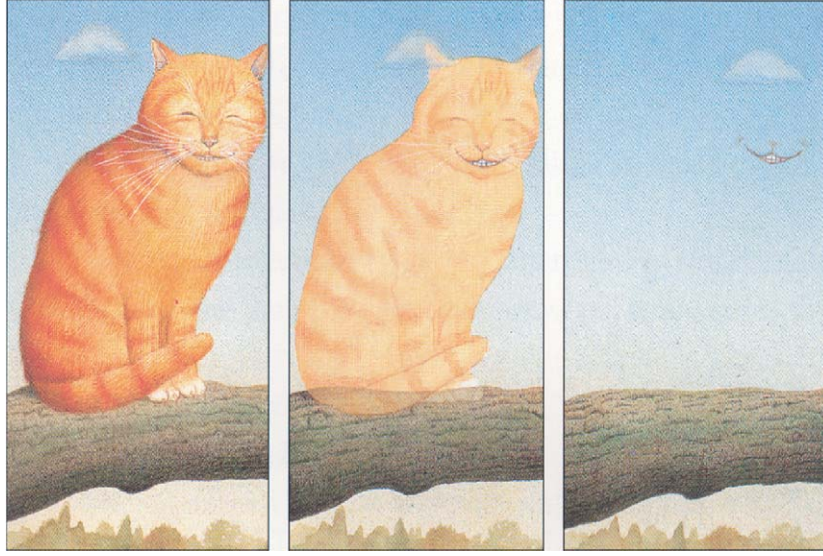


Fig. 45. “Well! I’ve often seen a cat without a grin,” thought Alice, “but a grin without a cat! It’s the most curious thing I ever saw in all my life!” [169].

symmetry with generators given in Eq. (14), which reduces to pseudospin symmetry in the mean field approximation, may be conserved in nucleon–nucleon scattering and is currently being investigated. Hence, the final conclusion on an approximate symmetry for the nucleon–nucleon interaction is still to be rendered.

Although we have restricted ourselves to spin symmetry in heavy mesons, small spin orbit splittings are observed in baryons as well. This prevalence of spin symmetry needs to be investigated more deeply. One puzzle is: Why do hadrons exhibit spin symmetry while nuclei exhibit pseudospin symmetry?

19. Appendices

19.1. Orthogonal transformation in four dimensions

The orthogonal transformation of the four vector (β, α_i) , O , is the product of a rotation in four Euclidean dimensions, R , and a discrete reflection in this space, Π ,

$$O = R\Pi . \quad (200)$$

A rotation group in four dimensions is isomorphic to the $SU(2) \times SU(2)$ group. For the Dirac matrices the generators of these rotations are

$$K_i = \frac{\Sigma_i + i\gamma_i}{4}, \quad P_i = \frac{\Sigma_i - i\gamma_i}{4}, \quad (201)$$

with commutation relations,

$$[K_i, K_j] = i\epsilon_{ijk} K_k, \quad [P_i, P_j] = i\epsilon_{ijk} P_k, \quad [K_i, P_j] = 0 . \quad (202)$$

In terms of $SU(2) \times SU(2)$ the four vector (β, α_i) transforms like a double spinor

$$\begin{aligned} T_{1/2,1/2} &= -(\alpha_x + i\alpha_y), & T_{1/2,-1/2} &= (\alpha_z + i\beta), & T_{-1/2,1/2} &= (\alpha_z - i\beta), \\ T_{-1/2,-1/2} &= (\alpha_x - i\alpha_y). \end{aligned} \quad (203)$$

Thus the transformation matrix for $T, T' = \tilde{R}TR$,

$$T'_{\mu,\mu'} = \mathcal{D}_{\mu,v}^{(1/2)}(\phi_K, \theta_K, \psi_K) \mathcal{D}_{\mu',v'}^{(1/2)}(\phi_P, \theta_P, \psi_P) T_{v,v'}. \quad (204)$$

where $\phi_K, \theta_K, \psi_K, \phi_P, \theta_P, \psi_P$ are the Euler angles for the rotations generated by K_i and P_i , respectively, and $\mathcal{D}_{\mu,v}^{(1/2)}(\phi_K, \theta_K, \psi_K)$ are the Wigner D-functions [170]. Transforming to the original basis we can determine the matrix elements $e_{\mu,v}$ in Section 2 in terms of the Euler angles where $\mu, v = 0, 1, 2, 3$:

$$e_{0,0} = \cos \left[\frac{\theta_K}{2} \right] \cos \left[\frac{\theta_P}{2} \right] \cos [\Delta_7] + \cos [\Delta_8] \sin \left[\frac{\theta_K}{2} \right] \sin \left[\frac{\theta_P}{2} \right], \quad (205a)$$

$$e_{0,1} = -\cos \left[\frac{\theta_P}{2} \right] \sin \left[\frac{\theta_K}{2} \right] \sin [\Delta_6] - \cos \left[\frac{\theta_K}{2} \right] \sin \left[\frac{\theta_P}{2} \right] \sin [\Delta_5], \quad (205b)$$

$$e_{0,2} = \cos \left[\frac{\theta_P}{2} \right] \cos [\Delta_6] \sin \left[\frac{\theta_K}{2} \right] - \cos \left[\frac{\theta_K}{2} \right] \cos [\Delta_5] \sin \left[\frac{\theta_P}{2} \right], \quad (205c)$$

$$e_{0,3} = \cos \left[\frac{\theta_K}{2} \right] \cos \left[\frac{\theta_P}{2} \right] \sin [\Delta_7] - \sin \left[\frac{\theta_K}{2} \right] \sin \left[\frac{\theta_P}{2} \right] \sin [\Delta_8], \quad (205d)$$

$$e_{1,0} = -\cos \left[\frac{\theta_K}{2} \right] \sin \left[\frac{\theta_P}{2} \right] \sin [\Delta_3] + \cos \left[\frac{\theta_P}{2} \right] \sin \left[\frac{\theta_K}{2} \right] \sin [\Delta_4], \quad (205e)$$

$$e_{1,1} = \cos \left[\frac{\theta_K}{2} \right] \cos \left[\frac{\theta_P}{2} \right] \cos [\Delta_1] - \cos [\Delta_2] \sin \left[\frac{\theta_K}{2} \right] \sin \left[\frac{\theta_P}{2} \right], \quad (205f)$$

$$e_{1,2} = -\sin \left[\frac{\theta_K}{2} \right] \sin \left[\frac{\theta_P}{2} \right] \sin [\Delta_2] - \cos \left[\frac{\theta_K}{2} \right] \cos \left[\frac{\theta_P}{2} \right] \sin [\Delta_1], \quad (205g)$$

$$e_{1,3} = \cos \left[\frac{\theta_P}{2} \right] \cos [\Delta_4] \sin \left[\frac{\theta_K}{2} \right] + \cos \left[\frac{\theta_K}{2} \right] \cos [\Delta_3] \sin \left[\frac{\theta_P}{2} \right], \quad (205h)$$

$$e_{2,0} = -\cos \left[\frac{\theta_P}{2} \right] \cos [\Delta_4] \sin \left[\frac{\theta_K}{2} \right] + \cos \left[\frac{\theta_K}{2} \right] \cos [\Delta_3] \sin \left[\frac{\theta_P}{2} \right], \quad (205i)$$

$$e_{2,1} = -\sin \left[\frac{\theta_K}{2} \right] \sin \left[\frac{\theta_P}{2} \right] \sin [\Delta_2] + \cos \left[\frac{\theta_K}{2} \right] \cos \left[\frac{\theta_P}{2} \right] \sin [\Delta_1], \quad (205j)$$

$$e_{2,2} = \cos \left[\frac{\theta_K}{2} \right] \cos \left[\frac{\theta_P}{2} \right] \cos [\Delta_1] + \cos [\Delta_2] \sin \left[\frac{\theta_K}{2} \right] \sin \left[\frac{\theta_P}{2} \right], \quad (205k)$$

$$e_{2,3} = \cos \left[\frac{\theta_K}{2} \right] \sin \left[\frac{\theta_P}{2} \right] \sin [\Delta_3] + \cos \left[\frac{\theta_P}{2} \right] \sin \left[\frac{\theta_K}{2} \right] \sin [\Delta_4], \quad (206a)$$

$$e_{3,0} = -\cos\left[\frac{\theta_K}{2}\right] \cos\left[\frac{\theta_P}{2}\right] \sin[\Delta_7] - \sin\left[\frac{\theta_K}{2}\right] \sin\left[\frac{\theta_P}{2}\right] \sin[\Delta_8] , \quad (206b)$$

$$e_{3,1} = -\cos\left[\frac{\theta_P}{2}\right] \cos[\Delta_6] \sin\left[\frac{\theta_K}{2}\right] - \cos\left[\frac{\theta_K}{2}\right] \cos[\Delta_5] \sin\left[\frac{\theta_P}{2}\right] , \quad (206c)$$

$$e_{3,2} = -\cos\left[\frac{\theta_P}{2}\right] \sin\left[\frac{\theta_K}{2}\right] \sin[\Delta_6] + \cos\left[\frac{\theta_K}{2}\right] \sin\left[\frac{\theta_P}{2}\right] \sin[\Delta_5] , \quad (206d)$$

$$e_{3,3} = \cos\left[\frac{\theta_K}{2}\right] \cos\left[\frac{\theta_P}{2}\right] \cos[\Delta_7] - \cos[\Delta_8] \sin\left[\frac{\theta_K}{2}\right] \sin\left[\frac{\theta_P}{2}\right] . \quad (206e)$$

The phases Δ_i ,

$$\Delta_1 = \frac{1}{2}(\phi_K + \phi_P + \psi_K + \psi_P), \quad \Delta_2 = \frac{1}{2}(\phi_K + \phi_P - \psi_K - \psi_P) , \quad (207a)$$

$$\Delta_3 = \frac{1}{2}(\phi_K + \phi_P + \psi_K - \psi_P), \quad \Delta_4 = \frac{1}{2}(\phi_K + \phi_P - \psi_K + \psi_P) , \quad (207b)$$

$$\Delta_5 = \frac{1}{2}(\phi_K - \phi_P + \psi_K + \psi_P), \quad \Delta_6 = \frac{1}{2}(\phi_K - \phi_P - \psi_K - \psi_P) , \quad (207c)$$

$$\Delta_7 = \frac{1}{2}(\phi_K - \phi_P + \psi_K - \psi_P), \quad \Delta_8 = \frac{1}{2}(\phi_K - \phi_P - \psi_K + \psi_P) , \quad (207d)$$

are not all independent: $\Delta_1 + \Delta_2 = \Delta_3 + \Delta_4$, $\Delta_5 + \Delta_6 = \Delta_7 + \Delta_8$, $\Delta_1 - \Delta_2 = \Delta_5 - \Delta_6$, $\Delta_3 - \Delta_4 = \Delta_7 - \Delta_8$; only four are independent.

From Eq. (201) we readily see that Σ_i and γ_i are related to the generators K_i and P_i and transform like the six dimensional representation of the orthogonal group in four dimensions. In terms of $SU(2) \times SU(2)$ the generators transform like a vector–scalar

$$T_{i,0} = K_i, \quad T_{0,i} = P_i . \quad (208)$$

Thus the transformation matrix for T , $T' = \tilde{R} T R$

$$T'_{i',0} = \mathcal{D}_{i',i}^{(1)}(\phi_K, \theta_K, \psi_K) T_{i,0}, \quad T'_{0,i'} = \mathcal{D}_{i',i}^{(1)}(\phi_P, \theta_P, \psi_P) T_{0,i} . \quad (209)$$

With some algebra we obtain

$$\Sigma'_i = \mathcal{A}_{i,j} \Sigma_j + B_{i,j} \gamma_j , \quad (210a)$$

$$\gamma'_i = -B_{i,j} \Sigma_j + \mathcal{A}_{i,j} \gamma_j , \quad (210b)$$

where

$$\begin{aligned} \mathcal{A}_{1,1} = & \frac{\cos[\phi_K] \cos[\theta_K] \cos[\psi_K] + \cos[\phi_P] \cos[\theta_P] \cos[\psi_P]}{2} \\ & - \left(\frac{\sin[\phi_K] \sin[\psi_K] + \sin[\phi_P] \sin[\psi_P]}{2} \right) , \end{aligned} \quad (211a)$$

$$\begin{aligned} \mathcal{A}_{1,2} = & - \left(\frac{\cos[\phi_K] \cos[\theta_K] \sin[\psi_K] + \cos[\phi_P] \cos[\theta_P] \sin[\psi_P]}{2} \right) \\ & - \left(\frac{\cos[\psi_K] \sin[\phi_K] + \cos[\psi_P] \sin[\phi_P]}{2} \right) , \end{aligned} \quad (211b)$$

$$\mathcal{A}_{1,3} = \frac{\cos[\phi_K] \sin[\theta_K] + \cos[\phi_P] \sin[\theta_P]}{2}, \quad (211c)$$

$$\begin{aligned} \mathcal{A}_{2,1} = & \frac{\cos[\theta_K] \cos[\psi_K] \sin[\phi_K] + \cos[\theta_P] \cos[\psi_P] \sin[\phi_P]}{2} \\ & + \frac{\cos[\phi_K] \sin[\psi_K] + \cos[\phi_P] \sin[\psi_P]}{2}, \end{aligned} \quad (211d)$$

$$\begin{aligned} \mathcal{A}_{2,2} = & \frac{\cos[\phi_K] \cos[\psi_K] + \cos[\phi_P] \cos[\psi_P] - \cos[\theta_K] \sin[\phi_K] \sin[\psi_K]}{2} \\ & - \frac{\cos[\theta_P] \sin[\phi_P] \sin[\psi_P]}{2}, \end{aligned} \quad (211e)$$

$$\mathcal{A}_{2,3} = \frac{\sin[\phi_K] \sin[\theta_K] + \sin[\phi_P] \sin[\theta_P]}{2}, \quad (211f)$$

$$\mathcal{A}_{3,1} = - \left(\frac{\cos[\psi_K] \sin[\theta_K] + \cos[\psi_P] \sin[\theta_P]}{2} \right), \quad (211g)$$

$$\mathcal{A}_{3,2} = \frac{\sin[\theta_K] \sin[\psi_K] + \sin[\theta_P] \sin[\psi_P]}{2}, \quad (211h)$$

$$\mathcal{A}_{3,3} = \frac{\cos[\theta_K] + \cos[\theta_P]}{2}, \quad (211i)$$

$$\begin{aligned} \mathcal{B}_{1,1} = & \frac{\cos[\phi_K] \cos[\theta_K] \cos[\psi_K] - \cos[\phi_P] \cos[\theta_P] \cos[\psi_P]}{2} \\ & + \left(\frac{-\sin[\phi_K] \sin[\psi_K] + \sin[\phi_P] \sin[\psi_P]}{2} \right), \end{aligned} \quad (212a)$$

$$\begin{aligned} \mathcal{B}_{1,2} = & \frac{-\cos[\psi_K] \sin[\phi_K] + \cos[\psi_P] \sin[\phi_P] - \cos[\phi_K] \cos[\theta_K] \sin[\psi_K]}{2} \\ & + \frac{\cos[\phi_P] \cos[\theta_P] \sin[\psi_P]}{2}, \end{aligned} \quad (212b)$$

$$\mathcal{B}_{1,3} = \frac{\cos[\phi_K] \sin[\theta_K] - \cos[\phi_P] \sin[\theta_P]}{2}, \quad (212c)$$

$$\begin{aligned} \mathcal{B}_{2,1} = & \frac{\cos[\theta_K] \cos[\psi_K] \sin[\phi_K] - \cos[\theta_P] \cos[\psi_P] \sin[\phi_P]}{2} \\ & + \frac{\cos[\phi_K] \sin[\psi_K] - \cos[\phi_P] \sin[\psi_P]}{2}, \end{aligned} \quad (212d)$$

$$\begin{aligned} \mathcal{B}_{2,2} = & \frac{\cos[\phi_K] \cos[\psi_K] - \cos[\phi_P] \cos[\psi_P] - \cos[\theta_K] \sin[\phi_K] \sin[\psi_K]}{2} \\ & + \frac{\cos[\theta_P] \sin[\phi_P] \sin[\psi_P]}{2}, \end{aligned} \quad (212e)$$

$$\mathcal{B}_{2,3} = \frac{\sin[\phi_K] \sin[\theta_K] - \sin[\phi_P] \sin[\theta_P]}{2}, \quad (212f)$$

$$\mathcal{B}_{3,1} = - \left(\frac{\cos[\psi_K] \sin[\theta_K] - \cos[\psi_P] \sin[\theta_P]}{2} \right) , \quad (212g)$$

$$\mathcal{B}_{3,2} = \frac{\sin[\theta_K] \sin[\psi_K] - \sin[\theta_P] \sin[\psi_P]}{2} , \quad (212h)$$

$$\mathcal{B}_{3,3} = \frac{\cos[\theta_K] - \cos[\theta_P]}{2} . \quad (212i)$$

In order to preserve the anticommutation and commutation relations in Eqs. (10) and (11), these matrices satisfy:

$$\mathcal{A}\tilde{\mathcal{A}} + \mathcal{B}\tilde{\mathcal{B}} = 1, \quad \mathcal{A}\tilde{\mathcal{B}} + \mathcal{B}\tilde{\mathcal{A}} = 0 , \quad (213a)$$

$$\sum_{j,l} \epsilon_{jlm} [\mathcal{A}_{i,j} \mathcal{A}_{k,l} + \mathcal{B}_{i,j} \mathcal{B}_{k,l}] = \epsilon_{ikp} \mathcal{A}_{p,m} , \quad (213b)$$

$$\sum_{j,l} \epsilon_{jlm} [\mathcal{A}_{i,j} \mathcal{B}_{k,l} + \mathcal{B}_{i,j} \mathcal{A}_{k,l}] = \epsilon_{ikp} \mathcal{B}_{p,m} . \quad (213c)$$

The most general transformation of the orthogonal group in four dimensions for the four dimensional representation and the six dimensional representation are given in Eqs. (204)–(207) and Eqs. (209)–(212), respectively, for no discrete reflection, $\Pi = \text{unity}$. There is only one independent reflection,

$$\Pi = \begin{pmatrix} -1 & 0 & 0 & 0 \\ 0 & 1 & 0 & 0 \\ 0 & 0 & 1 & 0 \\ 0 & 0 & 0 & 1 \end{pmatrix} . \quad (214)$$

The four dimensional representation which includes this reflection is obtained by $e_{i,0} \rightarrow -e_{i,0}$. The six dimensional representation including the reflection is given by $\Sigma_i \rightarrow -\Sigma_i$ in Eq. (210).

19.2. Invariant symmetry

In order to prove that the generators S'_i in Eq. (14) satisfy SU(2) commutation relations, we note that $\beta' \beta' = 1$ follows from the anticommutation rules given in Eq. (10) and thus

$$(1 + \beta')(1 + \beta') = (1 - \beta')(1 - \beta') = 2 , \quad (215a)$$

$$(1 + \beta')(1 - \beta') = 0 . \quad (215b)$$

Furthermore,

$$\vec{\Sigma}' \cdot \vec{p}' \vec{\Sigma}' \cdot \vec{p}' = \vec{p}' \cdot \vec{p}' . \quad (216)$$

Since β' commutes with Σ'_i (see Eq. (11)) and p' , the commutation relation reduces to

$$[S'_i, S'_j] = \frac{1}{8} \left\{ [\Sigma'_i, \Sigma'_j] (1 + \beta') + \frac{1}{\vec{p}' \cdot \vec{p}'} \vec{\Sigma}' \cdot \vec{p}' [\Sigma'_i, \Sigma'_j] \vec{\Sigma}' \cdot \vec{p}' (1 - \beta') \right\} \quad (217)$$

which gives Eq. (15a) after using Eq. (11).

As for Eq. (15b), using Eqs. (215)–(216)

$$[S'_i, H_{\text{BR}}] = \frac{c}{4} \left\{ \Sigma'_i (1 + \beta') \vec{\alpha}' \cdot \vec{p}' - \vec{\alpha}' \cdot \vec{p}' \Sigma'_i (1 + \beta') \right. \\ \left. + \frac{1}{\vec{p}' \cdot \vec{p}'} [\vec{\Sigma}' \cdot \vec{p}' S'_i \vec{\Sigma}' \cdot \vec{p}' (1 - \beta') \vec{\alpha}' \cdot \vec{p}' \right. \\ \left. - \vec{\alpha}' \cdot \vec{p}' \vec{\Sigma}' \cdot \vec{p}' S'_i \vec{\Sigma}' \cdot \vec{p}' (1 - \beta')] \right\}. \quad (218)$$

Using the relations

$$\alpha'_i = \gamma'_5 \Sigma'_i = \Sigma'_i \gamma'_5, \quad (219a)$$

$$x[\gamma'_5, \Sigma'_i] = 0, \quad \{\gamma'_5, \beta'\} = 0, \quad (219b)$$

where γ'_5 is the transformed $\gamma_5 = \begin{pmatrix} 0 & 1 \\ 1 & 0 \end{pmatrix}$, the right-hand side of Eq. (218) vanishes thus giving Eq. (15b).

19.3. Spherical amplitudes

We shall in fact go backwards in our proof. In the two column form in Eq. (50) clearly $g_{n_r, \ell}(r)[Y^{(\ell)}(\theta, \phi)\chi_M^{(j)}]$ is an eigenfunction of $\vec{j} \cdot \vec{j}$, $\vec{\ell} \cdot \vec{\ell}$, and j_z . We expand the lower component into momentum space,

$$f_{n_r, \ell, j}(r)[Y^{(\ell_j)}(\theta, \phi)\chi_M^{(j)}] = \int_0^\infty e^{i\vec{q} \cdot \vec{r}} \tilde{f}_{n_r, \ell, j}(q)[Y^{(\ell_j)}(\theta_q, \phi_q)\chi_M^{(j)}] d\vec{q}. \quad (220)$$

Then $\vec{\ell} \cdot \vec{\ell}$ operating on the lower component will give

$$\vec{\ell} \cdot \vec{\ell} f_{n_r, \ell, j}(r)[Y^{(\ell_j)}(\theta, \phi)\chi_M^{(j)}] = \int_0^\infty e^{i\vec{q} \cdot \vec{r}} \tilde{f}_{n_r, \ell, j}(q) \vec{\ell} \cdot \vec{\ell} [Y^{(\ell_j)}(\theta_q, \phi_q)\chi_M^{(j)}] d\vec{q} \\ = \int_0^\infty e^{i\vec{q} \cdot \vec{r}} \tilde{f}_{n_r, \ell, j}(q) \sigma \cdot \hat{q} \vec{\ell} \cdot \vec{\ell} \sigma \cdot \hat{q} [Y^{(\ell_j)}(\theta_q, \phi_q)\chi_M^{(j)}] d\vec{q}. \quad (221)$$

Using the relations,

$$\sigma \cdot \hat{q} [Y^{(\ell_j)}(\theta_q, \phi_q)\chi_M^{(j)}] = [Y^{(\ell)}(\theta_q, \phi_q)\chi_M^{(j)}], \\ \sigma \cdot \hat{q} [Y^{(\ell)}(\theta_q, \phi_q)\chi_M^{(j)}] = [Y^{(\ell_j)}(\theta_q, \phi_q)\chi_M^{(j)}], \quad (222)$$

we get

$$\vec{\ell} \cdot \vec{\ell} f_{n_r, \ell, j}(r)[Y^{(\ell_j)}(\theta, \phi)\chi_M^{(j)}] = \ell(\ell + 1) f_{n_r, \ell, j}(r)[Y^{(\ell_j)}(\theta, \phi)\chi_M^{(j)}], \quad (223)$$

satisfying Eq. (49) and proving that is the right form for the eigenfunctions coupled to definite J . The uncoupled eigenfunction will be just the inversion of Eq. (50); namely, $\Phi_{n_r, \ell, m, \mu, M}^s(\vec{r}) = \sum_{j, M} C_{m\mu M}^{\ell(1/2)j} \times$

$\Psi_{n_r, \ell, j, M}^s(\vec{r})$. The upper component is then given by Eq. (44) since a simple inversion is involved. However the lower component will have

$$\sum_{j, M} C_{m\mu M}^{\ell(1/2)j} C_{m'\mu' M}^{\ell_j(1/2)j}. \quad (224)$$

Using the expressions for the Clebsch–Gordan coefficients,

$$C_{m(1/2)M}^{\ell(1/2)\ell+1/2} = C_{m-(1/2)M}^{\ell(1/2)\ell-1/2} = \sqrt{\frac{\ell + \frac{1}{2} + M}{2\ell + 1}}, \quad (225a)$$

$$C_{m(1/2)M}^{\ell(1/2)\ell-1/2} = -C_{m-(1/2)M}^{\ell(1/2)\ell+1/2} = -\sqrt{\frac{\ell + \frac{1}{2} - M}{2\ell + 1}}, \quad (225b)$$

we end up with Eqs. (44) and (46).

Acknowledgements

The author would like to thank A. Leviatan for collaboration on many aspects of pseudospin symmetry. For collaboration on the first test of pseudospin symmetry in realistic relativistic eigenfunctions, the author thanks D.G. Madland. For collaboration on the global test of pseudospin symmetry in magnetic dipole transitions, the author thanks P. von Neumann-Cosel. For collaboration on spin symmetry in heavy mesons the author thanks T. Goldman and P. Page. For collaboration on pseudospin symmetry in realistic non-relativistic eigenfunctions, the author thanks P.J. Borycki, W. Nazarewicz, and M. Stoitsov. For collaboration on pseudospin symmetry in deformed nuclei, the author thanks J. Meng and S.-G. Zhou. Finally, the author thanks T. Bürvenich, T. Cohen, F. Goldhaber, H. Leeb, M. Malheiro, P. Ring, B. Serot, I. Talmi, I. Towner, D. Vretenar, and N. Walet for discussions. This research is supported by the U.S. Department of Energy under contract W-7405-ENG-36.

References

- [1] G.B. Smith, L.J. Tassie, *Ann. Phys.* 65 (1971) 352.
- [2] J.S. Bell, H. Ruegg, *Nucl. Phys. B* 98 (1975) 151.
- [3] P.R. Page, T. Goldman, J.N. Ginocchio, *Phys. Rev. Lett.* 86 (2001) 204.
- [4] A. Arima, M. Harvey, K. Shimizu, *Phys. Lett. B* 30 (1969) 517.
- [5] K.T. Hecht, A. Adler, *Nucl. Phys. A* 137 (1969) 129.
- [6] J.N. Ginocchio, *Phys. Rev. Lett.* 78 (1997) 436.
- [7] W. Greiner, B. Müller, J. Rafelski, *Quantum Electrodynamics of Strong Fields*, Springer-Verlag, New York, 1985.
- [8] A.L. Blokhin, C. Bahri, J.P. Draayer, *Phys. Rev. Lett.* 74 (1995) 4149.
- [9] J.N. Ginocchio, *Phys. Rev. C* 66 (2002) 064312.
- [10] A. Bohr, Ben R. Mottelson, *Nuclear Structure*, vol. II, W. A. Benjamin, Reading, MA, 1975.
- [11] J.N. Ginocchio, *Phys. Rev. C* 69 (2004) 034318.
- [12] G. Eyre, H. Osborn, *Nucl. Phys. B* 116 (1976) 281.
- [13] J.N. Ginocchio, A. Leviatan, *Phys. Lett. B* 425 (1998).
- [14] M.E. Rose, R.R. Newton, *Phys. Rev.* 82 (1951) 470.
- [15] M.E. Rose, *Relativistic Electron Theory*, Wiley, New York, 1961.

- [16] A. Leviatan, J.N. Ginocchio, *Phys. Lett. B* 518 (2001) 214.
- [17] S. Marcos, L.N. Savushkin, M. Lopez-Quelle, P. Ring, *Phys. Rev. C* 62 (2000) 034318.
- [18] S. Marcos, et al., *Phys. Lett. B* 513 (2001) 30.
- [19] P. Alberto, M. Fiolhais, M. Malheiro, A. Delfino, M. Chiapparini, *Phys. Rev. C* 65 (2002) 034307.
- [20] M.G. Mayer, J.H.D. Jensen, *Elementary Theory of Nuclear Shell Structure*, Wiley, New York, 1955.
- [21] *Table of Isotopes*, edited by R.B. Firestone, et al., Wiley, New York, 1996.
- [22] C. Gustafson, I.L. Lamm, B. Nilsson, S.G. Nilsson, *Arkiv Fysik* 36 (1967) 613.
- [23] A. Bohr, I. Hamamoto, B.R. Mottelson, *Phys. Scr.* 26 (1982) 267.
- [24] J. Dudek, W. Nazarewicz, Z. Szymanski, G.A. Leander, *Phys. Rev. Lett.* 59 (1987) 1405.
- [25] G.A. Lalazissis, Y.K. Gambhir, J.P. Maharana, C.S. Warke, P. Ring, *Phys. Rev. C* 58 (1998) R45.
- [26] A.M. Bruce, et al., *Phys. Rev. C* 56 (1997) 1438.
- [27] B. Mottelson, *Nucl. Phys. A* 522 (1991) 1c.
- [28] F.S. Stephens, *Nucl. Phys. A* 520 (1990) c91.
- [29] W. Nazarewicz, P.J. Twin, P. Fallon, J.D. Garrett, *Phys. Rev. Lett.* 64 (1990) 1654.
- [30] J. Dudek, T.R. Werner, Z. Szymanski, *Phys. Lett.* 248 (1990) 235.
- [31] F.S. Stephens, et al., *Phys. Rev. Lett.* 65 (1990) 301.
- [32] K. Zuber, et al., *Phys. Lett. B* 254 (1991) 308.
- [33] J.Y. Zeng, C.S. Wu, J. Meng, Y.A. Lei, C.Z. Lin, *Commun. Theoret. Phys.* 18 (1992) 179.
- [34] A.J. Kreiner, *Phys. Lett. B* 279 (1992) 233.
- [35] A.J. Kreiner, *Nucl. Phys. A* 553 (1993) c535.
- [36] C. Baktash, W. Nazarewicz, R. Wyss, *Nucl. Phys. A* 555 (1993) 375.
- [37] P.G. Bizzeti, *Nucl. Instrum. Methods Phys. Res. A* 328 (1993) 361.
- [38] D.T. Vo, et al., *Phys. Rev. Lett.* 71 (1993) 340.
- [39] S. Lunardi, et al., *Phys. Rev. Lett.* 72 (1993) 1427.
- [40] A.J. Kreiner, et al., *Nucl. Phys. A* 583 (1995) c209.
- [41] Z. Szymanski, *Phys. Rev. C* 51 (1995) R1094.
- [42] D. Nisius, et al., *Phys. Lett. B* 346 (1995) 15.
- [43] J.A. Cizewski, et al., *Phys. Rev. C* 52 (1995) 1307.
- [44] Z. Szymanski, *Acta Phys. Polon. B* 26 (1995) 175.
- [45] F.S. Stephens, et al., *Phys. Rev. C* 57 (1998) R1565.
- [46] A.L. Blokhin, T. Beuschel, J.P. Draayer, C. Bahri, *Nucl. Phys. A* 612 (1997) 163.
- [47] T. Beuschel, A.L. Blokhin, J.P. Draayer, *Nucl. Phys. A* 619 (1997) 119.
- [48] I.M. Green, S.A. Moszkowski, *Phys. Rev.* 139B (1965) 790.
- [49] R. Arvieu, S.A. Moszkowski, *Phys. Rev.* 145 (1966) 830.
- [50] A. Plastino, R. Arvieu, S.A. Moszkowski, *Phys. Rev.* 145 (1966) 837.
- [51] R. Arvieu, in: M. Jean, R.A. Ricci (Eds.), *Proceedings of the International School of Physics Enrico Fermi, Course XL*, Academic Press, New York, 1969.
- [52] W.P. Jones, L.W. Borgman, K.T. Hecht, John Bardwick, W.C. Parkinson, *Phys. Rev. C* 4 (1971) 580.
- [53] F. Todd Baker, Robert Tickle, *Phys. Rev. C* 5 (1972) 182.
- [54] D. Strottman, *Nucl. Phys. A* 118 (1972) 488.
- [55] P. Van Isacker, O. Juillet, *J. Phys. G* 25 (1999) 675.
- [56] P. Van Isacker, O. Juillet, F. Nowacki, *Phys. Rev. Lett.* 82 (1999) 2060.
- [57] R.D. Ratna Raju, J.P. Draayer, K.T. Hecht, *Nucl. Phys. A* 202 (1973) 433.
- [58] D. Strottman, *Phys. Lett. B* 47 (1998) 215.
- [59] C. Vargas, J.G. Hirsch, T. Beuschel, J.P. Draayer, *Phys. Rev. C* 61 (2000) 031301 (R).
- [60] G. Popa, J.G. Hirsch, J.P. Draayer, *Phys. Rev. C* 62 (2000) 064313.
- [61] J.P. Draayer, G. Popa, J.G. Hirsch, C. Vargas, *Revista Mexicana de Fisica* 46 (2000) 71.
- [62] V.G. Gueorguiev, J.P. Draayer, C.W. Johnson, *Phys. Rev. C* 63 (2001) 014318.
- [63] C.E. Vargas, J.G. Hirsch, J.P. Draayer, *Phys. Rev. C* 64 (2001) 034306.
- [64] D. Troltenier, W. Nazarewicz, Z. Szymanski, J.P. Draayer, *Nucl. Phys. A* 567 (1994) 591.
- [65] O. Castanos, M. Moshinsky, C. Quesne, *Phys. Lett. B* 277 (1992) 238.
- [66] C. Bahri, J.P. Draayer, S.A. Moszkowski, *Phys. Rev. Lett.* 68 (1992) 2133.

- [67] B.D. Serot, J. D. Walecka, in: J.W. Negele, E. Vogt (Eds.), *The Relativistic Nuclear Many-Body Problem in Advances in Nuclear Physics*, vol. 16, Plenum, New York, 1986.
- [68] B.D. Serot, *Rep. Prog. Phys.* 55 (1992) 1855.
- [69] B.D. Serot, J.D. Walecka, *Acta Phys. Pol. B* 23 (1992) 655.
- [70] B.D. Serot, J.D. Walecka, in: T.L. Ainsworth, C.E. Campbell, B.E. Clements, E. Krotscheck (Eds.), *Recent Progress in Many-Body Theories*, vol. 3, Plenum, New York, 1992, p. 49.
- [71] B.D. Serot, J.D. Walecka, *Int. J. Mod. Phys. E* 6 (1997) 515.
- [72] P. Manakos, T. Mannel, *Z. Phys. A* 330 (1988) 223.
- [73] P. Manakos, T. Mannel, *Z. Phys. A* 334 (1989) 481.
- [74] P.-G. Reinhard, *Rep. Prog. Phys.* 52 (1989) 439.
- [75] B.A. Nikolaus, T. Hoch, D.G. Madland, *Phys. Rev. C* 46 (1992) 1757.
- [76] T. Bürvenich, private communication.
- [77] T.D. Cohen, R.J. Furnstahl, D.K. Griegel, X. Jin, *Prog. Part. Nucl. Phys.* 35 (1995) 221.
- [78] J. Gasser, H. Leutwyler, M.E. Saino, *Phys. Lett. B* 253 (1991) 252.
- [79] M.E. Saino, *Proceedings of the Ninth International Symposium on Meson–Nucleon Physics and the Structure of the Nucleon*, District of Columbia, 26–31 July 2001, hep-ph/0110413.
- [80] M. Gell–Mann, R.J. Oakes, B. Renner, *Phys. Rev.* 175 (1968) 2195.
- [81] J.N. Ginocchio, D.G. Madland, *Phys. Rev. C* 57 (1998) 1167.
- [82] J. Meng, K. Sugawara-Tanabe, S. Yamaji, P. Ring, A. Arima, *Phys. Rev.* 58 (1998) R628.
- [83] K. Sugawara-Tanabe, S. Yamaji, A. Arima, *Phys. Rev. C* 62 (2000) 054307.
- [84] J.N. Ginocchio, A. Leviatan, *Phys. Rev. Lett.* 87 (2001) 072502.
- [85] K. Sugawara-Tanabe, S. Yamaji, A. Arima, *Phys. Rev. C* 65 (2002) 054313.
- [86] P.J. Borycki, J. Ginocchio, W. Nazarewicz, M. Stoitsov, *Phys. Rev. C* 68 (2003) 014304.
- [87] J.N. Ginocchio, A. Leviatan, J. Meng, Shan-Gui Zhou, *Phys. Rev. C* 69 (2004) 034303.
- [88] S.G. Zhou, J. Meng, S. Yamaji, S.C. Yang, *Chin. Phys. Lett.* 17 (2000) 717.
- [89] S.G. Zhou, J. Meng, P. Ring, *Phys. Rev. C* 68 (2003) 034323.
- [90] J. Meng, P. Ring, *Phys. Rev. Lett.* 77 (1996) 3963.
- [91] J. Meng, *Nucl. Phys. A* 635 (1998) 3.
- [92] J. Meng, P. Ring, *Phys. Rev. Lett.* 80 (1998) 460.
- [93] Dr. Seuss, *Horton Hears a Who!* Random House, New York, 1954 (illustrated by T.S. Geisel).
- [94] E. Hagberg, et al., *Nucl. Phys. A* 571 (1994) 555.
- [95] B. Reitz, et al., *Phys. Rev. Lett.* 82 (1999) 291.
- [96] P. von Neumann-Cosel, *Progress in Part. Nucl. Phys.* 44 (2000) 49.
- [97] H. Margenau, *Phys. Rev.* 58 (1940) 383.
- [98] L.D. Miller, *Ann. Phys.* 91 (1975) 40.
- [99] J.N. Ginocchio, *Phys. Rev. C* 59 (1999) 2487.
- [100] I. Talmi, *Simple Models of Complex Nuclei*, Switzerland, Harwood, 1993.
- [101] J.A. McNeil, R.D. Amado, C.J. Horowitz, M. Oka, J.R. Shepard, D.A. Sparrow, *Phys. Rev. C* 34 (1986) 746.
- [102] T.K. Alexander, et al., *Nucl. Phys. A* 526 (1991) 407.
- [103] E. Hagberg, et al., *Nucl. Phys. A* 571 (1994) 555.
- [104] B.A. Brown, B.H. Wildenthal, *Atom. Data Nucl. Data Tables* 33 (1985) 347.
- [105] W. Knüpfer, W. Müller, B.C. Metsch, A. Richter, *Nucl. Phys. A* 457 (1986) 292.
- [106] B. Castel, I.S. Towner, *Modern Theories of Nuclear Moments*, Clarendon, Oxford, 1990.
- [107] B.A. Brown, *IOP Conf. Ser.* 86 (1987) 119.
- [108] P. von Neumann-Cosel, J.N. Ginocchio, *Phys. Rev. C* 62 (2000) 014308.
- [109] *Evaluated Nuclear Structure Data File*, National Nuclear Data Center, 2000.
- [110] E. Hagberg, et al., *Phys. Rev. C* 56 (1997) 135.
- [111] K.E. Rehm, et al., J. Görres, *Phys. Rev. Lett.* 80 (1998) 676.
- [112] P. von Neumann-Cosel, A. Richter, C. Schlegel, R. Schulz, *Nucl. Phys. A* 650 (1999) 267.
- [113] T. Otsuka, M. Honma, T. Misuzaki, *Phys. Rev. Lett.* 80 (1998) 676.
- [114] I.S. Towner, *Phys. Rep.* 155 (1987) 763.
- [115] A. Arima, K. Shimizu, W. Bentz, H. Hyuga, *Adv. Nucl. Phys.* 18 (1987) 1.

- [116] I.S. Towner, F.C. Khanna, Nucl. Phys. A 474 (1987) 290.
- [117] D.D. Warner, P. Van Isacker, Phys. Lett. B 247 (1990) 1.
- [118] J. Meng, K. Sugawara-Tanabe, S. Yamaji, A. Arima, Phys. Rev. C 59 (1999) 154.
- [119] P. Alberto, M. Fiolhais, M. Malheiro, A. Delfino, M. Chiapparini, Phys. Rev. Lett. 86 (2001) 5015.
- [120] R. Lisboa, M. Malheiro, P. Alberto, Phys. Rev. C 67 (2003) 054305.
- [121] R. Lisboa, M. Malheiro, P. Alberto, Brazilian J. Phys. 34 (2004) 293.
- [122] R. Kozack, D.G. Madland, Phys. Rev. C 39 (1989) 1461.
- [123] E.D. Cooper, S. Hama, B.C. Clark, R.L. Mercer, Phys. Rev. C 47 (1993) 297.
- [124] J.B. Bowlin, A.S. Goldhaber, C. Wilkin, Z. Phys. A 331 (1988) 83.
- [125] H. Feshbach, Theoretical Nuclear Physics—Nuclear Reactions, Wiley, New York, 1992.
- [126] J.N. Ginocchio, Phys. Rev. Lett. 82 (1999) 4599.
- [127] H. Lee, S. Wilmsen, Phys. Rev. C 62 (2000) 024602.
- [128] R.W. Ferguson, et al., Phys. Rev. C 33 (1986) 239.
- [129] H. Lee, S.A. Sofianos, Phys. Rev. C 69 (2004) 054608.
- [130] J.N. Ginocchio, Phys. Rep. 315 (1999) 231.
- [131] Shan-Gui Zhou, Jie Meng, P. Ring, Phys. Rev. Lett. 91 (2003) 262501.
- [132] T. Bürvenich, et al., Phys. Lett. B 542 (2002) 261.
- [133] D. Garetta, et al., Phys. Lett. B 151 (1985) 473.
- [134] N. Isgur, Phys. Rev. D 62 (2000) 054026;
N. Isgur, Phys. Rev. D 62 (2000) 014025.
- [135] N. Isgur, M.B. Wise, Phys. Lett. B 232 (1989) 113;
N. Isgur, M.B. Wise, Phys. Rev. Lett. 66 (1991) 1130.
- [136] K. Abe, et al., Phys. Rev. D 69 (2004) 112002.
- [137] M. Acciari, et al., Phys. Lett. B 465 (1999) 323–334.
- [138] R. Gupta, Nucl. Phys. 83 (2000) 295;
A. Ali Khan, et al., Phys. Rev. D 62 (2000) 054505.
- [139] A. Ali-Khan, et al., Nucl. Phys. Proc. B 73 (Suppl.) (1999) 345.
- [140] R. Lewis, R.M. Woloshyn, hep-lat/9909106; and references therein.
- [141] R. Lewis, R.M. Woloshyn, hep-lat/0003011.
- [142] Table XXI, J. Hein, et al., hep-ph/0003130.
- [143] S. Godfrey, R. Kokoski, Phys. Rev. D 43 (1991) 1679.
- [144] J. Koponen, A.M. Green, C. Michael, hep-lat/0310002, 2003.
- [145] D. Bisello, et al. (DM2 Collab.), LAL-90-35 (1990).
- [146] W. Buchmüller, S.H.H. Tye, Phys. Rev. D 24 (1981) 132;
A.K. Grant, J.L. Rosner, E. Rynes, Phys. Rev. D 47 (1993) 1981.
- [147] A.S. Goldhaber, T. Goldman, Phys. Lett. B 344 (1995) 319.
- [148] G.S. Bali, K. Schilling, A. Wachter, Phys. Rev. D 56 (1997) 2566.
- [150] F. Ravndal, Phys. Lett. B 113 (1982) 57.
- [151] R. Tegen, Ann. Phys. 197 (1990) 439.
- [152] M. Centelles, X. Vinx, M. Barranco, P. Schuck, Nucl. Phys. A 519 (1990) 73c.
- [153] V.I. Kukulin, G. Loyola, M. Moshinsky, Phys. Lett. A 158 (1991) 19.
- [154] Q.-W. Chao, Chin. Phys. 11 (2002) 757.
- [155] R.K. Bhaduri, Models of the Nucleon: From Quarks to Soliton, Addison-Wesley, Reading, MA, 1988.
- [157] T.-S. Chen, H.-F. Lu, J. Meng, S.-Q. Zhang, S.-G. Zhou, Chin. Phys. Lett. 20 (2003) 358;
T.-S. Chen, H.-F. Lu, J. Meng, S.-Q. Zhang, S.-G. Zhou, Phys. Lett. A 158 (1991) 19.
- [158] R. Lisboa, M. Malheiro, A.S. de Castro, P. Alberto, M. Fiolhais, Phys. Rev. C 69 (2004) 02431.
- [159] N.V.J. Swamy, Phys. Rev. 180 (1969) 1225.
- [160] Y.M. Cho, Il Nuovo Cimento A 23 (1974) 550.
- [161] J.N. Ginocchio, in: B. Gruber, R. Lenczewski (Eds.), Symmetries in Science, vol. II, Plenum Press, New York, 1986.
- [162] M. Moshinsky, A. Szczepaniak, J. Phys. A: Math. Gen. 22 (1989) 817.
- [163] B.G. Wybourne, Classical Groups for Physicists, Wiley, New York, 1974.
- [164] A. Leviatan, Phys. Rev. Lett. 92 (2004) 202501.

- [165] J.N. Ginocchio, Phys. Rev. C 65 (2002) 054002.
- [166] H.P. Stapp, T.J. Ypsilantis, N. Metropolis, Phys. Rev. 105 (1957) 302.
- [167] V.G.J. Stoks, R.A.M. Klomp, M.C.M. Rentmeester, J.J. de Swart, Phys. Rev. C 48 (1993) 792.
- [168] N-N OnLine, <http://nn-online.sci.kun.nl>, Theoretical High Energy Physics Group, University of Nijmegen, Netherlands.
- [169] Lewis Carroll, Alice's Adventures in Wonderland (illustrated by Anthony Browne), Alfred A. Knopf, New York, 1988.
- [170] A.R. Edmonds, Angular Momentum in Quantum Mechanics, Princeton University Press, Princeton, 1960.